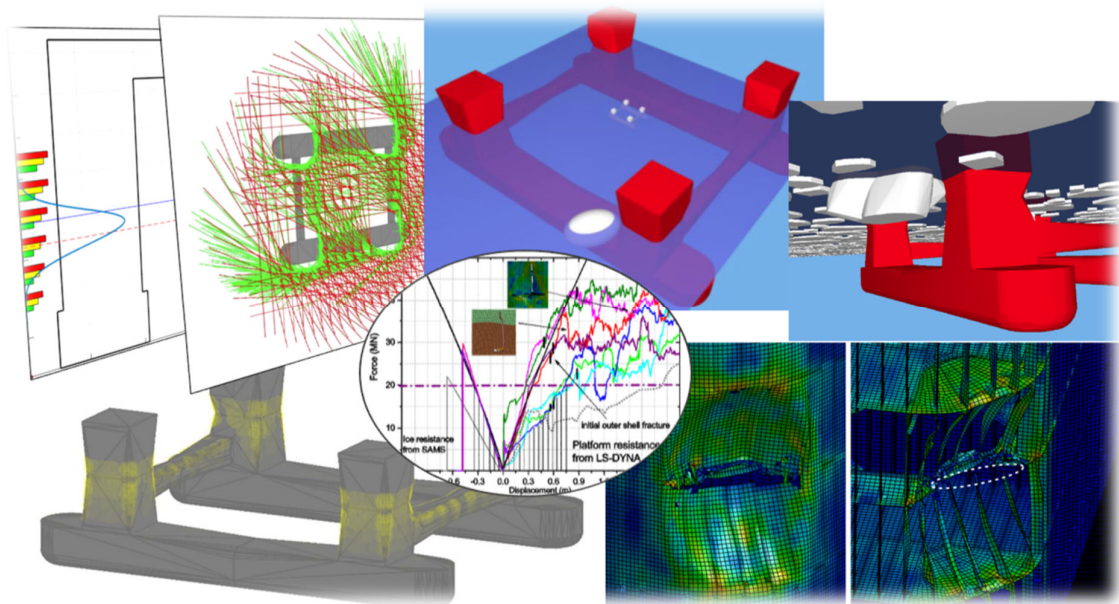


**PTIL - KONSTRUKSJONSSIKKERHET I NORDOMRÅDENE
(NORD ST19)**

**Assessment of Structural Damage due to
Glacial Ice Impact**

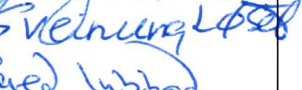
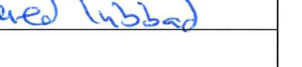
Petroleumstilsynet



Report NO: ArcISo_2018_Ptil01

By ArcISo AS

Date: 2018-11-30

 <p>ArcISO Arctic Integrated Solutions</p> <p>Address: NO-7034 Trondheim, Norway Location: Gløshaugen Høgskoleringen 7A Managing director: Raed Lubbad (+47 735 94 583) Email: raed.lubbad@ntnu.no Enterprise NO: 917100454 Website: https://arciso.com</p>	<h1>ArcISO AS</h1> <p>AUTHOR(S) Wenjun Lu, Zhaolong Yu, Marnix Van Den Berg, Raed Lubbad, Jørgen Amdahl, Sveinung Løset, Ekaterina Kim</p>		
<p>TITLE PTIL - Konstruksjonssikkerhet i Nordområdene (NORD ST19)</p>	<p>CLIENT(S) Petroleumstilsynet (Petroleum Safety Authority Norway)</p>		
<p>CLASS. THIS PAGE Open</p>	<p>PROJECT LEADER Raed Lubbad</p>	<p>PROJECT NO ST19</p>	<p>NO OF PAGES 96</p>
<p>APPROVED BY Raed Lubbad (ArcISO Managing Director)</p>	<p>CHECKED BY Jørgen Amdahl  Sveinung Løset  Raed Lubbad </p>		
<p>REPORT NO ArcISO_2018_Ptil01</p>	<p>DATE 30.11.2018</p>		
<p>ABSTRACT</p> <p>In order to gain insights into the consequence of potential impacts between offshore structures and relatively small glacial ice features, the Petroleum Safety Authority Norway (Petroleumstilsynet) initiated several studies of which this study (ST19) is one of them. The ST19 focuses on the interaction between floating spheroidal glacial ice features (<15 m) and a semi-submersible structure in irregular seas and in the presence of sea currents. The ST19 study comprises three stages, namely:</p> <ul style="list-style-type: none"> • Stage #1: Analysis of impact events to establish probability distributions for impact velocities and locations on the structure. • Stage #2: Simulations of hundreds of impact scenarios using the ‘Simulator for Arctic Marine Structures’ (SAMS) to create <i>energy map</i> showing the <i>demand for energy dissipation</i> at each location on the structure. • Stage #3: Structural damage assessment for the critical impact scenarios. <p>Innovative methods and a cutting-edge simulator for ice-structure interactions (SAMS) are utilised in the different stages of the project offering a great insight into the problem and leading to many important conclusions. The results for the structure under consideration in ST19 show that the maximum demand for energy dissipation is 7.32 MJ but with a very low probability. Actually, 90% of the simulated impacts result in an impact energy lower than 4.3 MJ. The shared-energy approach for damage assessment shows that the maximum indentation depth into the structure in ST19 can vary from 0.25 m to 0.55 m depending on the impact locations. As the outer shell rupture generally is predicted to occur at 0.6 m-0.9 m, the structure is considered safe from compartment flooding risks with the given impact energy.</p> <p>Although the results from this study are specific to the given structure and pre-assumed ice features, the approach is quite generic and could be adopted to other structures and ice geometries. It should also be noted that critical structural members such as risers and mooring lines are not considered in this study and they should be included in further studies.</p>			
<p>KEY WORDS: SAMS, Nonlinear FEM, Energy map, Damage assessment, Impact, Ice, Semi-submersible</p>			

Contents

1	Introduction.....	3
2	Background for ST19.....	6
2.1	Study Site	6
2.1.1	Waves	7
2.1.2	Currents	9
2.1.3	Ice Conditions.....	9
2.2	Review of ST5.....	12
2.2.1	ST5 tasks	12
2.2.2	ST5 major findings	13
2.2.3	Comments on ST5	14
2.3	General considerations of ST19	16
2.3.1	Ice feature's geometry	16
2.3.2	Relative motions.....	18
2.3.3	Design limit state and ice crushing considerations.....	19
3	Analysis of Impact Events.....	21
3.1	Uncorrelated impact velocity and height from ST5	21
3.2	Relative motion in a single wave component.....	22
3.3	Relative motion in a sea state with random waves.....	24
3.4	Sampling of impact events	26
3.4.1	Impact in the sway direction.....	27
3.4.2	Impact in the vertical direction.....	34
3.5	Summary	36
4	Simulations of Impacts Using SAMS	38
4.1	Description of SAMS	38
4.2	Verification of SAMS simulations	39
4.3	Energy map.....	42
4.3.1	Simulation input values	42
4.3.2	Scaling of the simulation results.....	43
4.3.3	Simulation output	44
4.3.4	Test matrix: spheroidal ice feature in open water.....	46
4.3.5	Simulation results	47
4.3.6	Critical impact scenarios	52
4.3.7	Simulations with ambient floe ice and other ice feature shapes.....	53

4.3.8	Summary	55
5	Assessment of Structural Damage.....	57
5.1	Shared-Energy approach in ST19.....	57
5.2	Force-deformation curves for the ice feature using SAMS	59
5.2.1	Data source and method for establishing CSE.....	59
5.2.2	Reconstruction of force-deformation curve from the SAMS results.....	60
5.2.3	Simplified method	62
5.3	Force-deformation curves for the structure using Non-linear FEM analysis in LS-DYNA..	63
5.3.1	Finite Element Modelling.....	64
5.3.2	Non-linear FEM analysis.....	69
5.3.3	Simplified analytical formulation of structure frames to ice loading	73
5.3.4	Assessment of strength of structural components with simplified methods.....	78
5.4	Integrated Analysis of SAMS and LS-DYNA	81
5.4.1	Discussion of fracture modelling in ST5 and ST19	83
6	Discussions.....	86
6.1	Discussion on ice feature's geometry	86
6.2	Discussion on correlated impact velocities and heights	86
6.3	Discussion on the energy map	88
6.4	Discussion on the damage assessment	89
7	Conclusions and Recommendations for Further Work	91
7.1	Conclusions	92
7.2	Further work	93
	Reference.....	95

1 Introduction

Floating glacial ice features of various sizes may pose great threat to the structural integrity of man-made structures in the High North. The interactions between glacial ice features, waves, broken sea ice and structures are quite complex. Figure 1.1 exemplifies a small iceberg with violent heave motion in waves with the presence of ambient broken ice in the Marginal Ice Zone (MIZ) at Spitsbergenbanken in the Barents Sea. A thorough hydrodynamic analysis of multi-bodies' interactions would yield reliable motion predictions for different sea states.

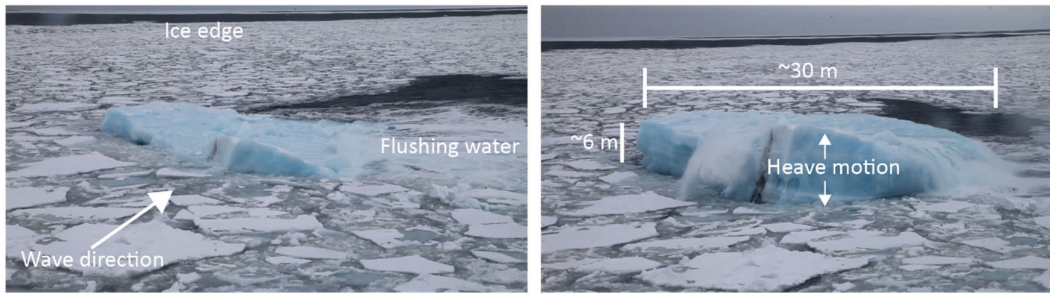


Figure 1.1. Small iceberg motion in waves and broken ice in the MIZ about N77.18° and E25.3° (March 2016), Barents sea.

In addition, the mechanics of a glacial ice feature colliding with a structure involve challenging coupled processes and complex material behaviours.

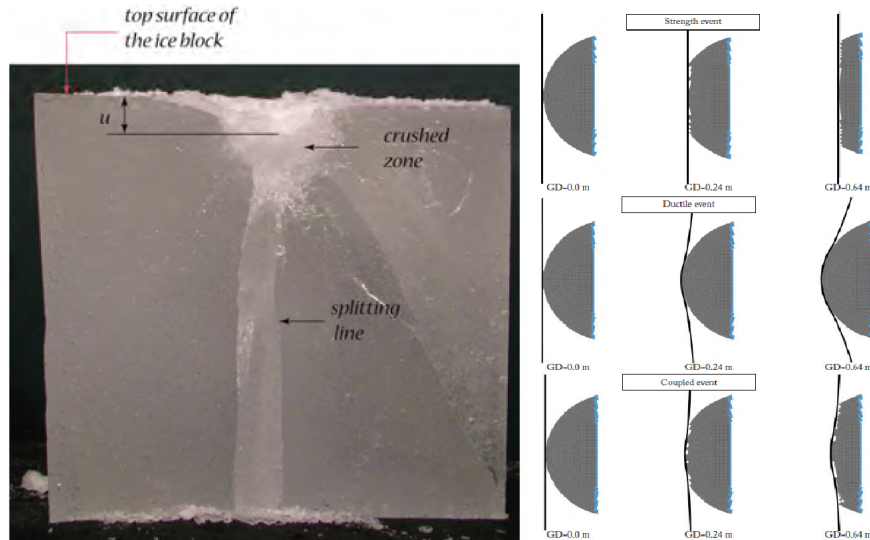


Figure 1.2 a) An ice block fractures at different scales; b) Simulation of different impact events between ice mass and a flat plate (Kim, 2014).

Ice is a complicated natural material, and it fractures at multiple scales. One can observe ice crushing (a type of fracture at grain size scale) at the local contact zone; and fractures at larger scale, such as splitting and flaking as in the model test shown in Figure 1.2a. Trying to simulate such multi-scale fractures into fine details is a challenging research topic within the solid mechanics community (Lu et al., 2018). On top of this challenging material behaviour, the coupled interaction between a glacial ice feature and structural members (e.g., a stiffened plate) can be treated differently in different events. From an

application point of view, the impact energy, its associated energy dissipation, structural deformation and the consequent damage assessment are of great interest.

This study (ST19) builds on the results from a previous project on structural safety in the High North (ST5) (Ekeberg et al., 2018). The ST5 project comprised two main studies:

- The 1st study described and identified concurrent knowledge and challenges in relation to structural safety in the High North. With reference to a site location (i.e., the northernmost block in the 23rd licensing area at N74°).
- The 2nd study narrowed down the investigation to a specific scenario regarding the impact between glacial ice features (with a characteristic water line < 15 m) and a semi-submersible structure.

The ST19 project substantially extends and enriches the work of ST5. ST19 focuses on the interaction between floating spheroidal glacial ice features (<15 m) and a semi-submersible structure in irregular seas and in the presence of sea currents. The ST19 study comprises three stages, namely:

- ***Stage #1: Analysis of Impact Events***

The motion of the glacial ice features is studied relative to a semi-submersible structure for the design sea state and in the presence of sea currents, which enabled identification of the impact velocities and hit locations on the structure. The outcome of Stage #1 is Probability Density Functions (PDFs) for impact velocities and locations on the structure.

- ***Stage #2: Simulations of Impacts Using SAMS***

The results of Stage #1 are used by the *Simulator for Arctic Marine Structures* (SAMS), a product of Arctic Integrated Solutions (ArcISo AS), to simulate hundreds of impact scenarios. The results from SAMS are verified using analytical solutions. For each impact scenario, the *demand for energy dissipation* is calculated i.e., the fraction of the total impact energy (kinetic energy) that is dissipated at the contact by crushing the glacial ice and deforming the semi-submersible structure. The rest of the impact energy is usually transferred to global rigid-body motions. The outcome of this stage is an *energy map* showing the *demand for energy dissipation* at each location on the structure. Consequently, we could identify number of critical impact scenarios that might potentially lead to structural damage.

- ***Stage #3: Assessment of Structural Damage***

Current design standards and recommended practice do not provide clear procedures to estimate structural damage due to impact with glacial ice features for the Accidental Limit State (ALS) analysis. In Stage #3 of ST19, we adopted the so-called shared-energy approach in analogy to the procedures for ship-installation impacts (DNV-GL-RP-C208, 2016). For the critical scenarios identified in Stage #2, integrated analyses in LS-DYNA and SAMS are carried out. The former implies a non-linear Finite Element Method (NLFEM) type of analyses that assumes rigid ice and deformable structure, and it is used to derive force-deformation curves for the structure. The latter (SAMS) assumes a rigid structure and it is used to derive force-deformation curves for the glacial ice features. The combined results are used to define the amount of energy absorbed by the structure and the consequent structural damage. Further, the different fracture criteria are compared and their effects on the results are discussed. Finally, ST19 provides simplified analytical formulation of structure frames to ice loading and proposes simplified methods for the assessment of strength of structural components.

The report comprises seven chapters as follows:

The second chapter describes the physical environment at the study site and reviews the findings from the previous study, ST5. The third chapter describes the method used to analyse impact events (Stage #1), and it presents and discusses the results. Chapter 4 describes the simulations of impacts using SAMS (Stage #2) including a detailed discussion of the results. Chapter 5 explains the shared-energy approach adopted in this study for structural damage assessment, and it presents the results from the integrated LS-DYNA-SAMS analysis (Stage #3). In addition, the chapter compares different fracture criteria for the NLFEM analysis. Moreover, Chapter 5 proposes simplified methods for the assessment of strength of structural components. Chapter 6 summarises the main results obtained from the three stages of ST19, and it discusses them thoroughly. Finally, the seventh chapter draws the most important conclusions from this study and suggests ideas for further work.

2 Background for ST19

This chapter describes the study site and presents the findings from the previous studies.

2.1 Study Site

The site chosen for the ST19 study is the same as that in ST5 (Ekeberg et al., 2018); namely, the northernmost Block A in the 23rd licencing round (see Figure 2.1). The site is located at about N74°, E35.67°; and the physical environmental conditions such as waves, wind, current and ice were derived based on the currently best available measurements (see Figure 2.2) in the Barents sea (Eik and Dezecot, 2016). This paragraph is largely based on the work by Eik and Dezecot (2016) with focus on the selected study site. For completeness, they are re-presented in this report together with comments and discussions on the choices of environmental parameters made in ST5 and this project (ST19).

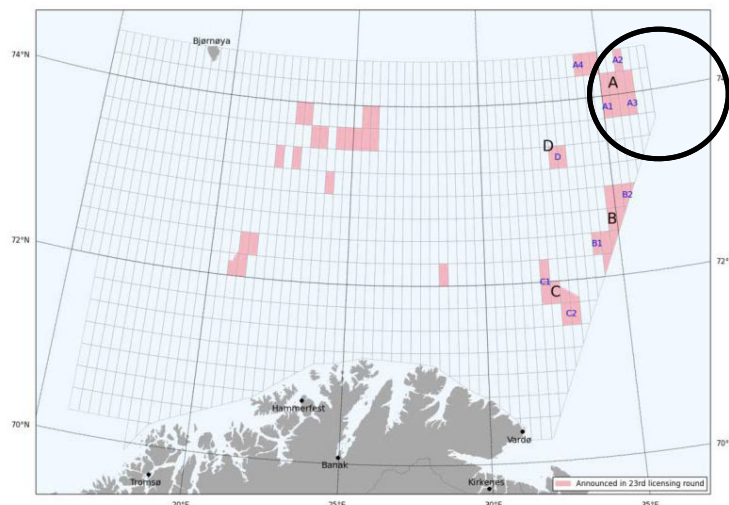


Figure 2.1: Selected study site (from (Eik and Dezecot, 2016)).



Figure 2.2: Ocean (blue markers) and ice (red markers) measurement locations in the Barents sea (from (Eik and Dezecot, 2016)).

The estimated environmental extreme values in Block A are summarised in Table 2.1. The extreme values are defined based on the annual probability of exceedance (i.e., q probability) according to Eq. (2.1). $q = 0.63, 10^{-1}, 10^{-2}$, and 10^{-4} correspond to return periods of $R = 1, 10, 100$, and 10000 years.

$$q = 1 - \exp\left(-\frac{T}{R}\right) \quad T = 1 \text{ [year]} \quad (2.1)$$

Table 2.1: Summary of estimate extreme wind, wave and current at Block A, after (Eik and Dezecot, 2016).

Parameter	Unit	Annual probability of exceedance			
		0.63	10^{-1}	10^{-2}	10^{-4}
Wind speed, 1hour, 10 m	[m/s]	25.5	28.0	30.5	35.0
Wind speed, 10 min, 10 m	[m/s]	28.0	31.0	33.5	38.5
Significant wave height	[m]	9.8	11.8	13.8	17.5
Spectral peak period	[s]	15.0	16.5	18.0	20.9
Individual wave height	[m]	18.9	22.2	25.7	32.8
Crest height	[m]	11.3	13.4	15.5	20.0
Current speed, Surface	[cm/s]	66	73	79	90
Current speed, 70 m	[cm/s]	46	50	54	61
Current speed, 3 m a.s.b. ¹	[cm/s]	32	34	37	41

Generally, according to Eik and Dezecot (2016), the wind, wave, and current conditions are similar to or milder than those in the North sea. In the forthcoming analysis, as we are mainly concerned with the wave and current conditions, a brief summary is presented in this regard.

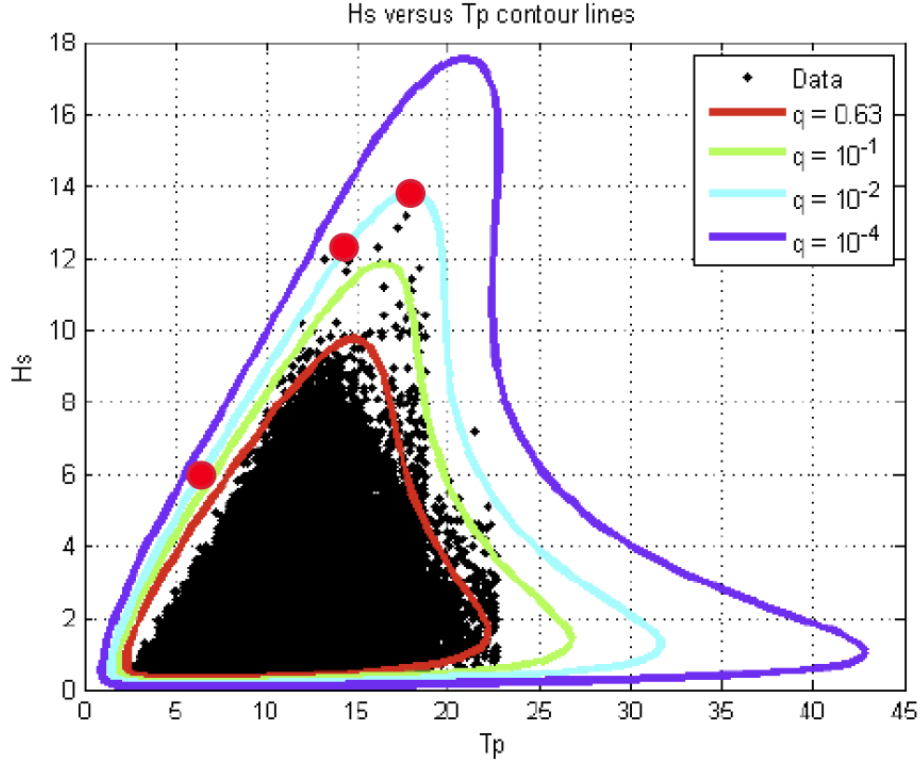
2.1.1 Waves

For waves, both the short-term and long-term statistical information are available. Specifically, the significant wave height's (H_s) directional distribution, monthly distribution, and its joint probability distribution together with wave period (T_p) are available after Eik and Dezecot (2016). As a follow-up study of ST5 (Ekeberg et al., 2018), similarly, ST19 performs analysis based on the long-term omnidirectional wave information, which is summarised in Table 2.2, in which, three selected sea states in ST5 are also highlighted (within red frames).

Table 2.2: $H_s - T_p$ values for different return period at Block A, after (Eik and Dezecot, 2016).

Annual probability of exceedance											
0.63			10^{-1}			10^{-2}			10^{-4}		
H_s [m]	T_{PL} [s]	T_{pH} [s]	H_s [m]	T_{PL} [s]	T_{pH} [s]	H_s [m]	T_{PL} [s]	T_{pH} [s]	H_s [m]	T_{PL} [s]	T_{pH} [s]
9.8	14.8	14.8	11.8	16.4	16.4	13.8	18.0	18.0	17.5	20.8	20.8
9.0	12.6	16.2	11.0	14.1	17.8	13.0	15.6	19.3	17.0	18.8	22.2
8.0	10.9	16.7	10.0	12.5	18.1	12.0	14.0	19.6	16.0	17.0	22.7
7.0	9.4	17.1	9.0	11.1	18.4	11.0	12.7	19.7	15.0	15.7	22.7
6.0	8.0	17.6	8.0	9.7	18.7	10.0	11.4	19.8	14.0	14.5	22.7
5.0	6.6	18.3	7.0	8.4	19.1	9.0	10.2	20.0	13.0	13.3	22.5
4.0	5.3	19.3	6.0	7.1	19.7	8.0	9.0	20.3	12.0	12.3	22.4
3.0	4.2	20.5	5.0	5.9	20.7	7.0	7.7	20.8	11.0	11.2	22.3
2.0	3.1	21.8	4.0	4.7	22.0	6.0	6.5	21.6	10.0	10.1	22.4
1.0	2.2	22.3	3.0	3.6	23.8	5.0	5.3	22.9	9.0	9.0	22.6
			2.0	2.6	25.9	4.0	4.2	24.6	8.0	7.9	23.1
			1.0	1.8	27.3	3.0	3.2	27.0	7.0	6.7	23.9
						2.0	2.3	30.0	6.0	5.6	25.2
						1.0	1.5	32.6	5.0	4.5	27.1
									4.0	3.5	29.9

The contour plot of $H_s - T_p$ joint distribution and the selected sea states in ST5 are illustrated in Figure 2.3.

Figure 2.3: $H_s - T_p$ joint contours and selected sea states (red disk-shape markers) in ST5, after (Eik and Dezecot, 2016).

2.1.2 Currents

Current was not included in the study of ST5. However, after careful considerations, it deems necessary (Fylling, 1994) to include current information in the ST19 study. This is mainly because the current velocity influences the sampling of impact events in the simulations (see Section 3.4.1).

The current data are presented at different water depths by Eik and Dezecot (2016). Considering the size and geometry of the glacial ice features within the ST19 study (i.e., a spheroidal glacial ice feature with CoG at -2.9 m from the SWL), the surface current velocity (i.e., 0 m water below water surface) is chosen as the representative value.

The directional extreme surface current velocity with different annual probability of exceedance are illustrated in Figure 2.4. Among these values, ST19 takes a similar approach as in ST5 and considers only the omnidirectional information for the current velocity as in Table 2.3.

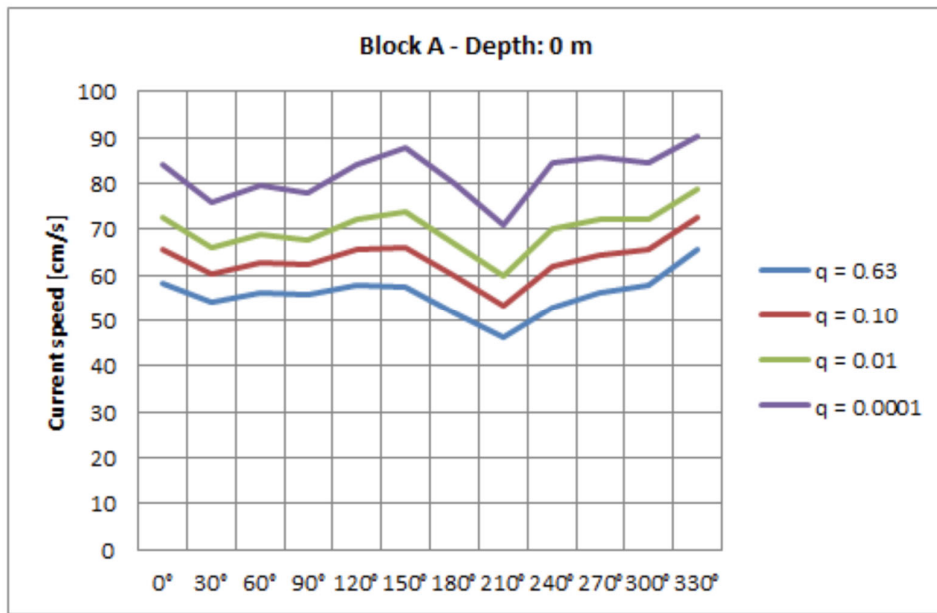


Figure 2.4: Extreme current velocities in different directions with different annual exceedance (Eik and Dezecot, 2016).

Table 2.3: Current velocity for different return periods at Block A, after (Eik and Dezecot, 2016).

Direction sector	Weibull parameters			Annual probability of exceedance			
	Shape	Scale [cm/s]	Location [cm/s]	$q = 0.63$	$q = 10^{-1}$	$q = 10^{-2}$	$q = 10^{-4}$
				-	[cm/s]	[cm/s]	[cm/s]
0°-360°	1.897	18.409	0.809	66	73	79	90

2.1.3 Ice Conditions

Based on general information in the Barents Sea, various ice types (i.e., broken ice with different concentrations, ice ridges and icebergs) can be expected in Block A (Eik and Dezecot, 2016). This

paragraph gives a general flavour about ice conditions that could potentially be encountered at the study site.

2.1.3.1 Floe ice

The general level/broken ice conditions at Block are illustrated in Figure 2.5 based on which the following observations can be made:

- Most time of the year (July to Mid-November), there is no ice present in the area.
- There is a great variability in terms of the presence of sea ice, ranging from days (e.g., 2011) to months (e.g., 2003).

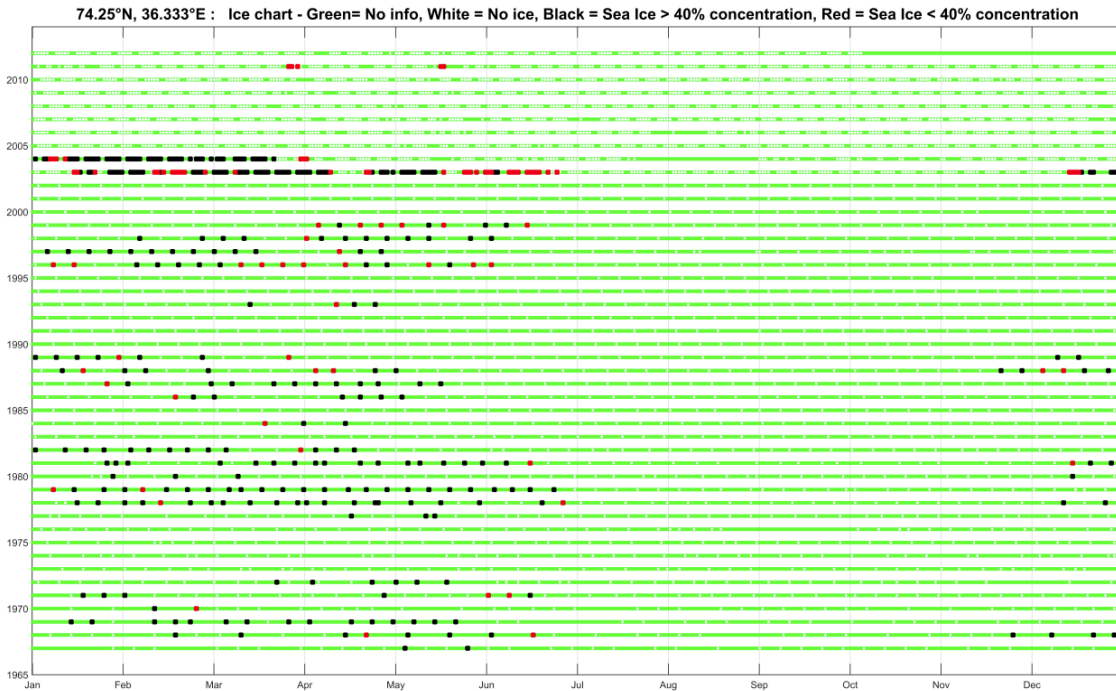


Figure 2.5: Presence of sea ice at Block A (Eik and Dezecot, 2016).

The ST19 study focuses on glacial ice features, with a characteristic length less than 15 m. Aside from extensive studies on a single glacial ice feature's impact with the structure, it is also interesting to investigate the scenario, in which, the glacial ice feature is surrounded by a broken floe ice field and its impact with the structure. Because the presence of a glacial ice feature can often be accompanied by a neighbouring broken ice field; and we are not entirely sure about the role of ambient broken floe ice in the process of glacial ice feature impacting a structure. Therefore, in selected cases, out of curiosity though not directly related to this project, we conducted such simulations (see Section 4.3.7). The broken ice field chosen is digitalized from an image taken from a helicopter at N81.595°, E15.206° in September 29th, 2015.

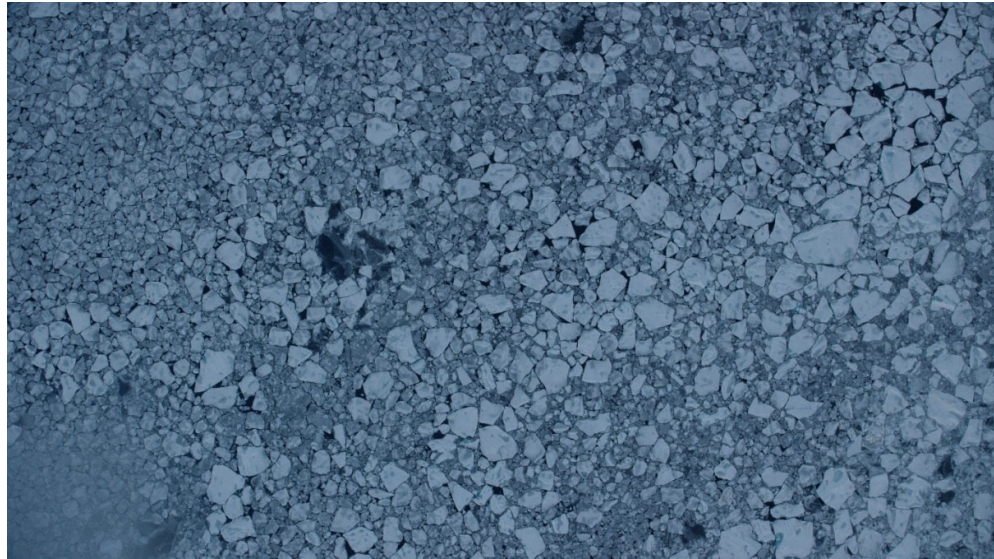


Figure 2.6: A representative broken ice field at N81.595°, E15.206° in September 29th, 2015 (Lubbad et al., 2018, Kjerstad et al., 2018).

The above real-life image is digitalized into the following ice field (see Figure 2.6) with an ice concentrations of about 58%. Considering the general ice conditions in Block A, as illustrated in Figure 2.5, this representative broken ice field is on the conservative side when it comes to consider the amount of ambient broken ice.

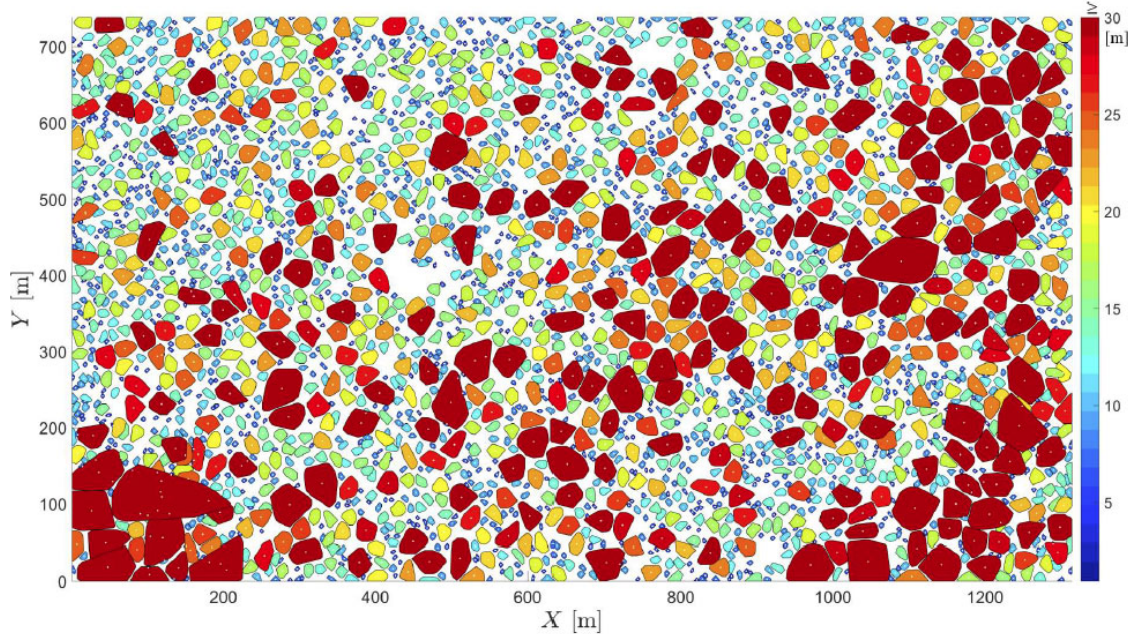


Figure 2.7: Digitalized ambient broken ice field, within which, a glacial ice feature can be embedded (different colours represent ice floes' sizes).

2.1.3.2 Glacial ice features

This section mainly reviews the properties of icebergs in Block A. However, it is emphasized that ST19 mainly concerns glacial ice features with a diameter less than 15 m. For simplicity, one refers to these

small glacial ice features in the rest of this report as *ice features*. Most of the existing knowledge and statistical information about ‘conventional’ icebergs are relevant, but might not be directly applicable to the glacial ice features’ impact study in this project. For example, an ice feature’s encounter frequency as described below:

For the selected study site, Block A, the encounter frequency of icebergs with a mean waterline diameter of 40 m within different considered zones are illustrated in Table 2.4. However, as cautioned by Eik and Dezecot (2016), the encounter frequency presented in Table 2.4 has significant uncertainties and the reality can be a magnitude higher or lower. Eik and Dezecot (2016) also stressed that a proper iceberg management can reduce the encounter frequency by as much as 80-90%.

For the ST19 study’s target, i.e., an ice feature with a diameter smaller than 15 m, there are no numbers regarding its encounter frequency at the study site. However, comparing to icebergs, the ice features of concern are viewed as a potential threat as it is generally more difficult to detect and monitor them besides the challenges in applying existing iceberg management methods due to its small size. The ST19 study does not further investigate the encounter frequency of the ice features of concern. All the forthcoming analysis are based on an assumption that impacts have already happened given the associated wave and current conditions; and we further analyse the consequences of such impacts. As to how often such impact events occur, it is considered beyond the scope of this project, and further studies based on best available data and some physically based simulations (i.e., ‘ice feature drifting patterns’ and ‘thermal and mechanical degradation process’) can offer a better insights on such accounts.

Table 2.4: Annual iceberg encounter frequency at Block A, after (Eik and Dezecot, 2016).

External diameter of zone (m)	Mean iceberg drift speed, m/s	Mean iceberg waterline length, m	Mean areal density, ρ_D	Annual number of iceberg encounters, η_E
Block A				
100				$5.20 \cdot 10^{-4}$
500				$1.93 \cdot 10^{-3}$
1000	0.44	48	$2.5342 \cdot 10^{-13} \text{ m}^{-2}$	$3.69 \cdot 10^{-3}$
4000				$1.42 \cdot 10^{-2}$
8000				$2.83 \cdot 10^{-2}$

2.2 Review of ST5

2.2.1 ST5 tasks

The work carried out in ST5 can be largely separated into two parts. The first part focuses on the hydrodynamic analysis and the second part deals with the impact simulation and damage assessment. The hydrodynamic analysis is mainly to study the relative motion of an ice feature and a structure in different sea states. The relative motion is further interpreted as the potential impact heights and velocities between an ice feature and a semi-submersible structure. The structural analysis part focuses

more on the local damage assessment given the impact energies derived from the results in the first part study.

Some key numbers of ST5 can be summarised in the following¹:

In terms of hydrodynamic analysis:

- 2 ice feature geometries (spheroid and cuboid);
 - 3 different waterline diameters for the ice features;
 - 3 different sea states (Table 4);
 - 1 wave direction or 1 ice feature – platform interaction arrangement (Figure 8);
 - 2 methods (i.e., frequency domain multi- and single body analysis (Figure 8); and time domain single spheroidal body analysis (Figure 15)).

6 different cases in Table 3

In terms of structural analysis:

- 1 impact location on 1 selected structure (Figure 29 - 31);
 - 1 impact direction (Figure 8);
 - 2 methods to evaluate the structural deformation during the impact (i.e., the ice feature as a rigid body in Figure 37 and applying a uniform pressure on a pre-defined area in Figure 43).

2.2.2 ST5 major findings

Detailed descriptions of the work carried out in ST5 can be found in the original report (Ekeberg et al., 2018). Major findings from ST5 are summarised herein:

From Phase #1:

1. Though all facilities operating on the Norwegian continental shelf are designed for ship impact, this might not be applicable/relevant to sea ice and ice feature impact with respect to the impact locations and energy levels.

From Phase #2:

1. Due to wave conditions, the vertical extent of impacts on the semi-submersible structure can be beyond ship impact regions (e.g., Table 7 shows the impact range -10.8 m to +10.8 m from the reference point of the spheroidal ice feature).
 2. The ice feature can protrude and collide with the structure elements which are not re-enforced for ship impact (Figure 23).
 3. More than 1.5 m horizontal penetration can take place due to ice feature impact (Table 15).
 4. Uncertainties related to the pressure-area formulation that is used to estimate ice feature load should be considered.

The previous studies also identified several topics that should be addressed in the future. They are summarised below:

¹ Figure number and table number presented in this list are with reference to the report (ST5) of Ekeberg et al. (2018).

From Phase #1:

Further work to understand:

1. Ice – structure interaction during broken ice conditions,
2. The mechanics of ice feature impacts and its associated uncertainties.

From Phase #2:

3. Propose limits for the vertical extent of damage to be considered (with relation to Conclusion #2).
4. Conclude on the uncertainties involved in the pressure-area relationship (similar to Conclusion #5).

2.2.3 Comments on ST5

Previous in ST5, there is no information about mean drift velocity (mainly due to current and second order wave drift forces) for the ice feature in ST5. The ice feature needs to have a mean drift velocity to approach the structure, and the impact velocity distribution will ‘skewed’ towards larger velocities than the drift velocity distribution if the mean drift velocity is large compared to the standard deviation, otherwise it may be ‘skewed’ towards smaller velocities (no impact can happen with “negative” velocities). This has been considered for drifting vessels (Fylling, 1994). ST5 investigates the first order wave induced relative velocity between the ice and the column in detail, but discusses the relation between impact velocity, drifting velocity and impact location (vertical extent) quite briefly; more detailed investigations could be performed on this issue. This is mainly achieved in Chapter 3 of the current report.

For damage assessment in ST5, different methods were adopted. Figure 2.8 illustrates these methods. NLFEM analysis was conducted for a vertical column of a given structure designed for operation in the Barents Sea, subjected to impact from rigid, spheroidal ice features of varying sizes. Thus, crushing of the ice was neglected, but the interface pressure for the simulations (governed by the structural resistance) was compared with the pressure-area relationships given in ISO 19906. It was found that for small indentations/contact areas the ice crushing pressure exceeded by far the structural resistance, but for larger indentations/contact areas the structural resistance could exceed the crushing pressure especially for larger ice spheroids, thus forcing the ice to deform and dissipate energy. This was neglected in the analysis, partly because of the uncertainties in the pressure-area characteristics. The approach adopted is conservative and sometimes very conservative; once, the ice starts to crush the contact area increases and the structure becomes even stronger.

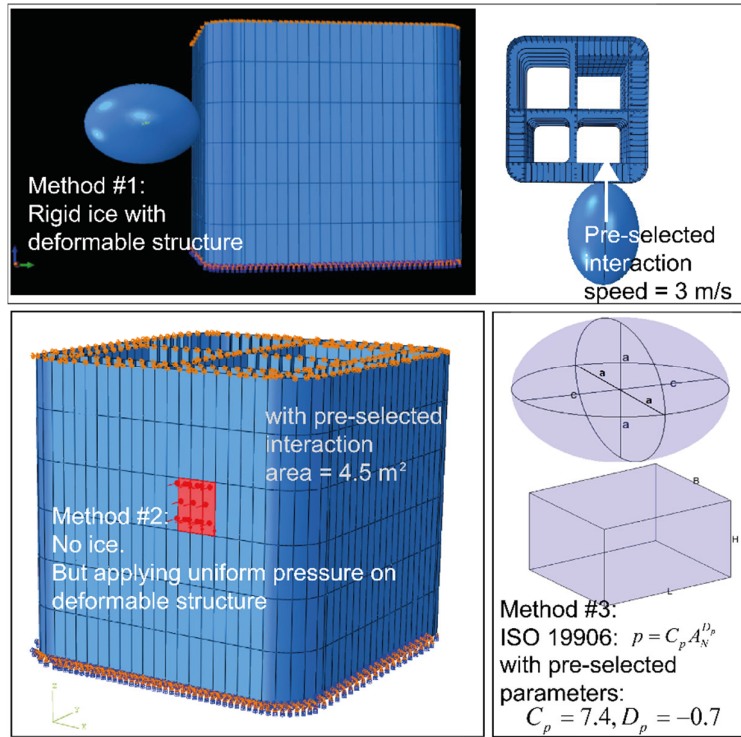


Figure 2.8: Analysis methods in ST5 regarding ice feature impact.

The findings here are in perfect match with results from ship impact analysis; if a rigid bow or rigid ice feature is assumed, the shape of the bow/ice is extremely crucial with respect to energy dissipation in the structure. An important issue is whether the ice crushing characteristics according to the local design with (power law with $C_p = 7.4$ and $D_p = -0.7$, ISO 19906) shall be adopted for the response analysis).

The draft version of the revised ISO standard 19906 lists the following local pressure area curves (see Sec. A8.2.5.4)

1. $p = 7.4A^{-0.7}$ based on data derived from indentation tests and full-scale measurements corresponding to the probability of exceedance 0.13% and assuming the data are normally distributed,
 2. $p = 9.6A^{-0.74}$ based on the same data as in pt. 1 and corresponding to the probability of exceedance 1%, and
 3. taking exposure into consideration, $p = 14.9A^{-0.7}$ and $p = 9.1A^{-0.7}$ pressure curves for 10^{-2} and 10^{-4} annual exceedance probabilities for three, 3.5 s impacts per year,
- where A is the local design area (confined area within a larger area exposed to ice action).

For comparison, for White Rose FPSO development ice pressures and contact areas for bow and side impacts corresponding to an annual probability of occurrence of 10^{-4} were taken as $p_{bow} = 6.24A^{-0.7}$ and $p_{side} = 4.59A^{-0.7}$, this is significantly lower than those listed in ISO 19906. More detailed investigation of the uncertainties related to the choice of the pressure-area relationship could be performed in view of damage assessment of the column.

It is noticed that the column of the structure used in the analysis of ice impact does not differ significantly from column conceptual design of similar structures in the North Sea (the “Gjøa” and “Midgard” structures), so the extent of ice strengthening is uncertain. In previous projects it was found that the columns of “Gjøa” and “Midgard” in most cases were able to crush the bulb of a conventional vessel with no rupture of shell plating with a small margin (Tavakoli and Amdahl, 2010).

It is stated that the selected column (and pontoon) is designed for ship impact with kinetic energy 11-14 MJ. It is not stated whether the design impact vessel is un-strengthened or ice-reinforced. The crushing resistance of the bow of an ice-strengthened vessel will exceed that of an un-strengthened vessel considerably. Thus, if the column is strong enough to crush the bow of an ordinary vessel, it might be subjected to severe penetration by an ice-strengthened bow requiring application of ductile design principles. In this case the shape of the bow becomes equally important as for the ice feature.

There is no information in the ST5 report about the scantlings on the inner side of column, which is not susceptible to ship impact, but might be hit by drifting ice. In this regard, extensive simulation with SAMS were carried out, see Chapter 4 in the current report, to study all possible impacts (including impact with inner sides of the column).

2.3 General considerations of ST19

The ST19 study focuses on the impact between an ice feature and a semi-submersible structure and its associated damage assessment. The impact characteristics depend upon several factors:

- The geometry of the structure and the ice feature,
- The mean drift of the structure and the ice feature caused by currents, wind and waves,
- The oscillatory wave motion of the structure and the ice feature especially the surge/sway and heave motions-

For damage assessment, it is important to properly characterise the ice crushing process, which is further determined by the chosen design limiting state.

All these general considerations and the associated choices made in this study are described in this section.

2.3.1 Ice feature’s geometry

It is very important to distinguish between local and global geometry of the ice feature. The **global** geometry is decisive with respect to the mass of the ice feature as well as the exposure to impact of the various parts of the structure, i.e., the column and the floater. In addition it is important with respect to the demand for energy dissipation, which is expressed as a fraction of the total kinetic energy at the instant of impact. This concerns the so-called external mechanics dealt with in Chapter 4.

The **local** geometry is essential with respect to the resistance of the ice to deformation (crushing, extrusion etc.) at the contact point. This is mainly dealt with in Chapter 5.

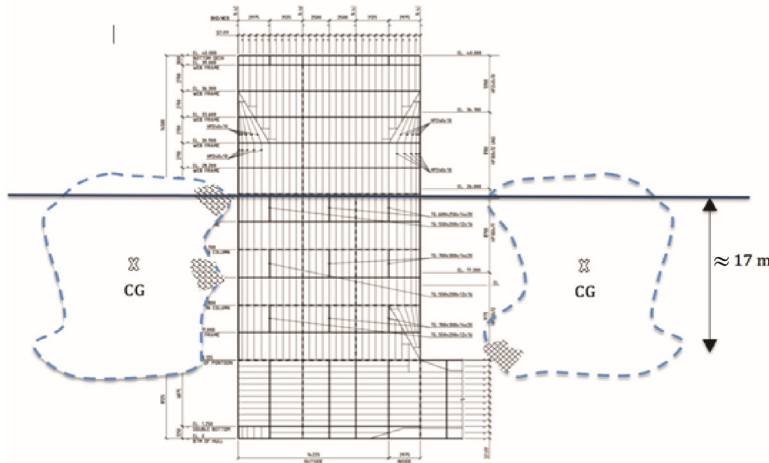


Figure 2.9: Illustration of global geometry for impact between a ‘large’ ice feature and structure’s column and pontoon in still water. The hatched areas indicate possible contacts where crushing will take place and where information of local geometry is needed. The ‘large’ ice feature is around 5000-10000 tons.

Figure 2.9 illustrates the importance of global geometry for exposure of column and pontoon at still water (or relatively small waves). The pontoon can only be hit by a ‘large’ ice feature at still water. The impact will in most case be eccentric, i.e., the force vector has a large arm with respect to the centre of gravity (CG), and substantial energy may be transferred into pitch/roll motion of the ice feature. This reduces the demand for energy dissipation. The same holds true for impacts around water level.

Depending on the ice features shape, impact may take place at intermediate depths and may be close to the CG; and most of the kinetic energy must be dissipated by deformation of structure and/or the ice feature.

For smaller ice features, like the spheroidal ice feature in Figure 2.10, only the column may be exposed to impact, which in this case is centric. It is true that the mass of the ice feature here is small; but it is also prone to larger wave induced motions leading to considerable impact velocities.

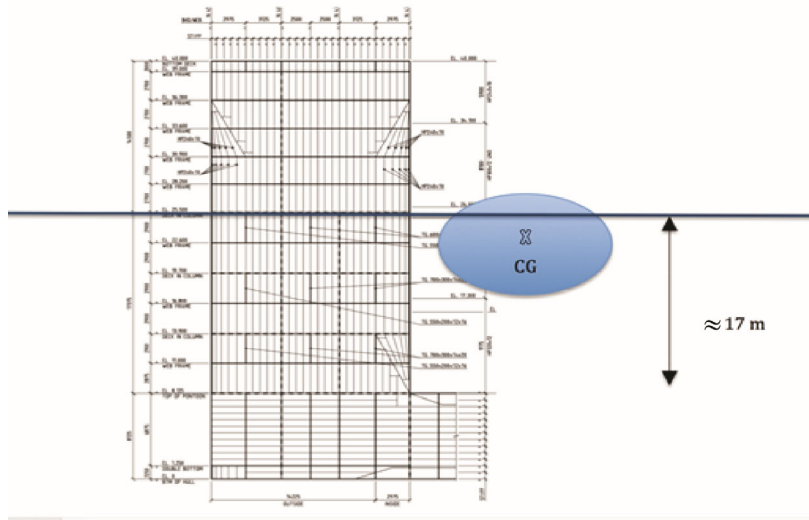


Figure 2.10: Illustration of global geometry for impact between a ‘small’ ice feature and structure’s column in still water. The ‘small’ ice feature is around 500-1000 tons.

The previous project ST5 studied two ice feature geometries, i.e., a spheroidal and a cuboidal geometry of various sizes. These geometries might be representative when it comes to calculate the global response or impact energy during the impact. We also see that similar results were obtained for these two different geometries with the same waterline size. However, the local geometry of the ice feature can have a large variety, which can further lead to various conclusions concerning the amount of local damage. In ST5, the spheroidal geometry is utilised in the NLFEM for damage assessment.

As a continuation of ST5, we choose the spheroidal ice feature in Figure 2.11 for both the global (i.e., external mechanics) and local analysis (i.e., damage assessment). It is cautioned here that a different geometry can have a significant influence on the local damage assessment (see Chapter 5).

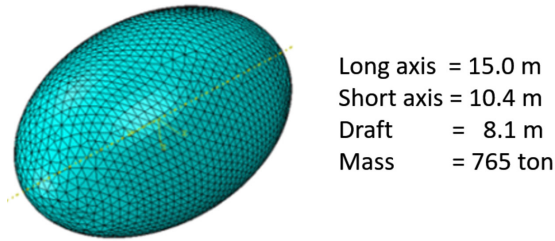


Figure 2.11: Geometry and size of the spheroidal ice feature mainly used in the ST19 study.

2.3.2 Relative motions

The presence of waves induces oscillatory motions in six Degrees of Freedom (6DoFs) for both the ice feature and the structure. This is important to determine the range of impact height. Depending on the motion characteristics, the vertical exposure of the structure will vary in different wave conditions. This is illustrated in Figure 2.12.

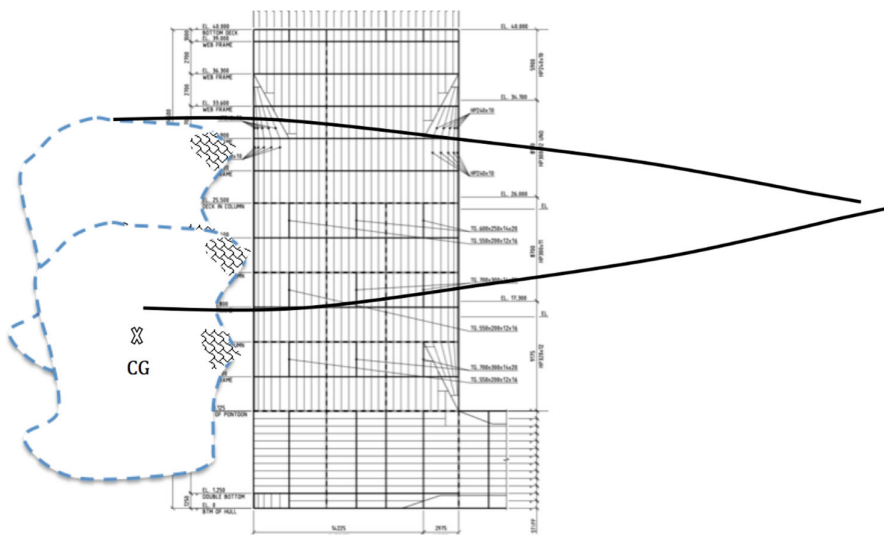


Figure 2.12: Illustration of potential global geometries for impact between 'large' ice feature (5000-10000 tons) and the structure's column and pontoon in waves. Upper sketch for high position impact close to wave crest, lower sketch for low position impacts close to wave trough.

If only the horizontal motions of the ice are considered, the likelihood of hitting the pontoon in a wave trough will most likely be considerably smaller than the likelihood of hitting the column in a wave crest.

This depends on the mean drift of the ice feature versus standard deviation of the **relative** wave induced surge/sway motion of the ice feature and the structure.

On the other hand, vertical impact on the pontoon due to the relative heave motions can be significant. In ST5, only the impacts due to horizontal motions of the ice (i.e., sway direction impact) were studied. Ther ST19 study carried out analysis of both the horizontal and vertical impact, which are described in Chapter 3.

2.3.3 Design limit state and ice crushing considerations

Ice crushing plays an important role during ice – structure interactions. There are many ways to characterise the ice crushing properties, e.g., the design Pressure-Area (P-A) curves mentioned in Section 2.2.3 and process P-A curves (to be discussed in Section 5.2.3). The *design P-A curves* are often viewed in the context of local or global ice loads and in the context of probabilistic or deterministic approaches to design. The *process P-A curves* (termed by Frederking (1998)) describe the process of a structure penetrating into an ice feature or of an ice feature hitting a structure. It is continuous plot of pressure versus nominal contact area variation during an ice-structure interaction process.

The choice on how we characterise the ice crushing process is again influenced by the chosen design limiting state. Generally, we have the Ultimate Limit State (ULS), in which, the designed structure is supposed to undergo only elastic or small plastic deformations for the given impact. For the internal mechanics shown in Figure 2.13 (i.e., local damage assessment), when the structure is not allowed to deform, localised high pressures can develop anywhere in the contact area and they govern the local design for the ULS state. This contact pressure can be characterised by the design P-A relationships commented in Section 2.2.3.

On the other hand, for the ALS, the structure is permitted to undergo substantial plastic deformations given an ice impact. In this case, it is the crushing process, not the peaks of the crushing force that are of interest. Because the structure in direct contact are most likely to ‘give in’, the contact force peaks due to localised high pressures, as in the ULS scenario, are not applicable herein. Instead, it is the overall process (without the formation of localised high pressure zones) that governs the contact force. It is the ALS condition that is focused here. Therefore, the impact studies carried out in this project are following the ALS design principles when it comes to characterising how the ice crushes and its associated contact force.

The ST19 study carries out two separate but interconnected tasks, i.e., the external mechanics analysis, in which, the demand for energy dissipation is calculated for any impact leading to the creation of an energy map (see the left of Figure 2.13); and the internal mechanics, in which, damage assessment is carried out on a deformable structure (see the right side in Figure 2.13).

Within the internal mechanics, two limiting cases shall be studied, i.e., NLFEM of a rigid ice colliding with a deformable structure; and SAMS simulations of a crushable ice feature against a rigid structure. For the NLFEM analysis with rigid ice, all available energy is dissipated by the structure. For the SAMS simulations, the Constant Specific Energy (CSE) approach is utilised to characterise the energy dissipation in the ice during crushing (alternatively, the process P-A curve (see Section 5.2.3) can also be utilised to characterise the energy dissipation during ice crushing process). The combined results of these two limiting scenarios will enable the quantification of energy dissipation in structural deformation and the consequent structural damage.

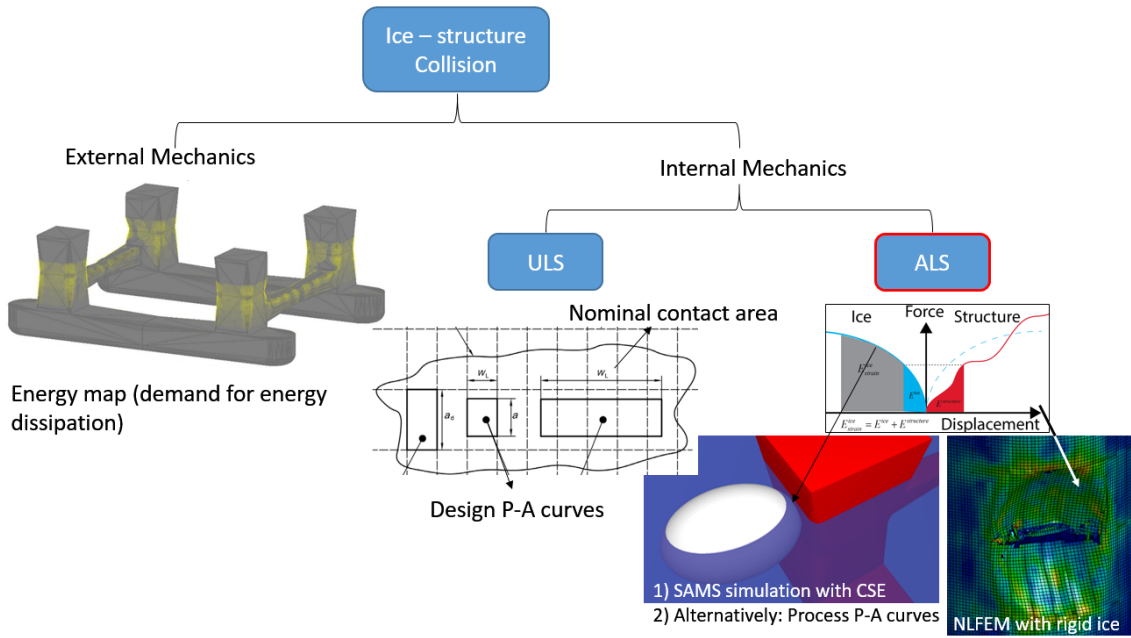


Figure 2.13: Illustration of the design limit states and ice crushing considerations.

In summary, instead of using design P-A curves, i.e. for a given contact area to calculate the ice pressure at a certain exceedance level (as commented in Section 2.2.3 and also that was carried out in ST5), the ST19 work selects a different approach to analyse the crushing of the ice feature; namely using the *CSE* method for SAMS simulations; or using the process P-A curve as a simplified approximation to yield a physically plausible value of energy absorbed per unit volume of crushed ice (see Chapter 5).

3 Analysis of Impact Events

This chapter describes the method adopted to derive the correlated impact velocities and heights, which are important inputs to scale SAMS simulation results (Task #2) and thereby identify critical impact locations and the associated energy for damage assessment (Task #3).

Work carried out in this chapter was initially beyond the scope of ST19 and the intention was to build directly upon ST5 results. However, along the course of scaling SAMS' simulation results based on ST5, we realised that ST5 estimated impact velocities are rather conservative; and the impact velocity and height are uncorrelated. In order to derive a less conservative impact velocity and its correlated impact height, a similar method to those of (Amdahl, 1980) and (Fylling, 1994) for drifting ship impacts with a floating platform was adopted.

Most of the frequency domain simulated results from ST5, i.e., Response Amplitude Operators (RAOs), were utilised for further analysis in this chapter. Detailed methods, procedures and results are presented in the following.

3.1 Uncorrelated impact velocity and height from ST5

In ST5, frequency domain multi-body analysis were carried out and the Response Amplitude Operators (RAOs) were derived for both the ice feature and the structure. Particularly, the RAOs for the structure and the ice feature are re-summarised in Figure 3.1 and Figure 3.2, respectively.

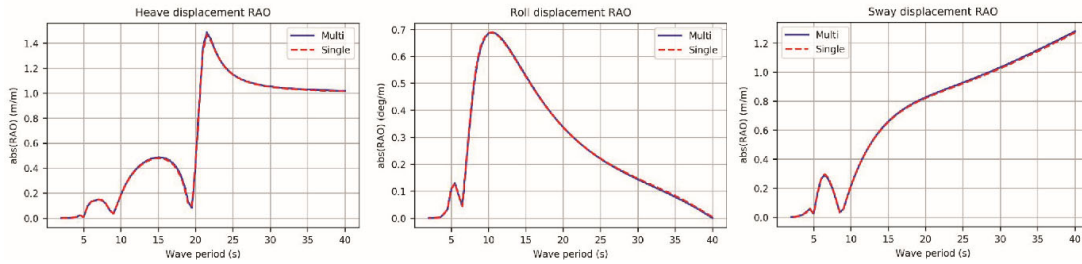


Figure 3.1: RAOs of the structure in heave $|H_3^{ps}(\omega)|$, roll $|H_5^{ps}(\omega)|$ and sway $|H_2^{ps}(\omega)|$ directions; definition of directions and results are originally from Figure 5 and 9a) of ST5 (Ekeberg et al., 2018).

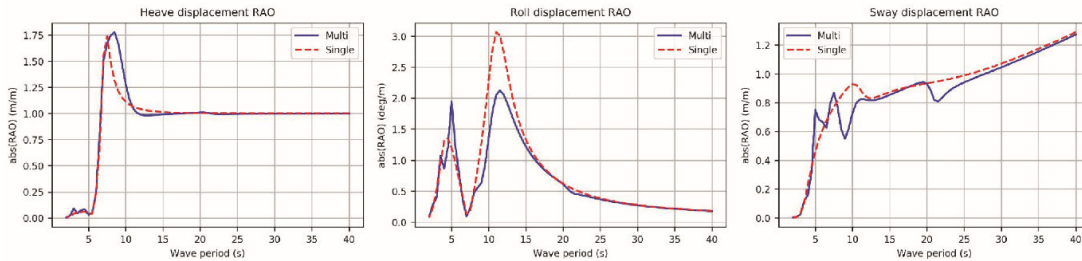


Figure 3.2: RAOs of the spheroidal ice feature in heave $|H_3^{pi}(\omega)|$, roll $|H_5^{pi}(\omega)|$ and sway $|H_2^{pi}(\omega)|$; definition of directions and results are originally from Figure 5 and 10a) of ST5 (Ekeberg et al., 2018).

Knowing the responses of the structure and the ice feature (in Figure 3.1 and Figure 3.2), the relative heave displacement and relative sway velocity can be easily established in Figure 3.3.

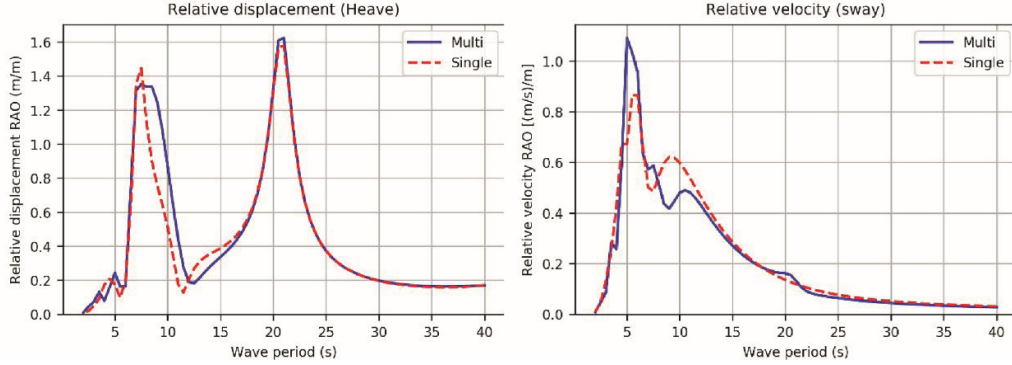


Figure 3.3: RAOs of the relative motions between the spheroidal ice feature and the structure. Results are originally from Figure 12a and 13a of ST5 (Ekeberg et al., 2018).

Both the multi-body (both the ice feature and the structure), and single-body simulations were carried out in ST5. The ST19 study focuses on the multi-body simulation results as they are more relevant to the impact scenarios.

Both the relative vertical displacement and sway velocity between the ice feature and the structure are presented in Figure 3.3. Each plot in Figure 3.3 represents the maximum absolute values of relative heave and relative sway velocity for different wave components with different wave period (or frequency). There is, however, no correlation between the left and right plots in Figure 3.3. In other words, given the same wave component, the impact height (in the left plot) and impact velocity (in the right plot) are not likely to be maximum values at the same time as presented in Figure 3.3.

Figure 3.3 is re-established considering the height-velocity correlation in the following, based on results from Figure 3.1 and Figure 3.2, and time-domain simulations.

3.2 Relative motion in a single wave component

Before the results for a complete sea state are presented, let us take a look at a simpler case, i.e., motions of a body in a harmonic single wave component. For a single wave component with frequency ω , wave number $k = 2\pi / \lambda$, wave length $\lambda = 1.56(2\pi / \omega)^2$ and a random phase angle ϕ , its vertical elevation at different location x can be written as in Eq. (3.1). Here the phase angle ϕ is a random number uniformly distributed between 0 and 2π .

$$\eta_v = \eta_0 \cos(\omega t - kx - \phi) \quad (3.1)$$

Similarly, a surface wave particle's horizontal displacement can be written as in Eq. (3.2).

$$\eta_h = \eta_0 \sin(\omega t - kx - \phi) \quad (3.2)$$

The motion of a body in such a harmonic wave component can be calculated with its associated RAOs functions presented in Figure 3.1 and Figure 3.2.

For two bodies, e.g., the ice feature and the structure, without losing generality, we can define the original location of the structure at $x=0$, and the location for the ice feature at $x=-(L^{P_s} + L^{P_i})$, see Figure 3.4 for the interpretation of symbols. Here, we can select two reference points P_i and P_s on the ice feature and on the structure, respectively. It is mainly their relative motion that is of interest. Figure

3.4 illustrates one possible definition of the reference points and their relative motion in a long wave with crest right at the $x=0$ point of the coordinate system. Notably, when there is no wave, P_i and P_s coincide with each other at Still Water Level (SWL).

With the above definitions and available RAOs, the heave motion of point P_s with reference to the centre of the platform's water plane at SWL is written in Eq. (3.3).

$$\eta_s^{ps} = |H_5^{ps}(\omega)|\eta_0 \cos(\omega t - kx - \phi) + L^{ps} |H_5^{ps}(\omega)|\eta_0 \cos(\omega t - kx - \phi) \quad (3.3),$$

in which, L^{ps} is the ‘arm length’ of the reference point P_s ; and the roll motion induced vertical motion is taken into account by multiplying the roll angle $|H_5^{ps}(\omega)|\eta_0 \cos(\omega t - kx - \phi)$ by this arm length.

Similarly, point P_i ’s heave motion with reference to the centre of the ice feature’s water plane at SWL is written in Eq. (3.4).

$$\eta_i^{pi} = |H_5^{pi}(\omega)|\eta_0 \cos(\omega t - kx - \phi) + L^{pi} |H_5^{pi}(\omega)|\eta_0 \cos(\omega t - kx - \phi) \quad (3.4)$$

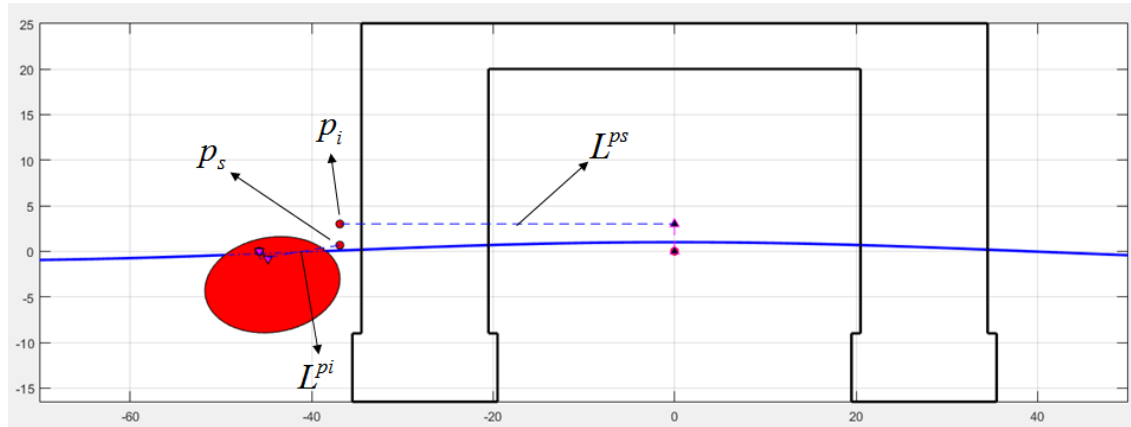


Figure 3.4: Definitions of symbols and the relative motion (sway and heave) between the ice feature (red) and structure (dark frames) in a relatively long wave component.

Thus the relative vertical displacement among the two bodies can be written as in Eq. (3.5).

$$\Delta \eta_s = \eta_s^{ps} - \eta_i^{pi} \quad (3.5)$$

For a floating body’s sway displacement, one needs to use the water particle’s horizontal motion (Eq. (3.2)) as the excitation together with the RAOs in the sway direction, i.e., $H_2(\omega)$. Generally, the sway displacement of a floating body can be written in Eq. (3.6), whose one time derivative leads to the sway velocity in Eq. (3.7).

$$\eta_2 = |H_2(\omega)|\eta_0 \sin(\omega t - kx - \phi) \quad (3.6)$$

$$\dot{\eta}_2 = \omega |H_2(\omega)|\eta_0 \cos(\omega t - kx - \phi) \quad (3.7)$$

Eq. (3.7) shows that the sway velocity is in phase with the heave motion of wave in Eq. (3.1), i.e. the maximum sway velocity is attained when the heave motion is maximum.

The sway velocity for the structure and ice feature are written in Eqs. (3.8) and (3.9), respectively. For simplicity the roll motion's contribution to the sway velocity at the reference point is excluded, and at the same time not sacrificing too much accuracy.

$$\dot{\eta}_2^{ps} = \omega |H_2^{ps}(\omega)| \eta_0 \cos(\omega t - kx - \phi) \quad (3.8)$$

$$\dot{\eta}_2^{pi} = \omega |H_2^{pi}(\omega)| \eta_0 \cos(\omega t - kx - \phi) \quad (3.9)$$

The relative velocity between the ice feature and the structure is given by Eq. (3.10):

$$\Delta \dot{\eta}_2 = \dot{\eta}_2^{pi} - \dot{\eta}_2^{ps} \quad (3.10)$$

3.3 Relative motion in a sea state with random waves

Eqs. (3.5) and (3.10) characterise the relative motions between two floating bodies, namely the ice feature and the structure, for a single wave component. Such a wave component can be considered having a wave frequency of ω_i in a sea state characterised by a JONSWAP wave spectrum in Figure 3.5. The spectrum is discretised into a number of regular waves with associated amplitude, as shown in Figure 3.5.

Based on the wave condition at Block A (described in Section 2.1.1) and ST5's study (see Figure 7 in ST5), we choose a sea state in Figure 3.5. It corresponds to the sea state in Figure 2.3 with a peak wave height of $H_s = 13.8$ m and the $H_s - T_p$ contour plot with a 100-year return period (i.e., $q = 10^{-2}$). The selected sea state is defined as Sea State #3 in the studies carried out in ST5.

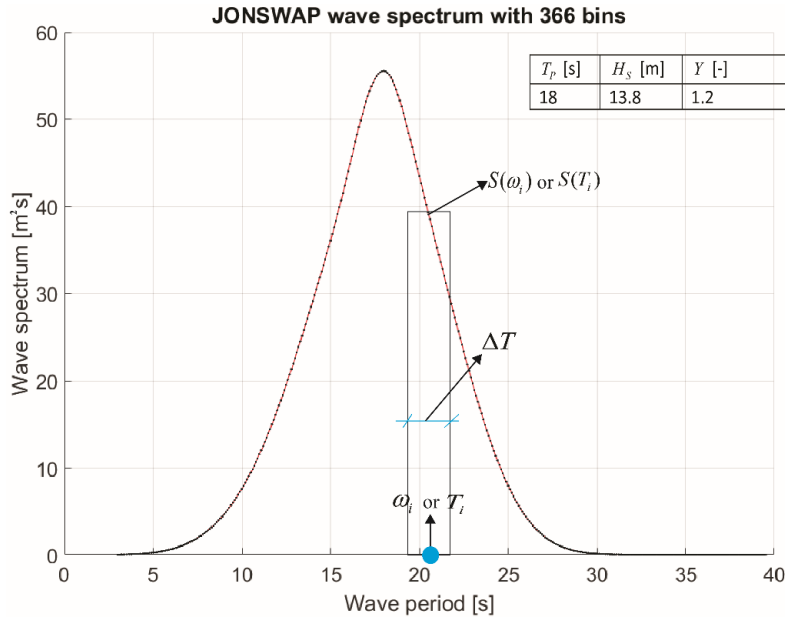


Figure 3.5: Selected sea state with an exaggerated bin width for definition of symbols (Note that this is the same Sea State #3 in ST5).

As concluded in ST5, Sea State #3 leads to the maximum impact range in the vertical direction (e.g., see Table 7 and the top plot of Figure 24 in ST5), and only a slightly lower impact velocity than Sea State #2 (e.g., see Table 8 and the lower plot of Figure 24 in ST5). Considering the severe consequences

in both impact height and velocity (even though slightly lower than Sea State #2), we consider Sea State #3 in ST5 is sufficiently representative; and all forthcoming analyses are based on this sea state.

Given the responses (re-written in Eq. (3.11)) from each single wave component ω_i with a wave height of η_i , one can write the overall response in Eq. (3.12).

$$\text{Relative heave displacement} \rightarrow \Delta\eta_{i,3}(\eta_i, \omega_i) = \eta_{i,3}^{ps}(\eta_i, \omega_i) - \eta_{i,3}^{pi}(\eta_i, \omega_i)$$

$$\text{Relative sway velocity} \rightarrow \Delta\dot{\eta}_{i,2}(\eta_i, \omega_i) = \dot{\eta}_{i,2}^{pi}(\eta_i, \omega_i) - \dot{\eta}_{i,2}^{ps}(\eta_i, \omega_i)$$

Individual wave height for wave component i with angular frequency ω_i is (3.11)

$$\text{given} \rightarrow \eta_i = \sqrt{2S(\omega_i) \cdot \Delta\omega} = \sqrt{2S(T_i) \cdot \frac{2\pi}{T_i^2} \cdot \Delta T}$$

$$\Delta\eta_{Total,3} = \sum_{i=1}^N \Delta\eta_{i,3} \quad (N \text{ is the number of bins in Figure 3.5}) \quad (3.12)$$

$$\Delta\dot{\eta}_{Total,2} = \sum_{i=1}^N \Delta\dot{\eta}_{i,2} \quad (N \text{ is the number of bins in Figure 3.5})$$

With all the previous formulas and discretisation of the wave spectrum, one obtains time series of relative heave displacement $\Delta\eta_{i,3}(t)$ and relative sway velocity $\Delta\dot{\eta}_{i,2}(t)$ for each wave component. After the summation, one also obtains the total relative heave displacement $\Delta\eta_{Total,3}(t)$ and total relative sway velocity $\Delta\dot{\eta}_{Total,2}(t)$.

First the simulation results are presented for the one wave component (Eq. (3.11)) in Figure 3.6 and Figure 3.7.

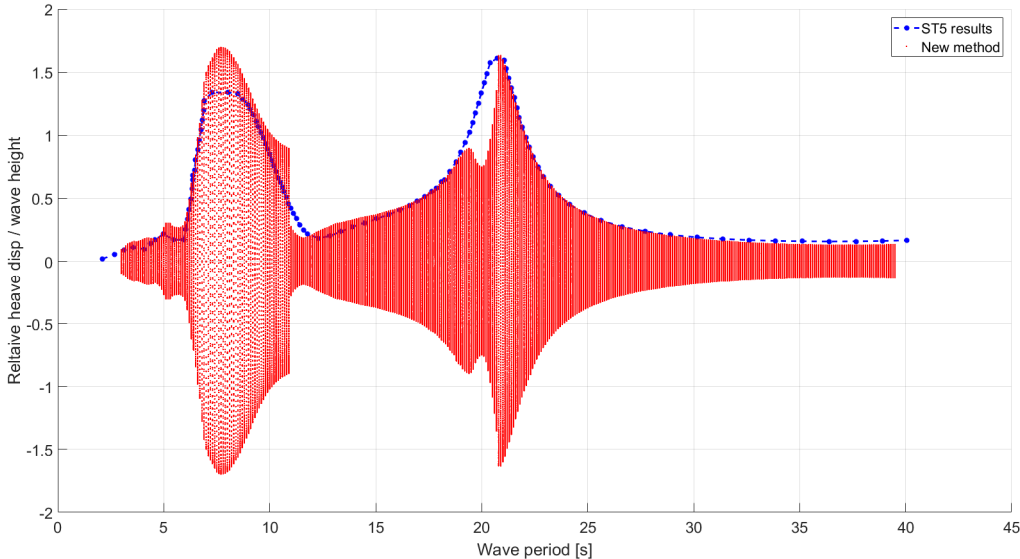


Figure 3.6: Relative heave displacement: time domain simulated results for each wave component (i.e., New method) comparing with ST5 results in frequency domain.

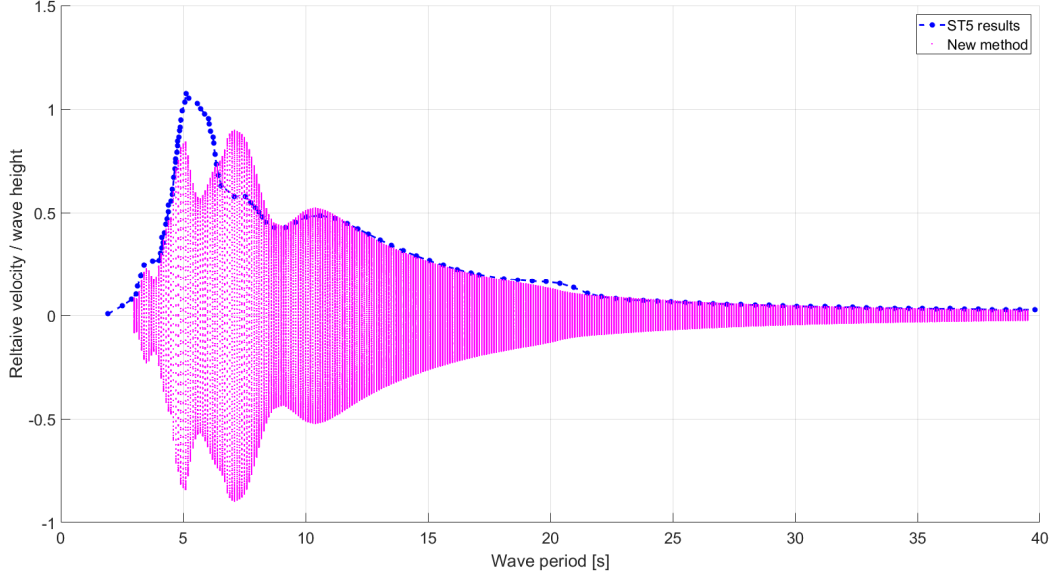


Figure 3.7: Relative sway velocity: time domain simulated results for each wave component (i.e., New method) comparing with ST5 results in frequency domain.

Each point in Figure 3.6 and Figure 3.7 represents a value of $\Delta\eta_{i,3}(\eta_i, \omega_i)$ and $\Delta\dot{\eta}_{i,2}(\eta_i, \omega_i)$, respectively. Most importantly, there is a one-to-one correlation between the simulated point in Figure 3.6 and Figure 3.7. In addition, given the same wave frequency/period, the maximum simulated results in Figure 3.6 and Figure 3.7 correspond well with the frequency domain based simulation in ST5. Small discrepancy can be found, which are most likely due to some discretisation errors in the RAOs in Figure 3.1 and Figure 3.2, different damping coefficients used in our simulation and our disregard of the roll motion component of the sway velocity. Generally speaking, the maximum response from both methods are in favourable agreement, which indicates the correctness of the method. However, the advantage of this method is that, correlated ‘impact height (quantified by $\Delta\eta_{Total,3}$)’ and ‘impact velocity (quantified by $\Delta\dot{\eta}_{Total,2}$)’ are obtained.

3.4 Sampling of impact events

After obtaining the relative motions between the ice feature and the structure in time domain, one needs to sample relevant impact events for our statistical analysis. Here, let us consider two different types of impacts, i.e., the impact in the sway direction, where the relative sway velocity $\Delta\dot{\eta}_{Total,2}$ and corresponding relative vertical motion $\Delta\eta_{Total,3}$ matter.

Another type of impact may take place in the vertical direction, i.e. a scenario where the ice feature heaves vertically upon the pontoon or any other structural component (e.g., a horizontal brace) due to the relative heave motion.

These two different impact events are treated separately, with major focus on the horizontal impact (or impact in the sway direction) and its associated simulations by SAMS and NLFEM analysis. For impacts in the vertical direction, we only derive the statistics of the impact velocity, whereas no further damage assessment is conducted for this scenario given the time constraint of this project.

3.4.1 Impact in the sway direction

3.4.1.1 Methods to sample horizontal impact events

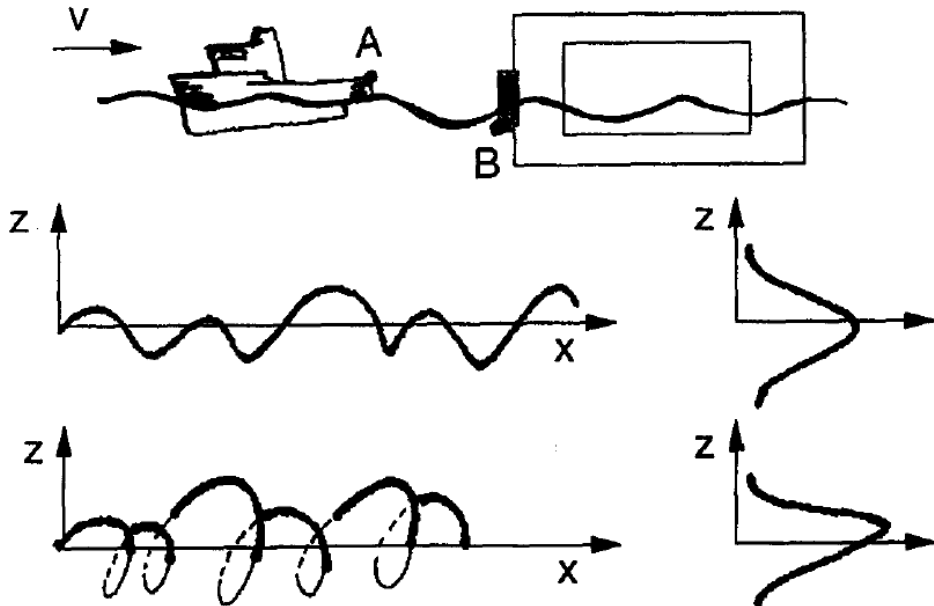


Figure 3.8: For ship and installation impacts (upper plot): sampling of impact events at high current velocity (middle plot) and low current velocity (lower plot), from Fylling (1994).

We adopt the same method that was introduced by Fylling (1994) for the analysis of ship impacts. When impacts in the horizontal direction is considered, it is necessary to include current velocity to ensure that the ice feature advances towards the structure. Simply put, if there is no current velocity, with reference to the structure, the ice feature is only moving back and forth, and will not hit the structure. The drifting ship impact scenario was described by Fylling (1994) by Figure 3.8. This can be well explained by Figure 3.8 for the scenario of ship (Body A) colliding with a structure (Body B) under the influence of current with a velocity of V . With a high current velocity, the middle plot in Figure 3.8 shows the trajectory (heave in ‘Z’ and sway in ‘X’) of the ship; and each point on this trajectory is a potential and valid impact event. However, with a smaller current velocity in the lower plot in Figure 3.8, the trajectory of the ship is swaying back and forth. In this scenario, only the advancing sway motions are sampled as valid impact events (bold black line); whereas the negative sway motions (in thin black line) and the shielded positive sway motions (in dashed black line) are not considered as valid impact events. Moreover, the sampling in both cases should be conducted with equal spacing in the sway direction, as when the ship approaches the structure, each point along the valid impact events trajectory (bold dark line) has an equal chance of impact.

Collectively, using his sampling method, the impact events tend to skew towards to higher locations and larger velocities (e.g., see lower plot in Figure 3.8).

3.4.1.2 Horizontal impact events

A current velocity of 0.79 m/s (see Table 2.3) with a 100-year return period is selected as the base number for sampling our impact events simulated in Figure 3.6 and Figure 3.7. First, out of around 2×10^7 simulated motion events, given the current velocity of 0.79 m/s, around 1.2×10^7 motion

events are sampled with positive velocity and non-shielded criteria in Figure 3.9. Each red circle in Figure 3.9 is the summed results of Figure 3.6 versus Figure 3.7, i.e., $\Delta \eta_{Total,3}$ versus $\Delta \dot{\eta}_{Total,2}$.

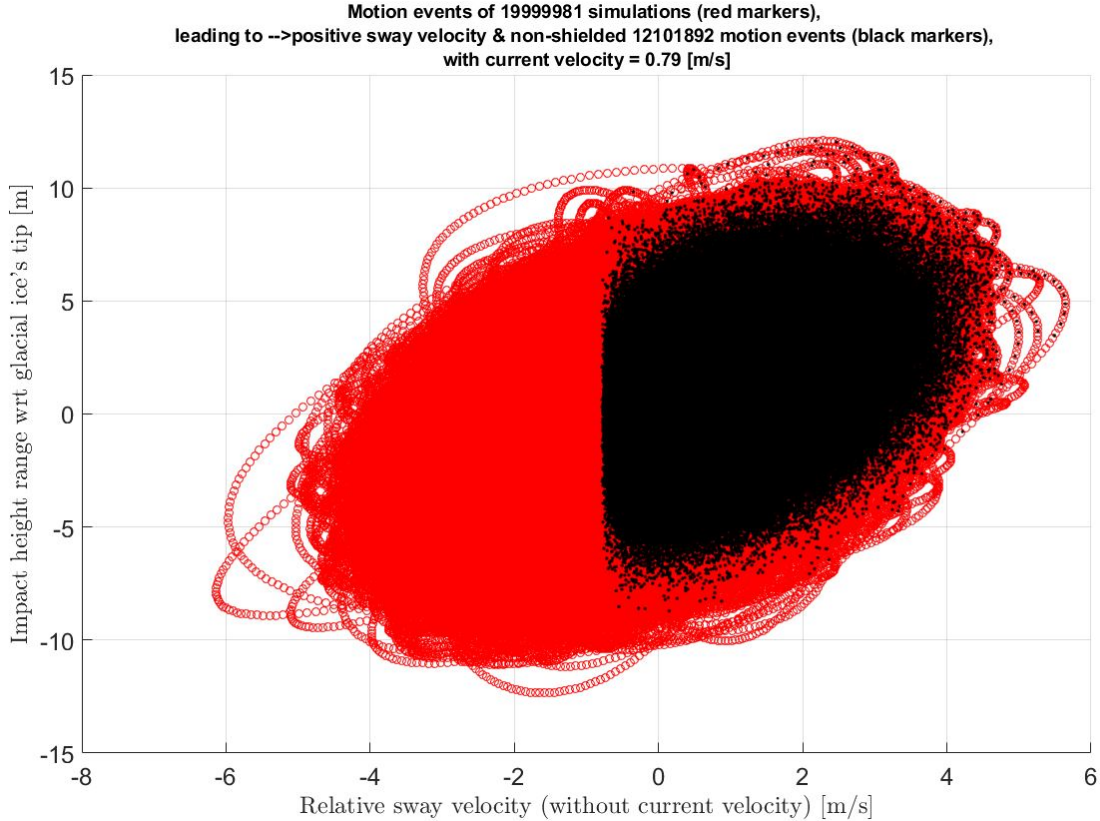


Figure 3.9: Step #1 impact events sampling: motion events with positive sway velocity and non-shielded events (dark points) are sampled out of all the simulated motion events (red circles).

Here, as our simulation is conducted in time domain, the sampled motion (dark points in Figure 3.9) are equally spaced in time. Namely, each consecutive sampled motions have the same time span in between. However, as the impact event at each location in the sway direction's trajectory has the same chance of impact, impact events should be sampled with equal sway displacement spacing in between. This is achieved via interpolation with a set of pre-defined equally spaced points in the sway displacement's direction to obtain their corresponding $\Delta \eta_{Total,3}$ versus $\Delta \dot{\eta}_{Total,2}$. In this regard, 1000000 impact events (green points) are further sampled in Figure 3.10.

These impact events contain correlated information of impact heights and velocities (i.e., $\Delta \eta_{Total,3}$ versus $\Delta \dot{\eta}_{Total,2}$), which will be the basis for the statistical analysis for the horizontal direction impact.

**Positive sway velocity & non-shielded 12101892 motion events (black markers),
leading to -->equally spaced 1000000 impact events (green markers),
with current velocity = 0.79 [m/s]**

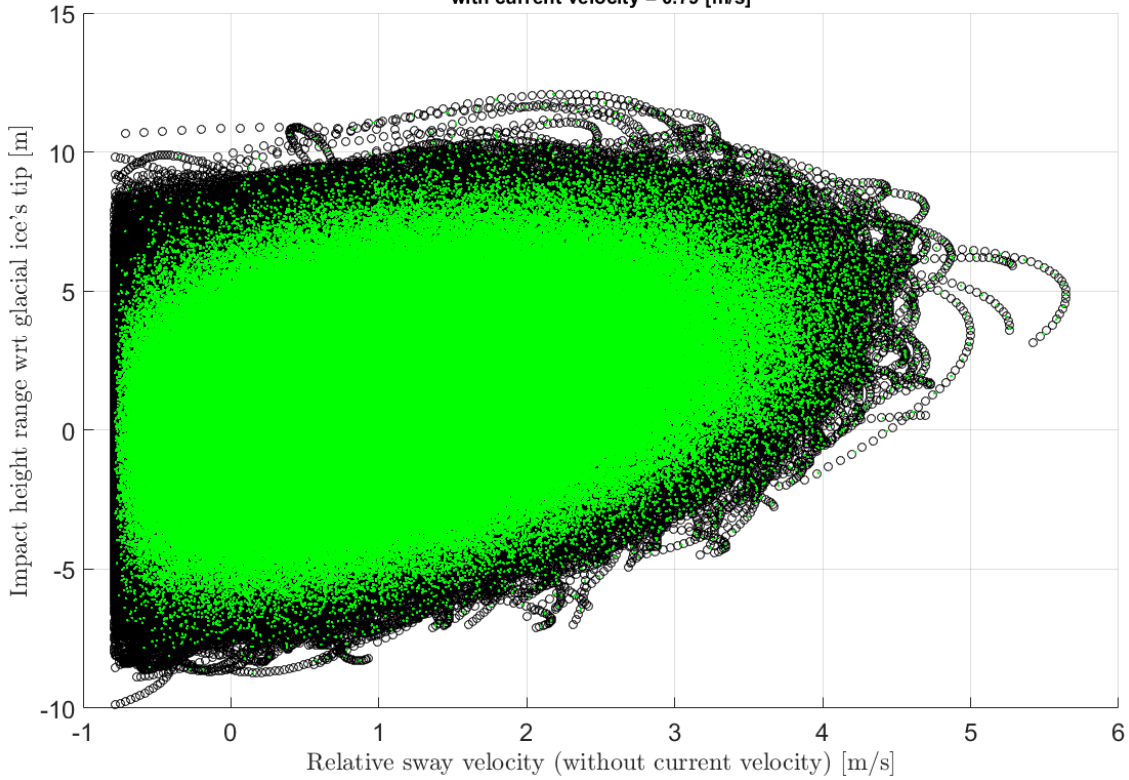


Figure 3.10: Step #2 impact events sampling: valid impact events with equal ‘sway displacement spacing’ (green points) are sampled from motion events with positive sway velocity and non-shielded events (dark circles).

3.4.1.3 Height range of horizontal impacts

For the sampled events for impact range in the vertical direction, its probability distribution together with the best-fit function are plotted in Figure 3.11. For the impact height, the best fit obtained is the Normal distribution with parameters listed in Table 3.1. Additionally, comparisons of the non-exceedance values obtained in this study are compared to those obtained in ST5. It shows that ST5 results are much larger. This is mainly because in ST5, it was the 3-hour maxima values (both for heights and velocities) that were used for statistical analysis. However, in the ST19 study, the statistical analysis are based on all the simulated impact events and one did not make an additional 3-hour maxima sampling of the sampled impact events in Figure 3.10. This is in line with the method proposed by Fylling (1994), who states: “*the transformed series represent samples of impact incidents with equal probability of occurrence. Hence, in a statistical interpretation, the fractiles of the distribution should be used directly to calculate impact states. This is in contrast to normal wave-induced motions and loads, where the distribution of maxima is used*”.

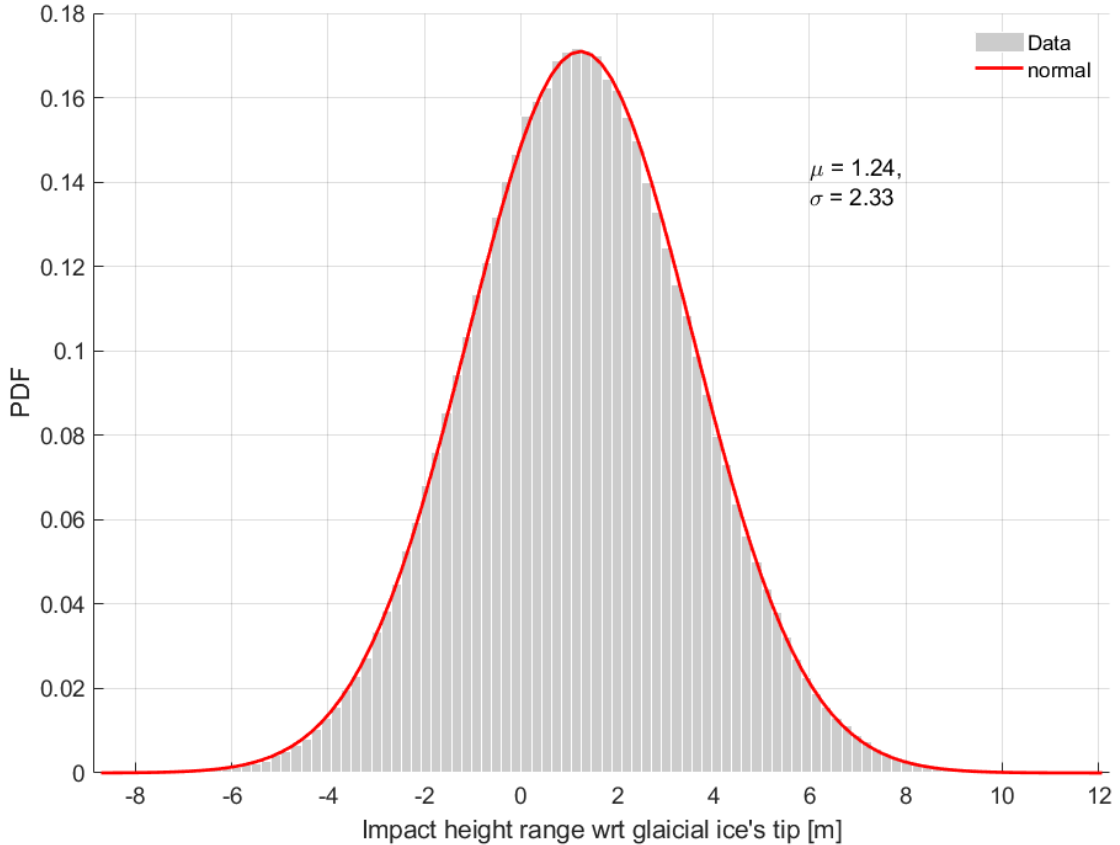


Figure 3.11: Statistical distribution of all sampled impact heights' values, unit: [m].

Table 3.1: All sampled impact heights' statistical values in this study comparing to results from ST5 (Note, impact events are sampled under the influence of a 0.79 m/s current velocity), unit: [m].

Non-exceedance level	50%	90%	99%	ST5 results	50%	90%
Normal distribution	± 1.8	± 4.4	± 6.7	Rayleigh distribution of 3-hour maxima values	± 9.6	± 10.8

3.4.1.4 Horizontal impacts' velocity distribution

Similarly, for all the sampled impact events' sway velocity, its statistical distribution are plotted in Figure 3.12 and Table 3.2. Again, without the 3-hour maxima value based statistics, impact velocities obtained in this study is much less than those obtained in ST5, even with the additional inclusion of a 100-year return current velocity of 0.79 m/s.

Aside from being less conservative, another advantage of the current new method is that the calculated impact height range and velocity are correlated. This means, one can make impact velocity statistics at different impact height.

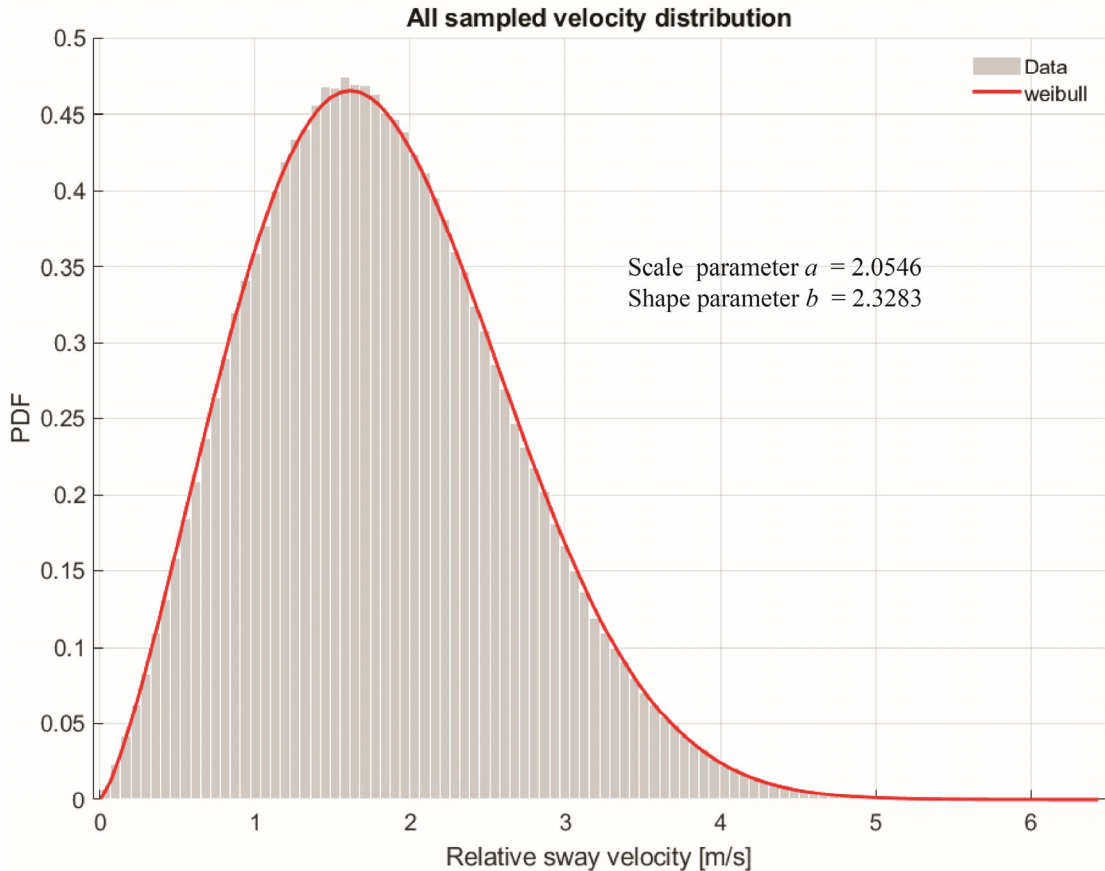


Figure 3.12: Statistical distribution of all sampled impact velocities in sway direction, unit: [m/s].

Table 3.2: All sampled sway velocity values in this study comparing to results from ST5 (Note, velocity values in this study contains an additional 0.79 m/s current velocity), unit: [m/s].

Non-exceedance level	50%	90%	99%	ST5 results	50%	90%
Weibull distribution	1.8	3.0	4.0	Rayleigh distribution of 3-hour maxima values	≈ 3.9	≈ 4.4

Given the sampled impact events in Figure 3.10, one separates the impact height range with several bins. The forthcoming analyses include 6 different bins, whose centre are listed in Table 3.3. Within each bin, a subset of impact velocities are available and the statistical analyses upon them were carried out. The best probabilistic fitting functions (see Table 3.4) together with the parameters within different bins are summarised in Table 3.3. The Weibull distribution gives the best fit for most of the bins, whereas the Nakagami and Generalized extreme value distribution fit best at the two ends of the height direction. One explanation to the inconsistent best-fit functions at the upper and lower end of the impact height direction could be that at these two ends (i.e., extremely high and extremely low impact locations), relatively smaller amount of simulated impact events are available to obtain the consistent Weibull distribution as appeared for other bins. Nevertheless, we content to what we obtained so far and impact

velocity analysis should be conducted with the derived best-fit functions with more weight giving to the consistent and conventional Weibull distribution.

Table 3.3: Sampled sway velocity values' statistic distribution within different bins at different impact height range (Note, velocity values in this study contain an additional 0.79 m/s current velocity), unit: [m/s].

Centre of bins [m]	Best fit distributions	Best fit parameters
-6.9825	Nakagami	$m = 1.0487 \quad \Omega = 1.5175$
-3.5175	Weibull	$\lambda = 1.5791 \quad k = 2.1874$
-0.0526	Weibull	$\lambda = 1.9127 \quad k = 2.3359$
3.4123	Weibull	$\lambda = 2.2696 \quad k = 2.5768$
6.8773	Weibull	$\lambda = 2.7021 \quad k = 2.8947$
10.3422	Generalized extreme value	$\mu = -0.3101 \quad \sigma = 0.8876 \quad \xi = 2.6074$

The probability distribution functions used together with their symbol definitions in Table 3.3 are summarised in the following Table 3.5.

Table 3.4: Probability distribution functions and symbols.

Weibull	$f(x) = \left(\frac{k}{\lambda}\right)\left(\frac{x}{\lambda}\right)^{k-1} \exp\left(-\left(\frac{x}{\lambda}\right)^k\right) \quad (x > 0)$
Nakagami	$f(x) = \frac{2m^m}{\Gamma(m)\Omega^m} x^{2m-1} \exp\left(-\frac{m}{\Omega}x^2\right) \quad (x > 0)$
Generalised extreme value	$f(x) = \frac{1}{\sigma} t(x)^{\xi+1} \exp(-t(x))$ $t(x) = \begin{cases} \left(1 + \xi\left(\frac{x-\mu}{\sigma}\right)\right)^{-1/\xi} & (\xi \neq 0) \\ \exp\left(-\left(\frac{x-\mu}{\sigma}\right)\right) & (\xi = 0) \end{cases}$

With the best-fit functions, we can derive the 50%, 90% and 99% non-exceedance relative sway velocities at different bins (at different height). This is visualised in Figure 3.13. To further put the calculated results into context, the same impact velocities' distribution together with its associated impact probability are plotted in Figure 3.14 with reference to the position and geometries of the structure. It is noticed that the impacts velocity is large at the high locations, but the probability of impact is small. As expected, the impacts reactions are skewed towards higher elevations.

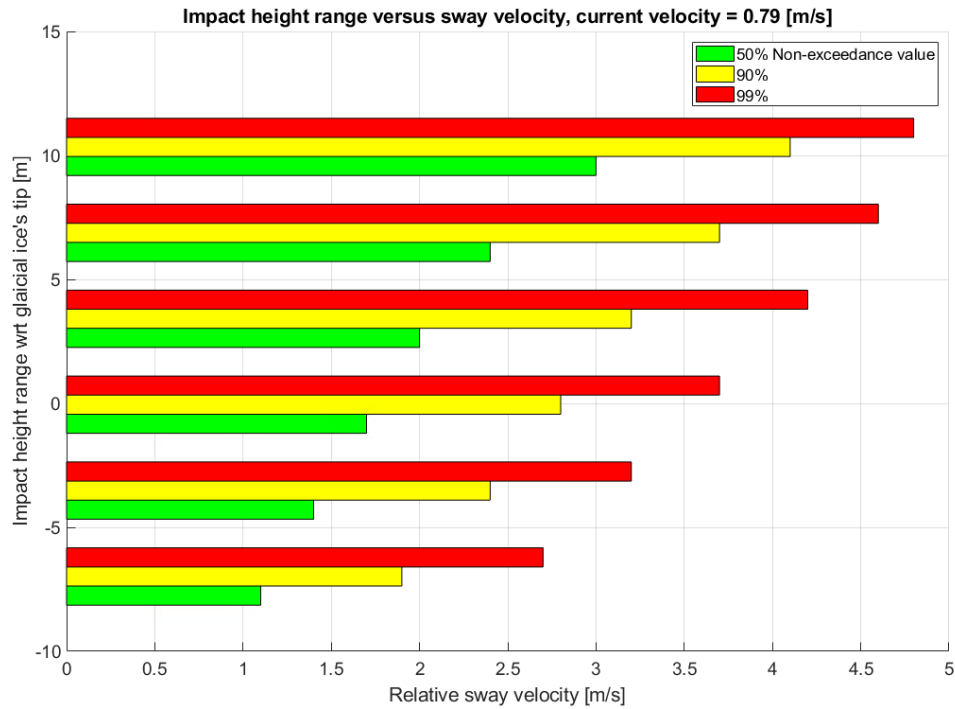


Figure 3.13: Impact velocities in sway direction at different heights with different non-exceedance levels.

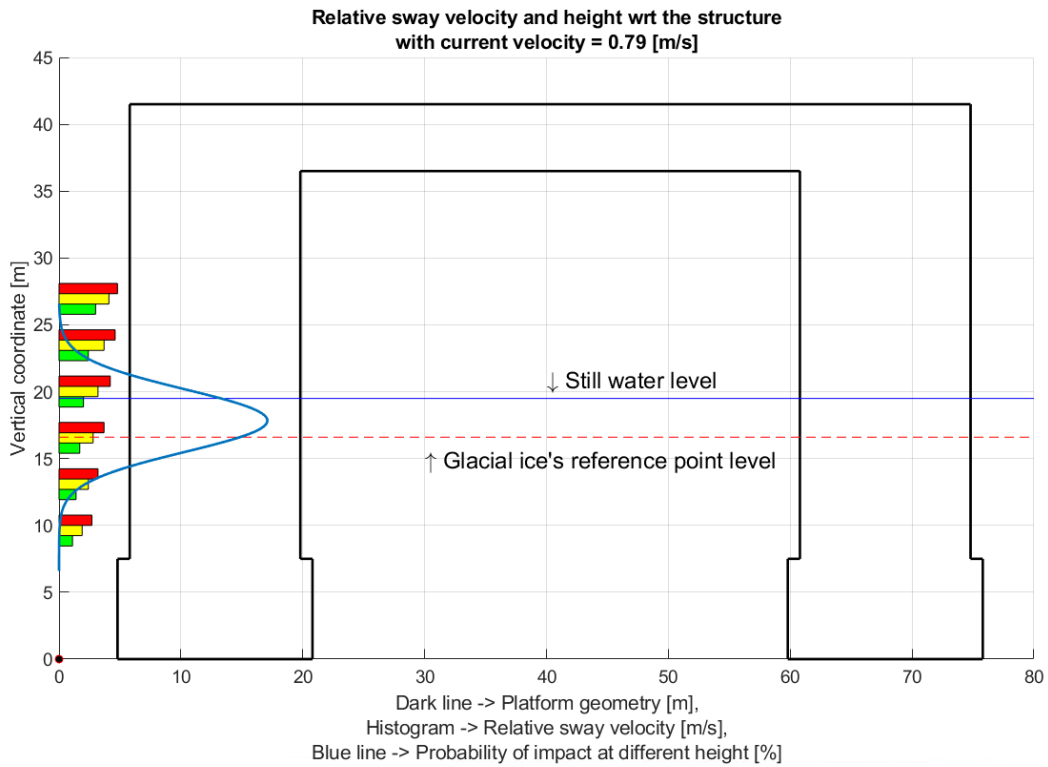


Figure 3.14: Impact velocities in sway direction and the associated impact probability at different heights with reference to the structure.

3.4.2 Impact in the vertical direction

Previous sections analysed the relative sway velocities' distribution collectively and at different heights. Such information is useful to characterise the horizontal impact. That was the major focus of this project. Additionally, however, it is also important to study the potential impacts, which may take place in the vertical direction. Particularly, when such a small ice feature travels into/in between the structure's columns and started to heave up and down, leading to potential impact with the pontoons. This scenario, i.e., impact in the vertical direction, is considered in this section.

Comparing to the horizontal direction impact scenario, the vertical direction impact differs when it comes to the sampling of impact events in the following aspects:

1. The advancement and hence current velocity has a minor influence on the velocity distribution and is neglected;
2. The impact is assumed to take place at the bottom of the ice feature onto the top of the pontoon. This naturally leads to the choice of using the bottom of the ice feature as one of the reference point and using the top of the pontoon as the other reference points;
3. The same set of equations from Eqs. (3.1) to (3.12) are utilised to calculate the relative motions between the above-defined two new reference points, except that $L^{pi} = 0$ in Eq. (3.4);
4. Impact only takes place/are only sampled when the ice feature is falling onto the top of the pontoons, i.e., when the relative heave displacement is changing from positive to 0 in the following figure (Note here we have already subtracted the clearance between the two reference points and a relative motion of 0 thus means impact occurs).

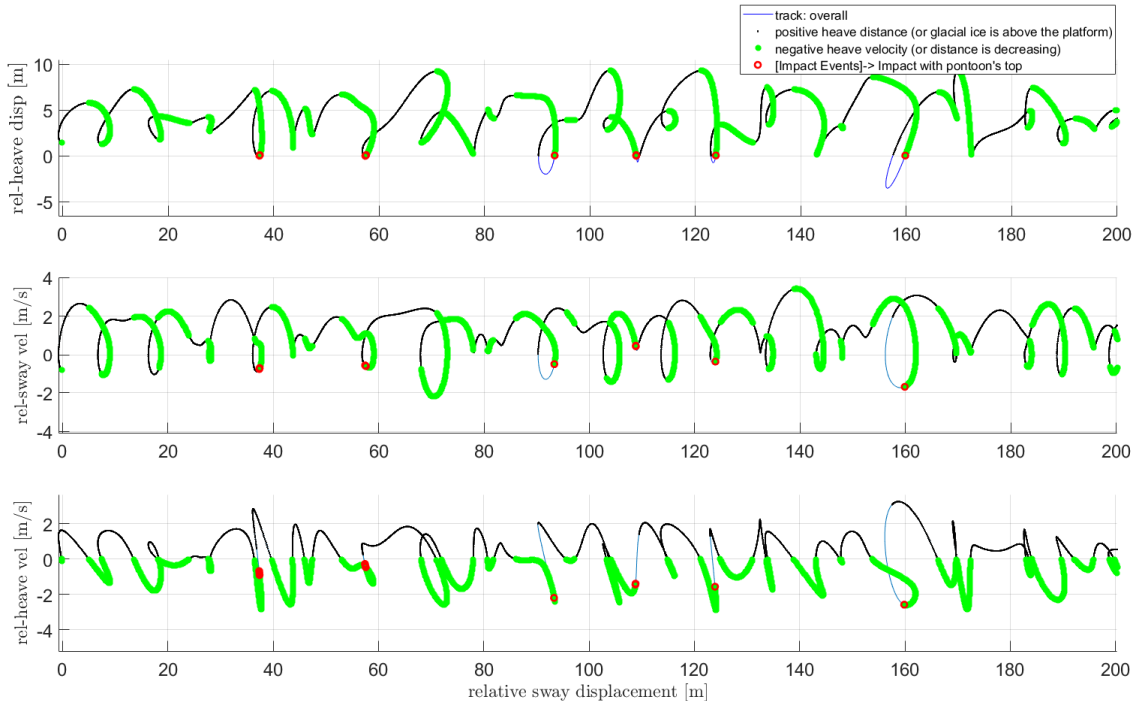


Figure 3.15: Illustration of the sampling of impact events in the vertical direction.

With the above defined impact events, Figure 3.15 shows the sampled vertical direction impact events with the pontoons (red circles) in a small time period as an example illustrating the sampling criteria's

influences. Collectively, we made 1000000 simulations regarding the relative heave motion between the reference points as red circles and its associated impact events as black dots in Figure 3.16.

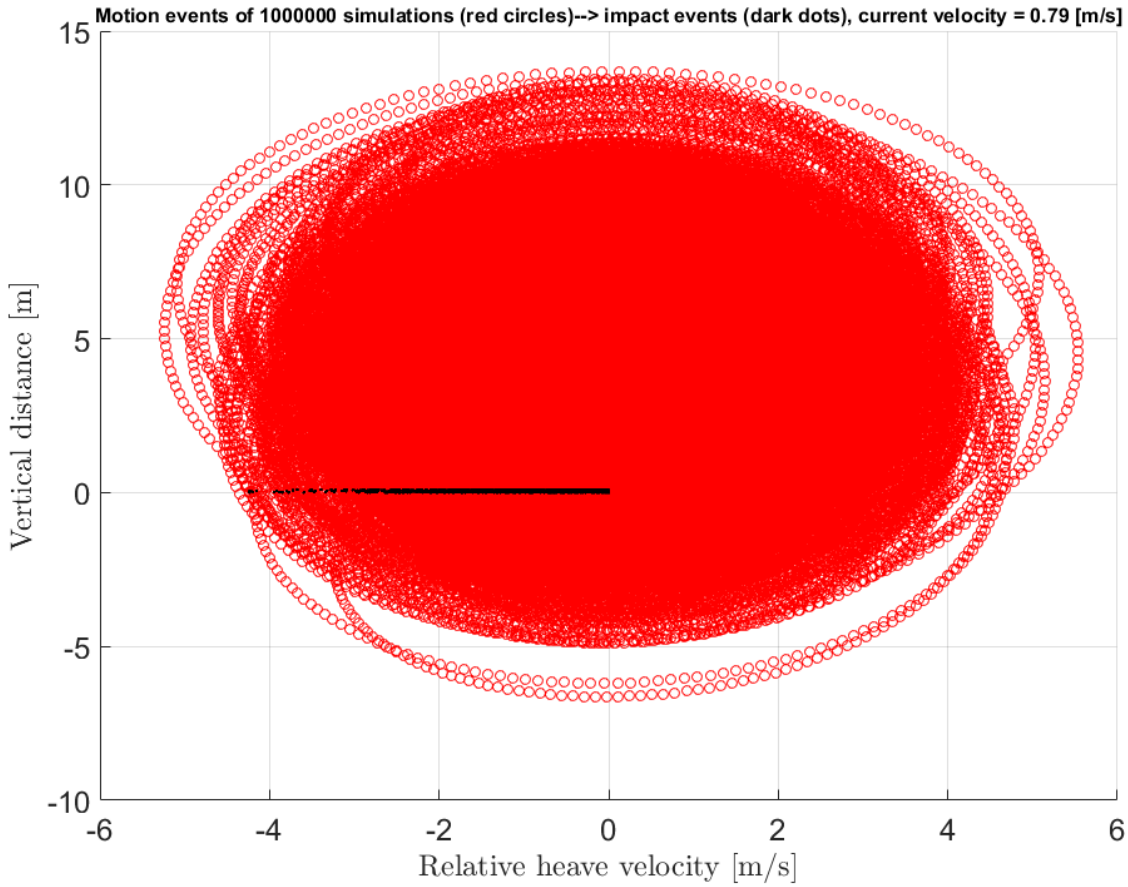


Figure 3.16: The sampling of impact events in the vertical direction among all conducted simulations.

Statistical analyses are further proceeded with the sampled impact events (i.e., dark circles). In principle, one can conduct analysis at different heights (same as that conducted for horizontal impact events). This might be useful if one is interested in other structural components (e.g., the horizontal member between two columns) that are also susceptible to vertical impact. For now, the focus is on the cases regarding vertical impact with pontoons.

The registered impact velocities in the vertical direction are processed and fitted in Figure 3.17 together with values of different non-exceedance levels in Table 3.5.

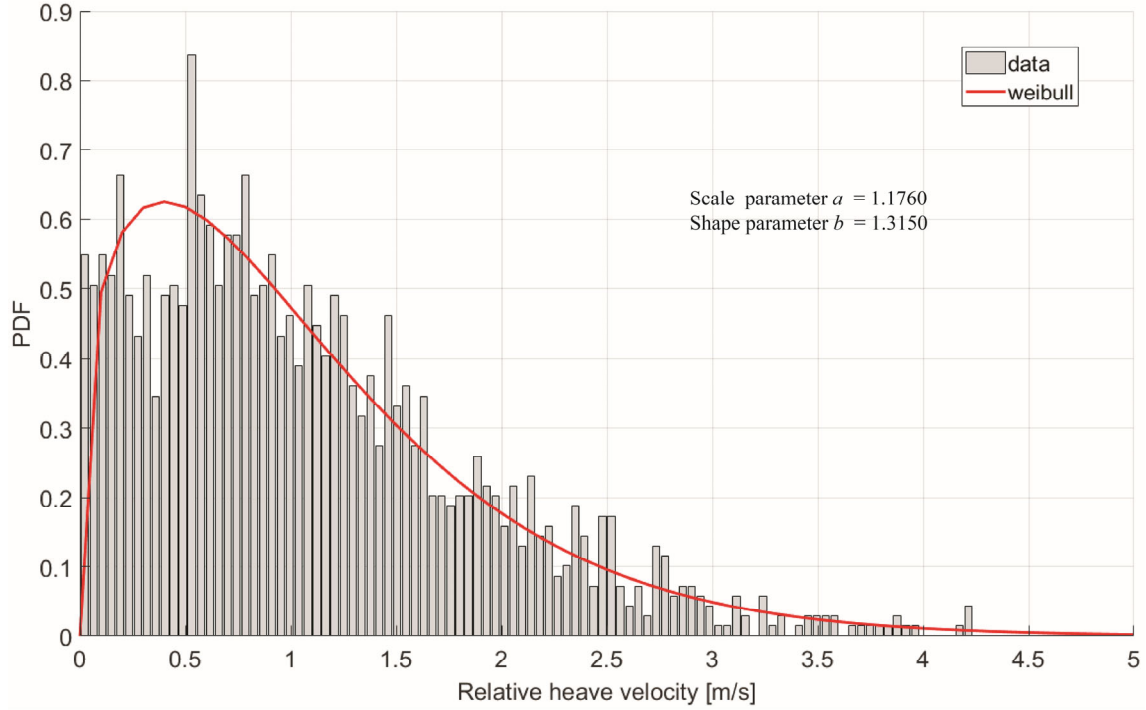


Figure 3.17: The sampled impact events' vertical velocities' distribution.

Table 3.5: all sampled vertical velocity values, unit: [m/s].

Non-exceedance level	50%	90%	99%
Weibull distribution	0.9	2.3	3.8

3.5 Summary

This chapter focuses on deriving the correlated impact velocities and heights. It is an extension of related work conducted in ST5. Based on the methods outlined in this chapter, we analysed two sets of impact events, i.e., the horizontal and vertical impacts. Focuses was placed on the horizontal impact scenario, as that was the basis for ST5. With new methods, we obtained the distribution of horizontal impact velocities in the height direction. This information (re-organised in Table 3.6) will be useful to scale SAMS' simulation results under the pre-defined test matrix.

Apart from supplying inputs to SAMS simulations, the following observations are made through the analysis conducted.

- For horizontal impacts, the impact velocities increase with the impact height (see Figure 3.13).
- The most probable horizontal impact with the ice tip occurs around the SWL (e.g., the maximum probability of impact in Figure 3.14).
- There is a rather low chance to have a horizontal impact either with the pontoon (12.5 m below SWL) or with anywhere say, 5 m above SWL (see Figure 3.14).
- For the pontoon, a horizontal impact is most likely not of concern for two reasons; 1) low chance of impact; 2) low horizontal velocity of impact (see Figure 3.14).

- However, it can very well be that the vertical impact is of concern for the pontoon. Figure 3.16 shows that quite substantial vertical impact velocities (see Table 3.5) may occur.

Table 3.6: Impact velocities and their associated impact probabilities at different queried height for SAMS simulations (Note, velocity values in this study are sampled under the influence of a 0.79 m/s current velocity).

Queried height [m]	Impact probability [100%]	Velocity 99% non-exceedance [m/s]	Velocity 90% non-exceedance [m/s]	Velocity 50% non-exceedance [m/s]
-10.8000	0.0000	0	0	0
-8.1000	0.0003	0	0	0
-5.4000	0.0114	2.9284	2.1284	1.2370
-2.7000	0.1219	3.3180	2.4944	1.4708
0	0.3854	3.7076	2.8061	1.7046
2.7000	0.3669	4.0972	3.1178	1.9383
5.4000	0.1051	4.4295	3.4868	2.2295
8.1000	0.0089	4.6706	3.8412	2.6117
10.8000	0.0002	0	0	0

4 Simulations of Impacts Using SAMS

The purpose of this chapter is to solve the external mechanics to determine the demand for energy dissipation, i.e. how much of the kinetic impact energy must be dissipated by deformation of the structure and/or the ice feature and how much that will remain as kinetic energy, possibly transferred to other rigid body motions. The demand for energy dissipation only specifies the total amount of deformation energy, not how this is distributed between the structure and the ice feature. This is determined by the “internal mechanics” described in Chapter 5.

We solve the external mechanics and calculate the demand for energy dissipation using the *Simulator for Arctic Marine Structures* (SAMS), a product of *Arctic Integrated Solutions* (ArcISo AS). The results from SAMS are verified with analytical solutions.

4.1 Description of SAMS

Until recently, time domain models of sufficient quality to perform numerical simulations of ice and marine structures interactions have not existed. Today, this has changed, partly through the efforts at the Norwegian University of Science and Technology (NTNU) hosting SAMCoT (Centre for Research-based Innovation - Sustainable Arctic Marine and Coastal Technology), laying the foundation of a versatile and accurate numerical simulator for fixed and floating structures in various ice conditions. As continuum-mechanics-based methods are not valid for representing realistic ice conditions in major parts of the Arctic, SAMCoT has placed a considerable emphasis on developing discrete element methods (DEM) that enable modelling the interactions between individual ice blocks (e.g., floe ice, level ice, ridges and icebergs) and the structure of interest (Lubbad et al., 2018).

The DEM can broadly be divided into two main categories: smooth discrete element modelling (SDEM) and non-smooth discrete element modelling (NDEM). The difference between the two can be seen as the difference between explicit and implicit time integration, allowing much larger simulation time steps, while maintaining stable simulations, when using NDEM. SAMS falls under the NDEM category, but it applies a novel implicit time stepping scheme and an improved contact model, enabling general visco-elastic contacts. SAMS distinguishes two types of contacts: the rigid contacts and the compliant contacts. The earlier does not adopt any upper-limit to the contact force resulting in computationally inexpensive contact model that can properly estimate the average contact force, but not the exact contact behaviour. This limitation makes rigid contacts inadequate if ice fracturing is to be encountered and thus they should only be used to model contacts between small ice fragments and the structure. Compliant contacts, on the other hand, are able to predict the exact contact behaviour. They consider the contact crushing force as well as the force-penetration gradient, leading to highly accurate contact force predictions, see Van den Berg et al. (2018). For this project (ST19), it is the compliant contact model that is utilised to simulate the contact between the ice feature and the structure; and the crushing process of the ice feature at the contact zone is characterised by such compliant model.

Aside from the novel contact model SAMS built upon (van den Berg et al., 2018), it is also worth mentioning other modules SAMS contains, such as the ice fracture module characterizing the fracture of (mainly) floe ice (Lu et al., 2015a, Lu et al., 2015b, Lu et al., 2016, Lubbad and Løset, 2011) and the hydrodynamic module (Tsarau et al., 2014, Tsarau, 2015) calculating multiple floating objects’ motion in waves, wind and currents. However, for this project (ST19), these two modules are not active given the nature and focuses of the engineering problem (i.e., impact between an ice feature and a semi-submersible structure).

4.2 Verification of SAMS simulations

We used an analytical solution to verify SAMS results. This solution is based on the assumption that the impact duration is small compared to the eigenperiod for the governing motion and that the forces are dominated by the impact force and inertia forces and hydrodynamic added mass forces. A complete solution for the external mechanics is presented by Liu and Amdahl (2019). The method is formulated for ship –ship impacts as illustrated in Figure 4.1, but is also relevant for semi-submersible structure – ice feature impacts.

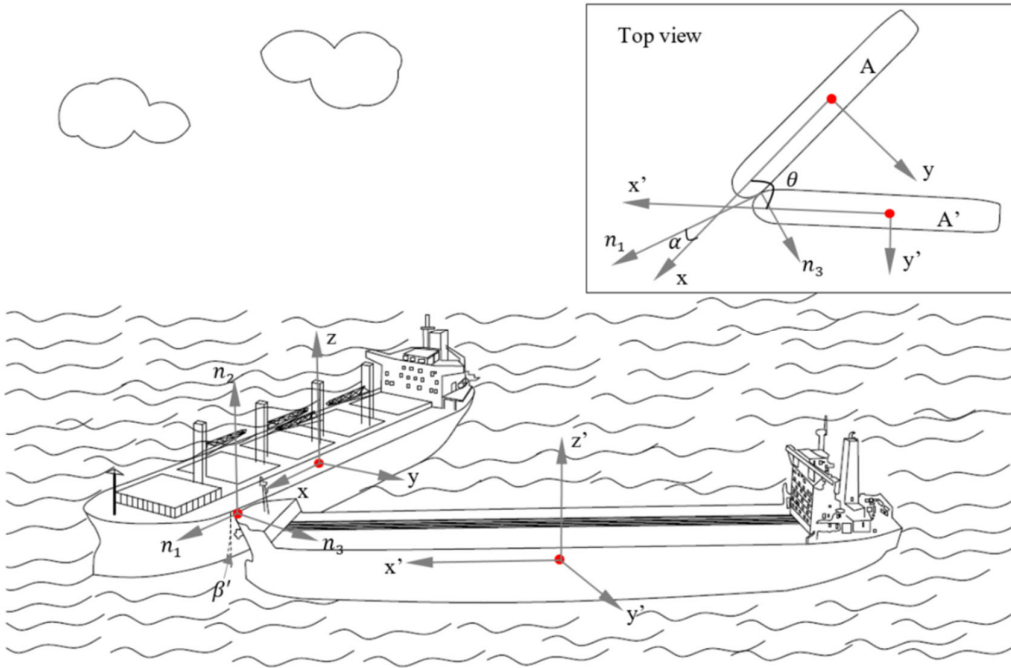


Figure 4.1: Illustration of external mechanics for ship impact (Liu and Amdahl, 2019).

The method is formulated by considering the equilibrium and conservation of momentum in the directions normal and parallel to the tangential impact plane (n_1, n_2, n_3 in Figure 4.1). The change of the relative velocities of the two bodies in the local coordinate system can be written as

$$d\bar{\mathbf{v}}_n = d\mathbf{v}_n - d\mathbf{v}'_n \neq \bar{\mathbf{K}}_n \cdot \mathbf{S}_n \quad (4.1)$$

where \mathbf{S}_n is the impulse vector and \mathbf{K}_n the so-called impact matrix defined by

$$\bar{\mathbf{K}}_n = \begin{bmatrix} \frac{C_{11}}{M} + \frac{C'_{11}}{M'} & \frac{C_{12}}{M} + \frac{C'_{12}}{M'} & \frac{C_{13}}{M} + \frac{C'_{13}}{M'} \\ \frac{C_{21}}{M} + \frac{C'_{21}}{M'} & \frac{C_{22}}{M} + \frac{C'_{22}}{M'} & \frac{C_{23}}{M} + \frac{C'_{23}}{M'} \\ \frac{C_{31}}{M} + \frac{C'_{31}}{M'} & \frac{C_{32}}{M} + \frac{C'_{32}}{M'} & \frac{C_{33}}{M} + \frac{C'_{33}}{M'} \end{bmatrix} \quad (4.2)$$

The coefficients are excessed as follows

$$C_{ij} = \frac{l_i l_j}{1 + a_1} + \frac{m_i m_j}{1 + a_2} + \frac{n_i n_j}{1 + a_3} + \frac{o_i o_j}{(1 + a_4) R_{xx}^2} + \frac{p_i p_j}{(1 + a_5) R_{yy}^2} + \frac{q_i q_j}{(1 + a_6) R_{zz}^2} \quad (4.3)$$

where l_i, n_i, m_i are the direction cosines of the impact plane relative to one body and o_i, p_i, q_i are the projection of the lever arms on the impact plane.

The energy can now be determined for two different cases, depending on whether the ice sticks to the structure or whether it slides along the side.

In order to determine the energy dissipation in three directions it is necessary to introduce the restitution coefficient and friction factors for the tangential force relative to the normal force μ_n , and the relative force for the two tangential components μ_t . For simplicity, the friction factors are calculated on the basis of the impulse ratios for S_1 , S_2 and S_3 , rather than the force ratios such that the following relationships are obtained

$$\begin{aligned} S_1 &= \frac{\mu_n}{\sqrt{1 + \mu_t^2}} S_3 = \mu_1 S_3 \\ S_2 &= \frac{\mu_n \mu_t}{\sqrt{1 + \mu_t^2}} S_3 = \mu_2 S_3 \end{aligned} \quad (4.4)$$

The restitution coefficient, e , gives the ratio of the normal velocity components after and before impact.

The energy can now be determined for two different cases, depending on whether the ice sticks to the structure or whether it slides along the side given a limiting friction factor of μ_0 .

In the stick case, where, $|\mu_n| < \mu_0$, the work done in the three directions are given by:

$$\begin{aligned} E_1 &= \frac{1}{2} \bar{M}_1 \left| (\bar{v}_1^t)^2 - (\bar{v}_1^0)^2 \right| = \frac{1}{2} \frac{\mu_1}{\mu_1 \bar{K}_{11} + \mu_2 \bar{K}_{12} + \bar{K}_{13}} (v_1^0 - v_1^{0'})^2 \\ E_2 &= \frac{1}{2} \bar{M}_2 \left| (\bar{v}_2^t)^2 - (\bar{v}_2^0)^2 \right| = \frac{1}{2} \frac{\mu_2}{\mu_1 \bar{K}_{21} + \mu_2 \bar{K}_{22} + \bar{K}_{23}} (v_2^0 - v_2^{0'})^2 \\ E_3 &= \frac{1}{2} \bar{M}_3 \left| (\bar{v}_3^t)^2 - (\bar{v}_3^0)^2 \right| = \frac{1}{2} \frac{1}{\mu_1 \bar{K}_{31} + \mu_2 \bar{K}_{32} + \bar{K}_{33}} (1 - e^2) (v_3^0 - v_3^{0'})^2 \end{aligned} \quad (4.5)$$

If we ignore the work done in the tangential direction, the work in the normal direction becomes

$$E_3 = \frac{1}{2} \frac{1}{\bar{K}_{33}} (1 - e^2) (v_3^0 - v_3^{0'})^2 \quad (4.6)$$

In the sliding case, $|\mu_n| > \mu_0$, the expressions for the work done in the three directions become

$$\begin{aligned}
E_1 &= \frac{1}{2} \bar{M}_1 |(\bar{v}_1^t)^2 - (\bar{v}_1^0)^2| = \frac{1}{2} \frac{\mu_1}{\mu_1 \bar{K}_{11} + \mu_2 \bar{K}_{12} + \bar{K}_{13}} |(2\bar{v}_1^0 + d\bar{v}_1) d\bar{v}_1| \\
E_2 &= \frac{1}{2} \bar{M}_2 |(\bar{v}_2^t)^2 - (\bar{v}_2^0)^2| = \frac{1}{2} \frac{\mu_2}{\mu_1 \bar{K}_{21} + \mu_2 \bar{K}_{22} + \bar{K}_{23}} |(2\bar{v}_2^0 + d\bar{v}_2) d\bar{v}_2| \\
E_3 &= \frac{1}{2} \bar{M}_3 |(\bar{v}_3^t)^2 - (\bar{v}_3^0)^2| = \frac{1}{2} \frac{1}{\mu_1 \bar{K}_{31} + \mu_2 \bar{K}_{32} + \bar{K}_{33}} (v_3^0 - v_3^{0'})^2
\end{aligned} \tag{4.7}$$

where the relative velocity changes on the tangential plane are given by

$$\begin{aligned}
d\bar{v}_1 &= -\frac{\mu_1 \bar{K}_{11} + \mu_2 \bar{K}_{12} + \bar{K}_{13}}{\mu_1 \bar{K}_{31} + \mu_2 \bar{K}_{32} + \bar{K}_{33}} (v_3^0 - v_3^{0'}) \\
d\bar{v}_2 &= -\frac{\mu_1 \bar{K}_{21} + \mu_2 \bar{K}_{22} + \bar{K}_{23}}{\mu_1 \bar{K}_{31} + \mu_2 \bar{K}_{32} + \bar{K}_{33}} (v_3^0 - v_3^{0'})
\end{aligned} \tag{4.8}$$

Given the above analytical formulations of the external mechanics (initially used for ship-ship impact analysis), the present study sets up two case studies to benchmark SAMS' simulation results to that of analytical external mechanics (Liu and Amdahl, 2019).

Figure 4.2 illustrates the set-up of two case studies, i.e., a head-on and an inclined impact of the spheroidal ice feature with the structure. In order to be in accordance with the assumptions made in the analytical approach, the following adjustments have to be made within SAMS:

- The two bodies that are in contact are infinitely rigid (i.e., the rigid contact model in SAMS is activated);
- There is no restitution after the contact (the restitution coefficient in SAMS' rigid contact model is set to 0).

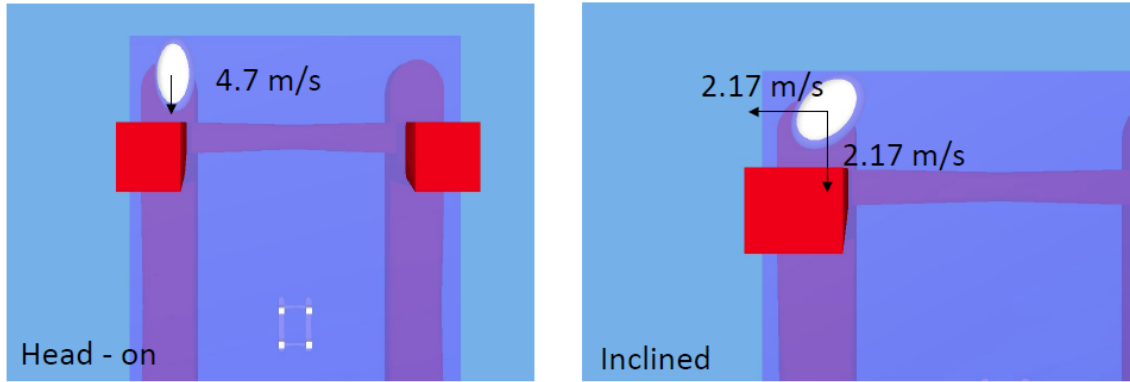


Figure 4.2: Two case studies to cross validate SAMS simulation results and analytical external mechanics by (Liu and Amdahl, 2019).

With the previously introduced assumptions and test setups. The following comparison results are obtained in Table 4.1.

Table 4.1: Benchmark test results.

	Head on impact		Inclined impact	
	Impact Energy	Difference	Impact Energy	Difference
Analytical approach	12.770 [MJ]		2.73 [MJ]	
SAMS	12.766 [MJ]	0.025%	2.73 [MJ]	0.000024%

The favourable comparisons in Table 4.1 are encouraging and signify the correctness of SAMS simulations. Some assumptions were made in this benchmark test, but SAMS simulation's capabilities are not limited by these assumptions. More general contact scenarios can be simulated by SAMS, e.g. the crushing process of ice feature using the compliant contact model of SAMS. The rigid contact model of SAMS was benchmarked in this section, but the two contact models of SAMS are using the same building blocks, e.g. the same time-stepping and integration scheme. Hence, it is concluded that this benchmark test demonstrates the capability and correctness of SAMS' simulations.

4.3 Energy map

After the successful benchmark tests conducted in the previous section, SAMS is used to analyse the statistical distribution of impact energy and peak impact force as a function of the impact position and direction. A total of 1800 different impact scenarios are simulated using a spheroidal ice feature geometry in open water. Further, 90 simulations are performed using ice feature shapes digitized from measurements. The simulations with ice feature shapes digitized from measurements are performed with the presence of ambient ice. The main results of the SAMS simulations are:

- Impact load patch, pressure, and total load, as a function of time, for each impact scenario.
- Impact energy, as a function of time, for each impact scenario.

The impact energy is defined as the kinetic energy that is dissipated during ice feature - structure impact. Energy dissipation occurs both in the structure as well as in the ice feature; the ice feature may dissipate energy by crushing of the ice at the contact zone. The structure may dissipate energy by plastic deformation of the structure hull. In the SAMS simulations, the structure is assumed to be rigid, thus all energy dissipation occurs by crushing of the ice. A more detailed analysis of impact energy dissipation mechanism is provided in Section 5.4. All simulations are initiated with the same initial ice feature's drifting velocity. The simulation results are scaled to other velocity values in post-processing.

Using the simulation results, the impact probability as well as the distribution of impact energy is visualized in energy maps and cumulative distribution functions for the impact energy and the maximum load. Note that the results presented in this section are dependent on the used ice feature geometry, the semi-submersible structure geometry and the design sea state. Therefore the analyses performed in this section should be seen as a template for how an ice feature impact analysis may be performed, rather than being directly applicable to other structures, ice feature geometries and sea states.

Firstly the simulation input values are discussed. Thereafter the study discusses the scaling that is applied to the SAMS results, after which the main results of the performed time domain analyses are presented.

4.3.1 Simulation input values

The simulations are performed using the structure and the ice feature described in Figure 2.11. Other simulation parameters are:

Ice-structure friction coefficient:	0.15
Structure Radius of gyration (x,y,z) ¹ :	[36, 34, 42] m
Ice feature's density ² :	900 kg/m ³
Crushing Specific Energy (CSE) ice feature ^{3,4} :	3.0 MN/m ³
Initial ice feature's velocity ⁴ :	4.0 m/s
Added mass ice feature (70% of mass):	535.5 tons
Added mass matrix structure (distribution instead of structure) (kg/kgm ²) ⁵ :	

$$\begin{bmatrix} 7.998 \cdot 10^6 & 0 & 0 & 0 & -8.087 \cdot 10^7 & 0 \\ 0 & 2.351 \cdot 10^7 & 0 & 4.105 \cdot 10^8 & 0 & 0 \\ 0 & 0 & 3.568 \cdot 10^7 & 0 & 0 & 0 \\ 0 & 4.105 \cdot 10^8 & 0 & 4.313 \cdot 10^{10} & 0 & 0 \\ -8.087 \cdot 10^7 & 0 & 0 & 0 & 2.820 \cdot 10^{10} & 0 \\ 0 & 0 & 0 & 0 & 0 & 2.705 \cdot 10^{10} \end{bmatrix}$$

1: Values as received from ST20.

2: Value as used in ST5.

3: The energy absorbed in the crushing of ice.

4: Simulation results are scaled to different values of CSE parameter.

5: Values as received from ST20, using the infinite frequency added mass.

Since the impacts between the structure and the ice feature are of short duration, hydrodynamic damping is neglected.

4.3.2 Scaling of the simulation results

All simulations are performed with the same initial velocity. The simulation results can be scaled in post-processing to represent impacts at other velocities. In addition, the simulation results may be scaled to other values for added mass and CSE. Due to the nonlinear nature of the simulations, the scaled results may have a small deviation compared to the equivalent unscaled results. The accuracy of result scaling is investigated for 21 different scenarios. The analysis shows that the scaled results on average deviate 1.5% from the unscaled results. This is considered sufficiently accurate, given the substantial uncertainty in other aspects of the performed analyses. As an example, an assessment of the scaling accuracy of contact energy as a function of velocity is presented in Figure 4.3. Scaling of the load and energy respectively is applied as follows:

Energy: \sim added mass¹

\sim velocity²

\sim CSE⁰

Peak load: \sim added mass^{0.5}

\sim velocity

\sim CSE^{0.5}

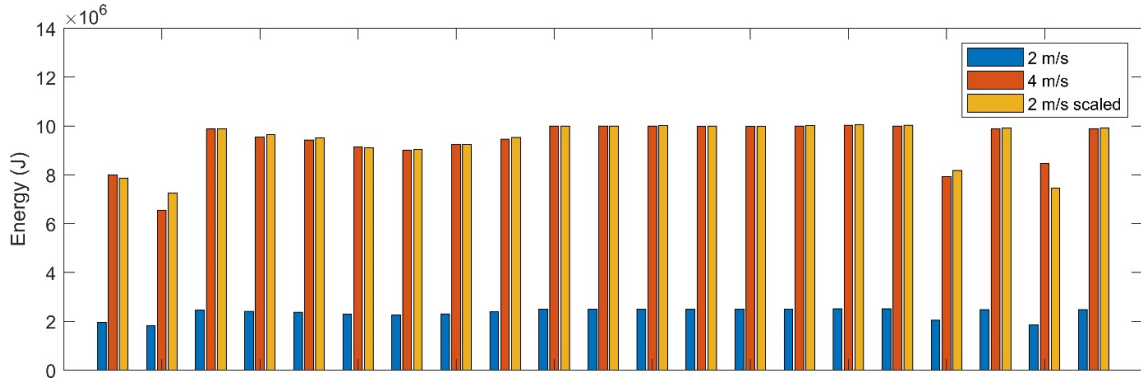


Figure 4.3: Scaling accuracy of energy versus velocity for 21 simulations. Mean difference: 1.5%.

4.3.3 Simulation output

From each simulation, the following output is generated:

- Position, orientation, linear and rotational velocity of the structure and ice feature, as a function of time.
- Contact load (both normal and frictional load), as a function of time.
- The loading patch, as a function of time.
- The kinetic energy of the ice feature and the structure, as a function of time.
- The dissipated contact energy, as a function of time.

The time-domain result of one scenario is shown as an example. The initial position, velocity and drift direction of the ice feature in this scenario are:

Initial position: [-84.1, 11.7] m (origin at COG of the semi-submersible structure)

Drift direction: 20°, see Figure 4.4.

Drift velocity: 2.32 m/s

Vertical offset: 0 m (both the ice feature and the structure are in hydrostatic buoyancy position in no-wave conditions)

The initial position and direction of the ice feature, as well as the ice feature's position at the moment of impact, are visualized in Figure 4.4.

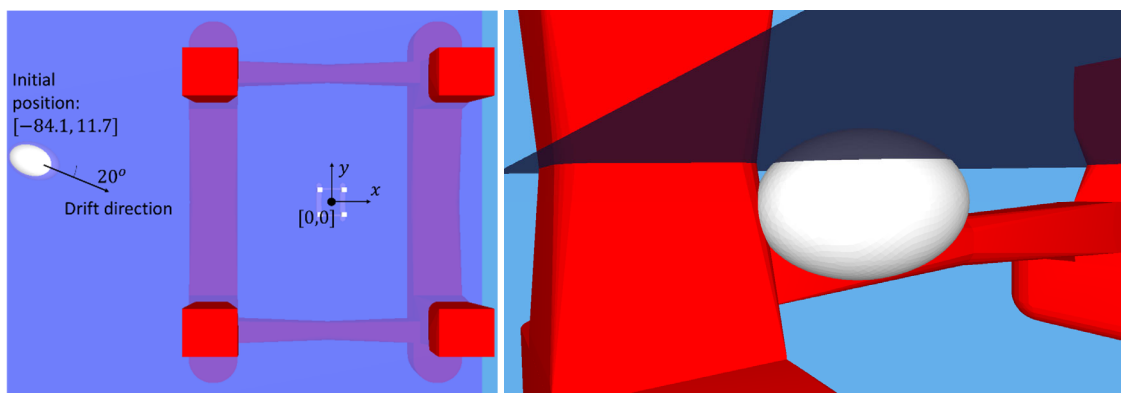


Figure 4.4: Initial position and direction (left). Ice feature's impact (right)

Figure 4.5 displays the load patch on the structure geometry at the moment of maximum load, as well as the contact pressure as a function of time. The load patch size and impact duration are scaled according to scaling laws presented in Section 4.3.2.

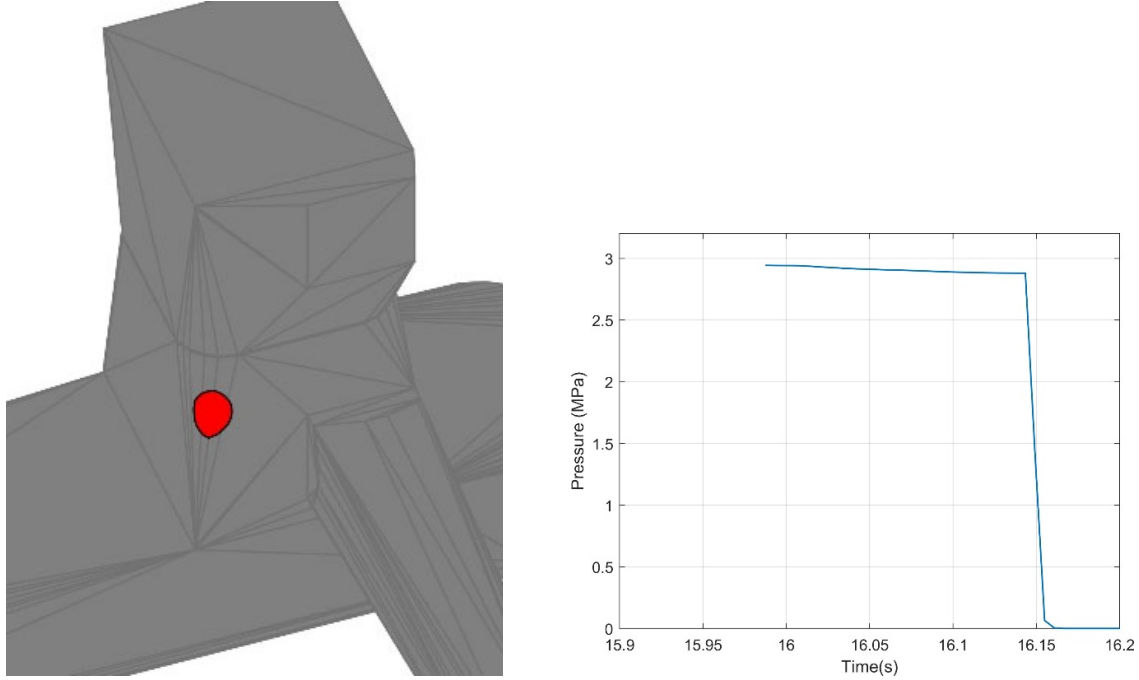


Figure 4.5: Maximum load patch on structure (left). Contact pressure as a function of time (right).

The normal load and the energy dissipation as a function of time are shown in Figure 4.6. Both load and energy are scaled according to the scaling laws presented in Section 4.3.2.

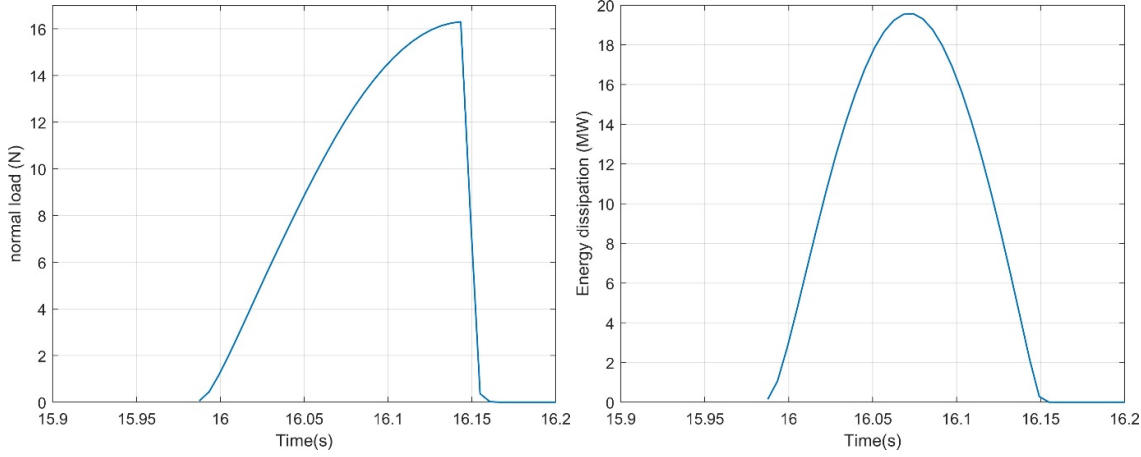


Figure 4.6: Normal load (left) and Energy dissipation (right) as a function of time.

In the remainder of this chapter, the study no longer uses the time-domain results of each simulation. Instead, the total dissipated energy, the maximum load and the load patch at the moment of maximum load are used to compare and combine the results of the different impact scenarios.

4.3.4 Test matrix: spheroidal ice feature in open water

A total of 1800 different impact scenarios is simulated using the spheroidal ice feature in open water. The ice feature's vertical offset, horizontal offset and drift direction are systematically varied in order to obtain the impact energy and loading values for a wide range of geometric impact scenarios. The impact height, direction and position are varied according to the test matrix shown in Table 4.2.

Table 4.2: Test matrix of spheroidal ice feature in open water.

Ice feature	Range	Number of values
Vertical offset	-10.8 to 10.8 ¹⁾	9
Horizontal offset	-67.5 to 67.5	20
Drift direction	0° to 90°	10

¹⁾ Variation from the hydrostatic buoyancy position of the ice feature and the semi-submersible structure in no-wave conditions (i.e., at SWL).

The different impact conditions are visualized in Figure 4.7 and Figure 4.8. The offset width is chosen to cover the diameter of the circle enclosing the structure in top-view. The impact directions vary from 0° ~ 90°, since the structure is symmetrical and the results can be mirrored. The impact height range goes from the minimum to the maximum impact height that was found for the 100-year wave condition in ST5. In total, 1800 simulations were performed covering a wide range of geometrical impact scenarios.

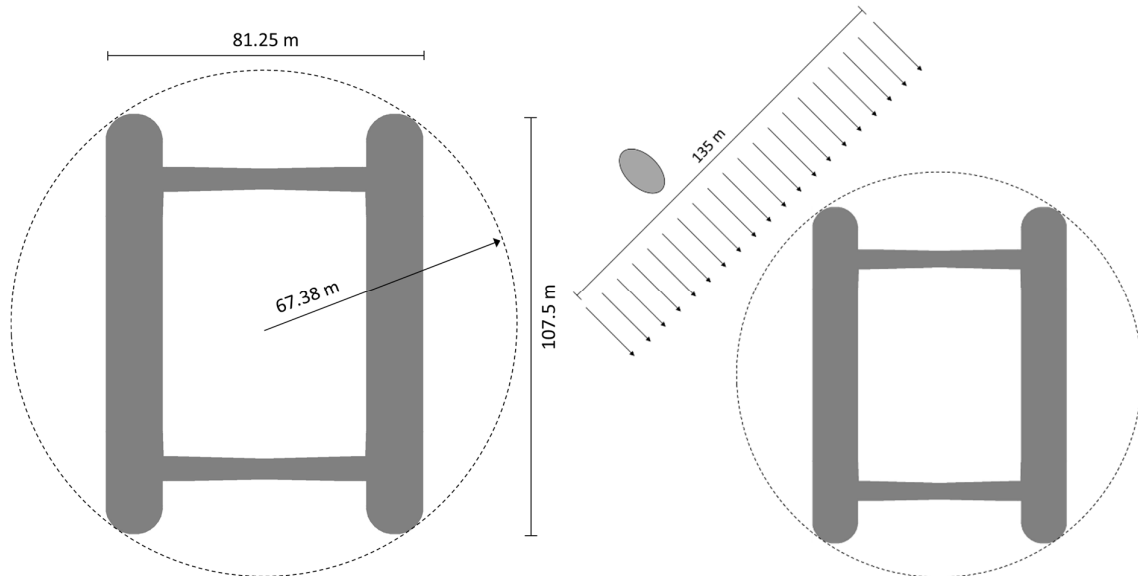


Figure 4.7: Top view of the semi-submersible structure, showing main structure dimensions and the radius of the minimum bounding circle (left). Ice feature horizontal offset as applied for each impact direction and impact height (right).

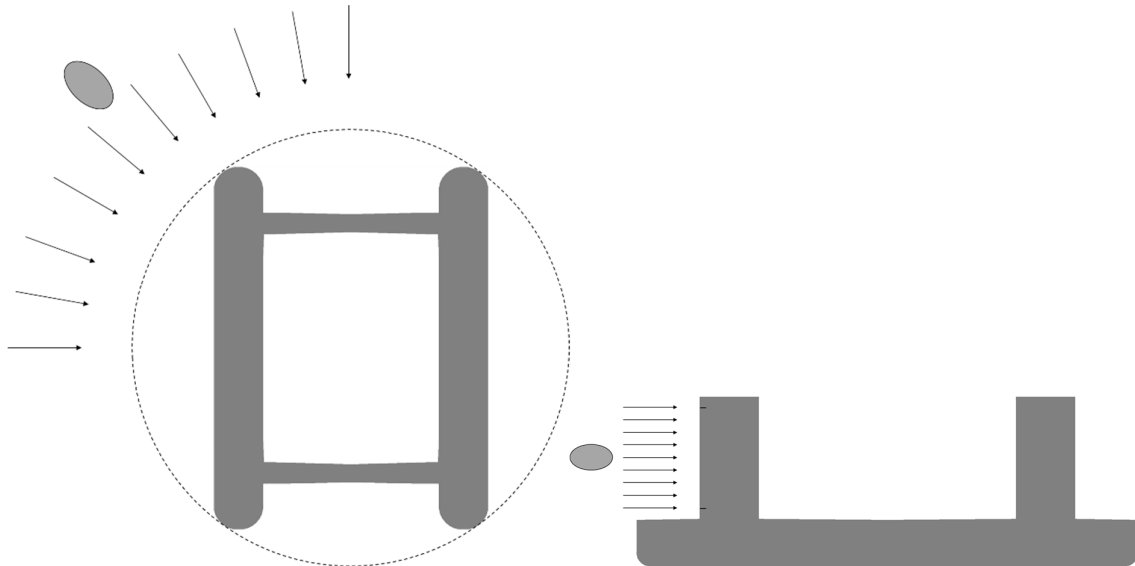


Figure 4.8: Simulated drift directions (left) and vertical offsets (right).

4.3.5 Simulation results

From the 1800 scenarios in the presented test matrix, the ice feature managed to collide with the structure in 1278 cases. Since the ice feature's drift direction, horizontal offset and vertical offset were varied with equal-spaced intervals, there are scenarios in which the ice feature did not contact the structure. The ice feature trajectories from all simulations are displayed in Figure 4.9. The ice feature trajectories show that it is likely that ice features may enter the area between the structure legs.

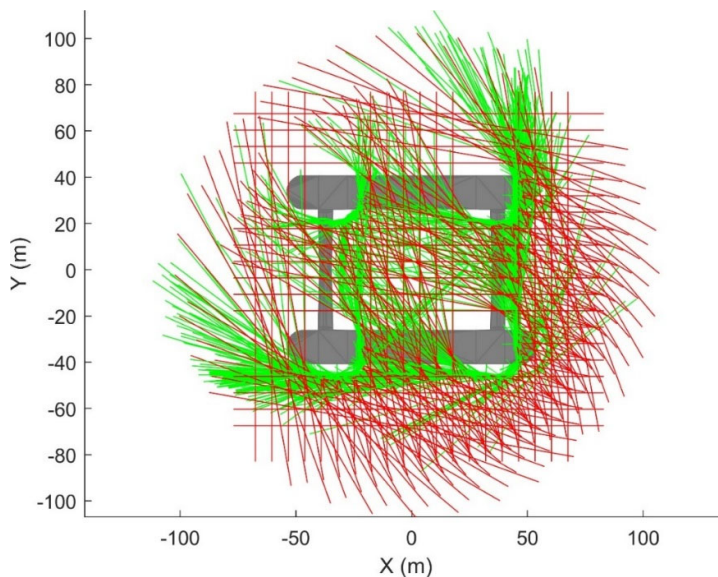


Figure 4.9: Ice feature's trajectories, top view, drift direction variation from 0 to 90°. Red lines: path before impact. Green lines: path after impact.

For each impact, the total dissipated impact energy, the peak load, and the maximum loading patch is extracted from the time-domain results, in order to present an impact energy map on the structure's hull. The energy map of the unscaled simulation results is shown in Figure 4.10.

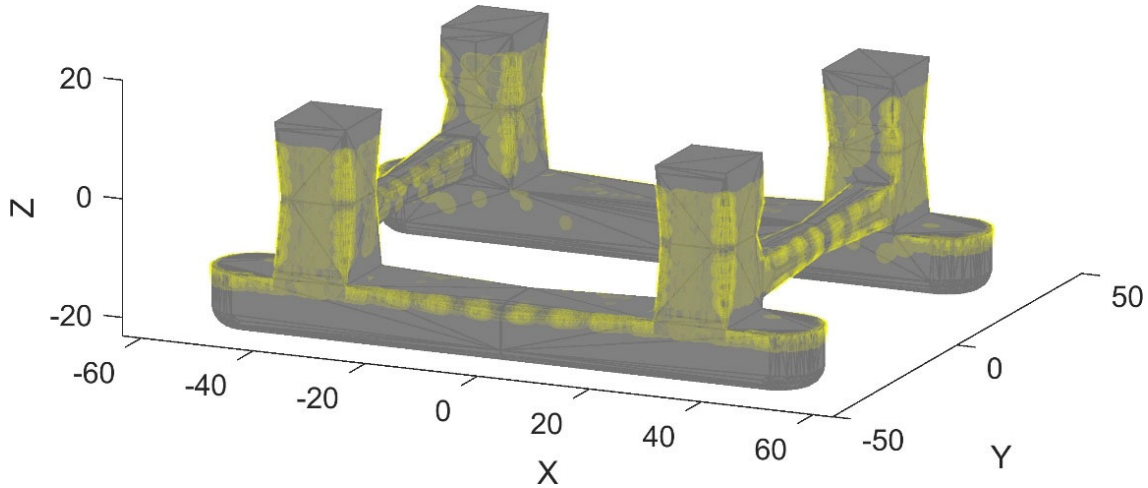


Figure 4.10: Unscaled energy map of impacts. Load patches show the maximum contact area from each simulation. The brightness of the patch in yellow reflects the amount of dissipated energy.

The unscaled energy map is produced assuming a uniform probability distribution of impact height and a constant ice feature drift velocity of 4 m/s. However, this is not representative for real conditions; following from the results of Chapter 3, the impact probability as a function of height is normally distributed, and the impact velocity distribution is correlated with the impact height. Figure 4.11 shows the energy map taking the impact probability as a function of height into account.

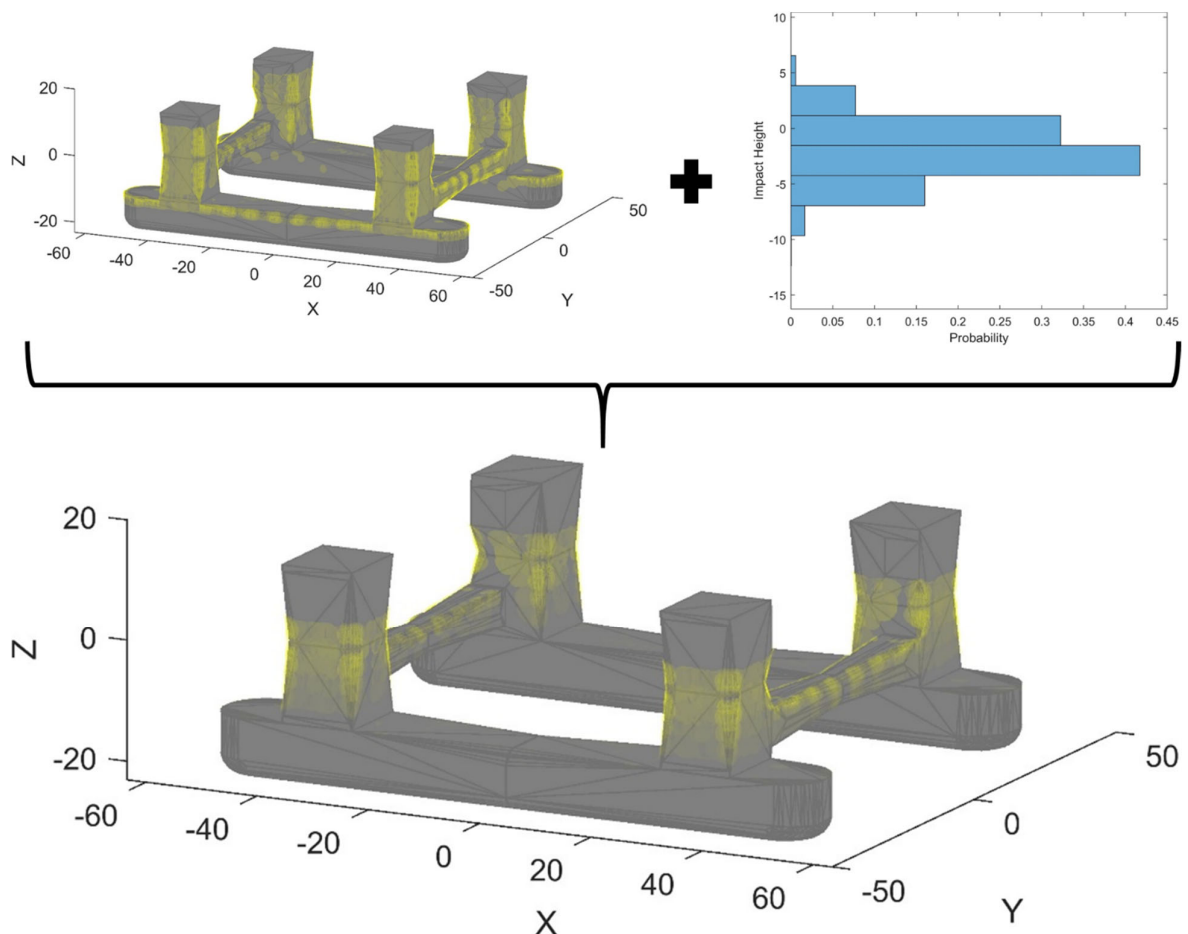


Figure 4.11: Impact energy map, scaled with the impact probability versus height.

In addition to the impact probability, the impact velocity distribution is also non-uniform as a function of height. Scaling the results according to the 90% non-exceedance impact velocities at each impact height, as obtained in Chapter 3, leads to the energy map shown in Figure 4.12.

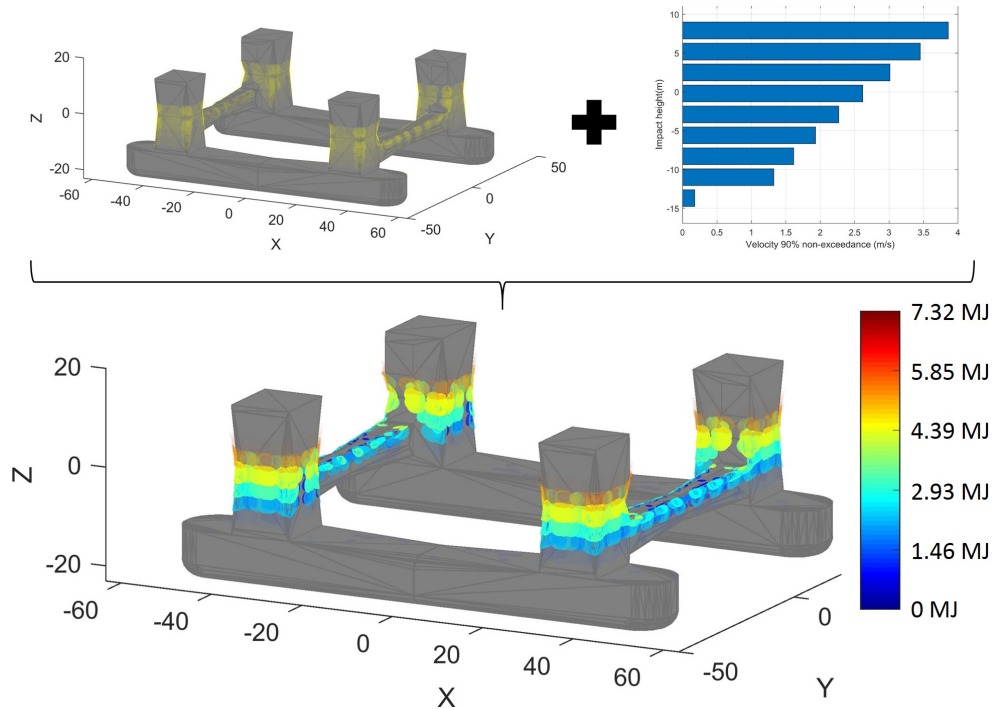


Figure 4.12: Impact energy map, scaled with the 90% impact velocity versus height.

The scaled energy map shows that the structure legs and the horizontal members are most susceptible to ice feature impacts. The simulations show that the impacts with the highest impact energy occur on the structure legs. The impacts on the horizontal members result in lower energy dissipation, since the hull geometry is inclined at the location of impact. To further assess the impact probability on different structural members, the structure is divided into 4 regions:

- Legs
- Horizontal members
- Mid-sections of pontoons
- End-sections of pontoons

For each region, the impact probability is assessed based on the simulation results. The regions are visualized in Figure 4.13.

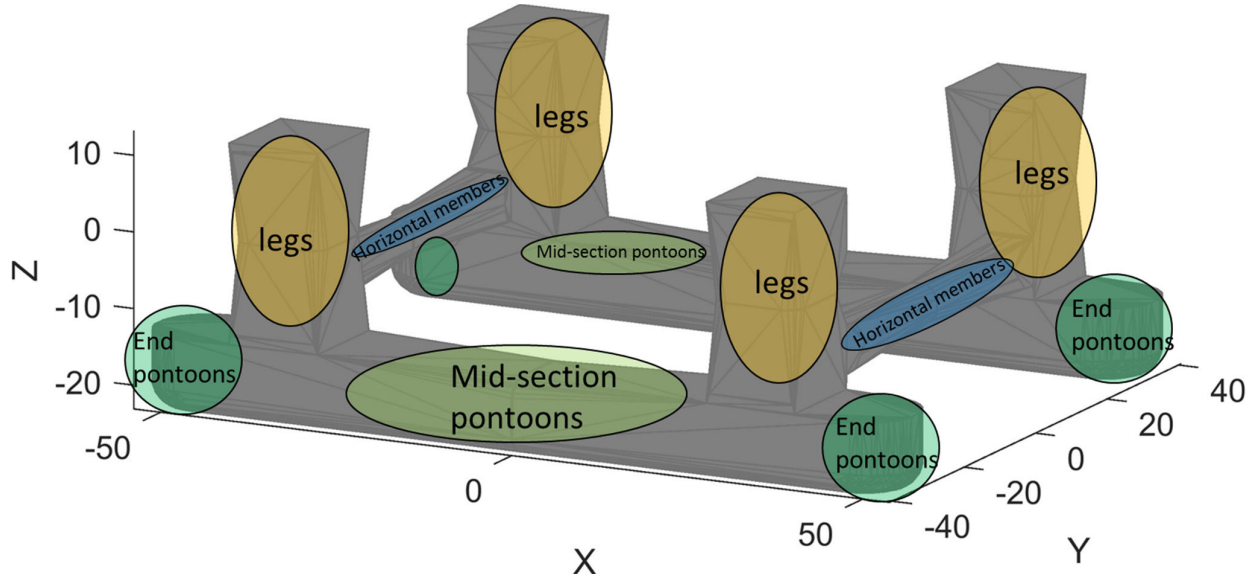


Figure 4.13: Sections of the semi-submersible structure for which impact probability is analysed.

Using the SAMS simulation results and the impact probability as a function of height as obtained from Chapter 3, the impact probability on the different structural sections are:

Table 4.3: The impact probability on the different structural sections.

Section	Impact probability (% of all impacts)
Legs	68.8
Horizontal members	30.6
Mid-section pontoons	0.3
End-section pontoons	0.3

The simulation results show that pontoon impacts have a low probability when the analysed semi-submersible structure is at its operating draft. Note that these results depend heavily on the assumed ice feature and semi-submersible structure geometry and on the design sea state used.

Cumulative density functions (CDFs) of the scaled impact energy and peak load are shown in Figure 4.14. The CDFs show that there is a large variety in the impact energy and peak load resulting from the simulations. Specifically, the high-energy impacts have a low probability of occurrence. This is caused by the correlation between impact height and velocity. The impacts with the highest velocity have a low probability of occurrence. From the 1278 simulations in which the ice feature collided with the structure, three scenarios are identified for more detailed analysis using NLFEM modelling. The impact energy and maximum load as resulting from the SAMS simulations of the three identified scenarios are highlighted in Figure 4.14.

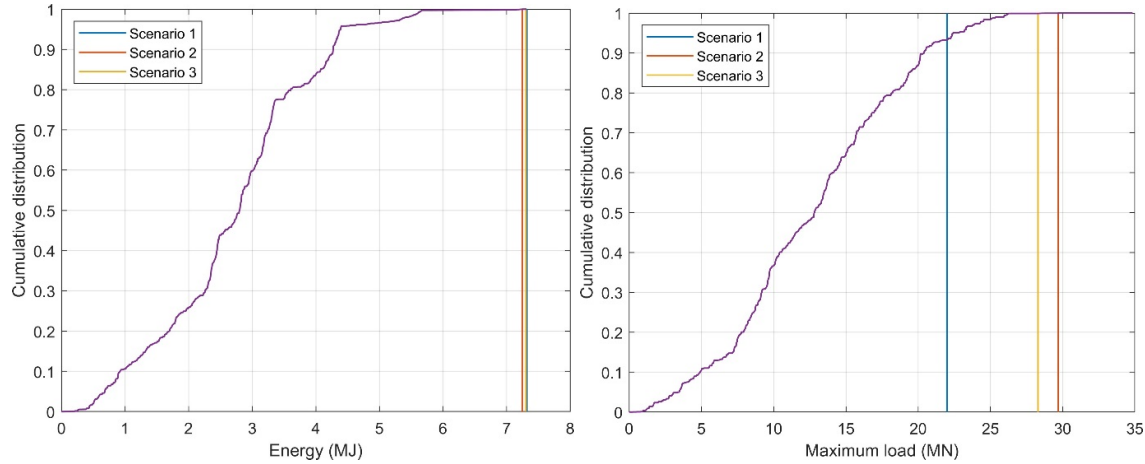


Figure 4.14: Cumulative distribution of impact energy and maximum load, of the scaled simulation results. Identified critical scenarios are highlighted.

4.3.6 Critical impact scenarios

The three identified critical scenarios are chosen based on their high impact energy and/or the high maximum load. In addition, the impact location on the structure is taken into account. The impact conditions of the identified scenarios are visualized in Figure 4.15. Some key properties of the critical impact scenarios are listed in Table 4.4.

Table 4.4: Key properties of critical impact scenarios.

Scenario	Ice feature drift velocity (m/s)	Maximum load ¹ (MN)	Impact energy (MJ)	Impact location
1	3.4	22.0	7.32	Corner of structure leg
2	3.4	29.7	7.25	Side of leg
3	3.4	28.3	7.30	Side of leg, near corner

¹⁾ Assuming a rigid structure. The NLFEM simulations for these scenarios will result in different loads, since the structure is non-rigid.

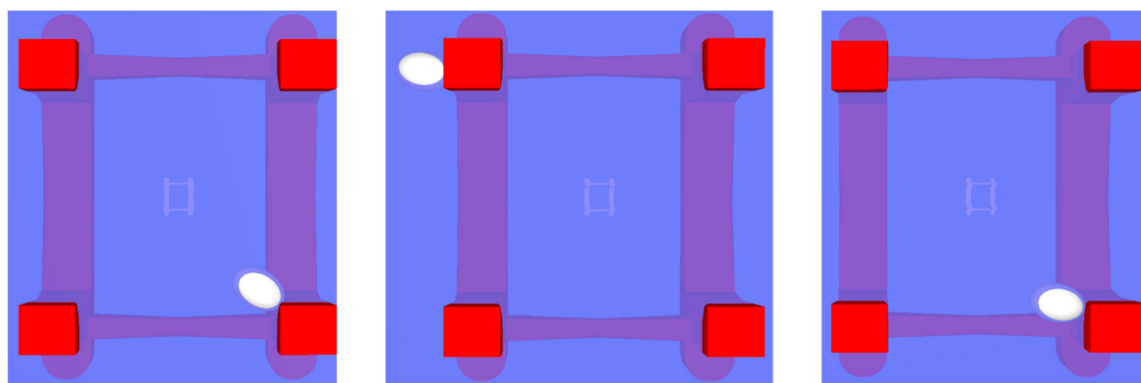


Figure 4.15: Critical impact Scenarios 1, 2 and 3.

The critical impact scenarios are analysed in more detail using NLFEM modelling in Chapter 5. Impacts on the horizontal members are not selected as critical scenarios for the following reasons:

- The lower impact energy and maximum load of the impacts on horizontal members.

- The fact that these members are specific to this structure geometry, and the results of a more detailed analysis of horizontal member impact may not be useful in a more general scenario.
- The fact that structural drawings and/or a FEM model of the horizontal members are not available to the authors.

4.3.7 Simulations with ambient floe ice and other ice feature shapes

For curiosity reasons and not directly relevant to the current study, simulations with ambient floe ice and other ice feature shapes were performed in order to assess if this will result in loading conditions different or more severe than the conditions resulting from impact with spheroidal ice feature in open water. Several mechanisms may lead to more severe loading conditions:

- Secondary loading from ambient floe ice on the ice feature.
- Different ice feature geometry, resulting in differences in impact load and energy dissipation.

Two different ice feature geometries were used. The main parameters of the digitised ice features geometries are shown in Table 4.5. Figure 4.16 shows the digitized iceberg geometries as visualized in SAMS.

Table 4.5: Mass properties of the digitized ice feature geometries.

Ice Feature #1		Ice Feature #2	
Mass (tons):	2173	Mass (tons):	966
Added mass ¹⁾ (tons):	1521	Added mass ¹⁾ (tons):	676
Density (kg/m ³):	900	Density (kg/m ³):	900

¹⁾ Assumed 70% of mass.

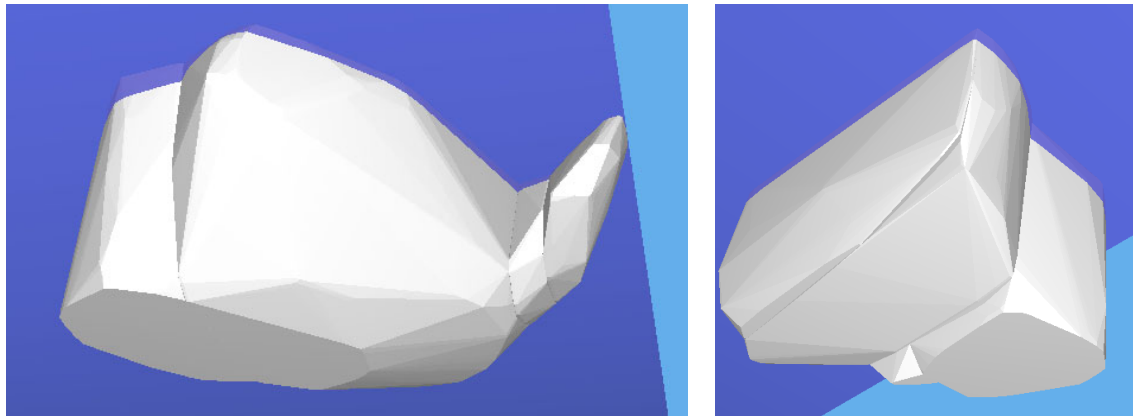


Figure 4.16: Digitized ice feature geometries. Ice Feature #1 (left) and Ice Feature #2 (right).

The ambient ice conditions used are described in Section 2.1.3.1. The ambient ice concentration is sufficient to prevent major waves from occurring. Therefore only the design current as specified in Section 2.1.2 is used in the analysis of ice feature impacts with ambient ice, resulting in an initial ice feature velocity of 0.79 m/s. Further simulation parameters are similar to the parameters described in Section 4.3.1. (i.e., the structure properties, the friction coefficient, and the CSE).

The test matrix for the geometrical impact scenarios that are modelled is selective comparing to the test matrix used for the spheroidal ice feature and is shown in Table 4.6.

Table 4.6: Test matrix for real ice feature geometry with ambient floe ice.

	Range	Number of values
Ice feature vertical offset	-4.7 to 4.7	3
Ice feature horizontal offset	-50 to 50	5
Ice feature drift direction	0° – 90°	3

A total of 45 simulations are performed for each ice feature geometry. A screenshot of a simulation with ambient ice is show in Figure 4.17.

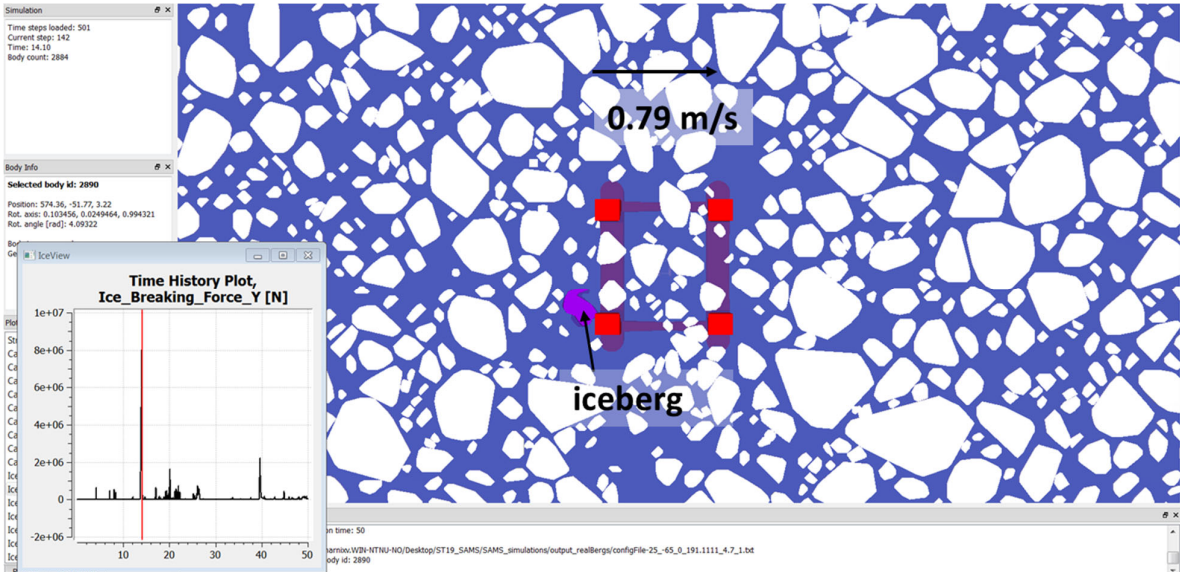


Figure 4.17: Simulation screenshot at the moment of ice feature impact, showing ambient ice conditions and the current direction.

The contact energy and maximum contact force resulting from the ambient ice simulations are shown in Figure 4.18 and Figure 4.19. Even though Ice Feature #1 has a substantially higher mass than the spheroidal ice feature used earlier in this chapter, the dissipated contact energy and maximum contact force are lower than the critical values resulting from the analysis of the spheroidal ice feature in open water. This is mainly caused by the lower impact velocity, since the ice feature is only driven by current and not by waves. The ice floes used in the analysis with ambient ice do not have sufficient momentum to increase the contact energy to values larger than the value caused by the initial ice feature impact.

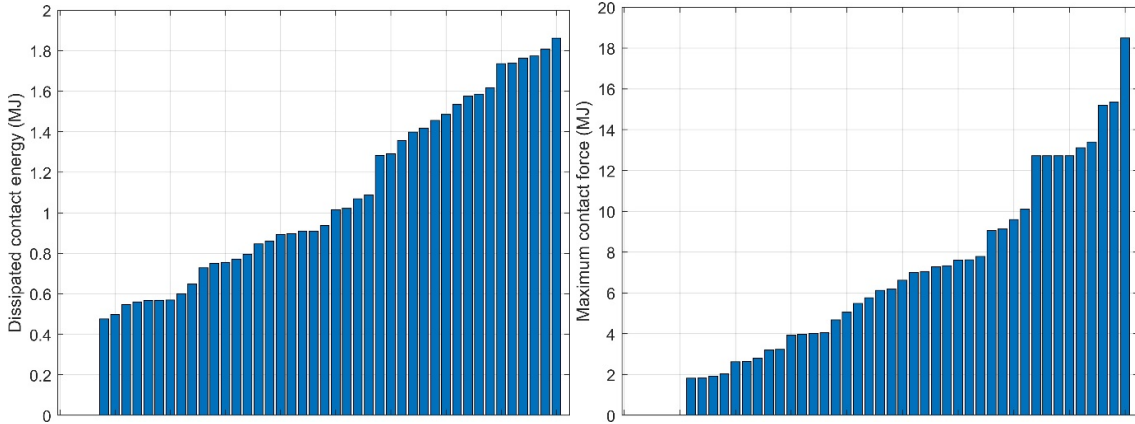


Figure 4.18: Dissipated contact energy and maximum contact force resulting from the simulations with Ice Feature #1 and ambient floe ice.

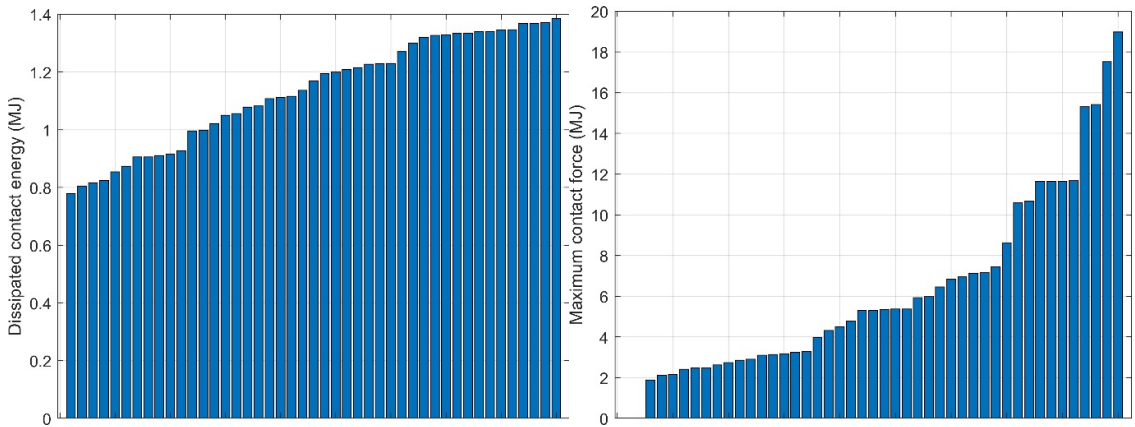


Figure 4.19: Dissipated contact energy and maximum contact force resulting from the simulations with Ice Feature #2 and ambient floe ice.

4.3.8 Summary

In total 1800 simulations were performed using a spheroidal ice feature in open water and for curiosity reasons 90 simulations were performed using two real-life ice feature geometries with the presence of ambient broken ice. The purpose of the simulations was to create an energy map of ice feature's impacts on the semi-submersible structure hull. Differences in velocity and impact probability as a function of impact height were taken into account in post-processing of the simulation results.

- The major finding is that critical impacts mainly occur on the structure legs. Impacts on the pontoons have a very low probability – only 0.6% of impacts will occur on the pontoons under the specified design conditions. The horizontal members which were present in the simulated semi-submersible structure have a substantial probability of impact. However, the impact energy of horizontal member impact is lower, since the hull geometry is inclined at the location of impact, and the impact velocity will be lower than in cases of impact higher up on the structure.
- The maximum impact energy resulting from the simulations is 7.32 MJ. However, high energy impacts have a low probability. About 90% of the simulated open water impacts result in an impact energy lower than 4.3 MJ when accounting for the impact probability and impact velocity

distribution as a function of height as found in Chapter 3. High energy impacts have a low probability because of the correlation between impact probability and impact velocity. High velocity impacts have a lower probability of occurrence.

The results presented in this section are dependent on, and valid for, the assumed ice feature geometries, the used semi-submersible structure geometry and the assumed design sea state. Other assumptions may give different results. In addition, only the horizontal impact scenarios are simulated in this chapter. The potential impact in the vertical direction by the heave motion of an ice feature, as described in Section 3.4.2, are not further analysed due to the time constraint of this project. However, as mentioned in Chapter 3, such vertical impact scenarios might be more decisive to the un-strengthened pontoon compared to the horizontal impact scenarios simulated in this chapter.

5 Assessment of Structural Damage

5.1 Shared-Energy approach in ST19

ISO 19906 specifies that design for Extreme Level (EL) ice actions and Abnormal Level (AL) ice actions shall include both local and global actions. Global actions represent the total action on the structure and are applied over the nominal contact area, while local actions are applied to a specific area within the normal contact area. The actions are often given as pressure-area relationships.

As shown in Figure 5.1 from ISO19906 (2018), the ice pressure distribution for massive ice features is highly non-uniform within the nominal contact area and is rapidly changing during ice-structure interaction. Ice at the boundaries may spall off reducing the actual contact area relative to the nominal contact area. Smaller areas within the nominal contact area can be subjected to pressures considerably larger than the global average pressure. According to ISO 19906, this should be addressed by assessing local design separately using local pressure relationships. This is relevant for structures undergoing small or very moderate plastic deformations, which is normally assumed for EL events.

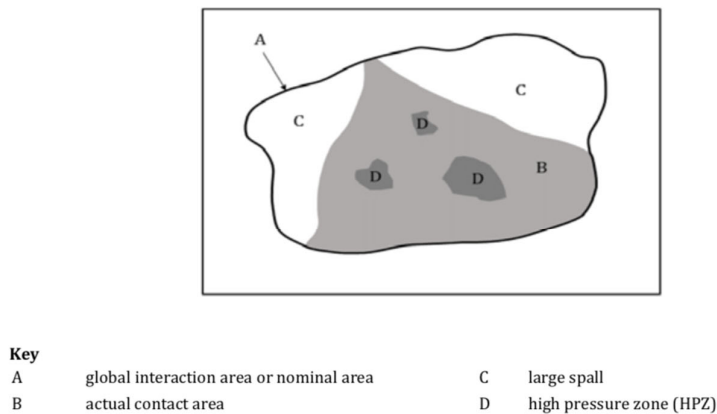


Figure A.8-2 — Illustration of nominal contact area for glacial or massive ice feature interactions

Figure 5.1: ice pressure distribution with ice-structure interactions, taken from ISO19906 (2018).

The approach is not easily applied to structures undergoing deep deformations, which can be considered for AL events, because the *structural resistance* may govern the interface pressure; i.e. plate and stiffeners may deform before the ice reaches the local AL pressure. This implies that the ice maintains its shape in the local high-pressure zones, the local indentation into the structure increases slightly locally, but simultaneously the contact area expands and mobilizes more structural members. Consequently, in the ALS we are not so much concerned about the resistance to local, rapidly varying pressures, but rather the resistance to the global ice actions.

In order to calculate the distribution of energy dissipation between the ice and the structure we will adopt the same principles as those used for ship impact according to NORSOK N-004 Appendix A (NORSOK, 2017).

The principle is sketched in Figure 5.2. The ship may represent the ice feature in the present context. The force-deformation curve for the installation is established assuming the ship to be rigid. Likewise, the force-deformation curve for the ship is established assuming the installation to be rigid. The resulting

damage is determined when the energy dissipation (equal to the area under force deformation curves) reaches the *demand* for energy dissipation, as determined by the external mechanics analysis.

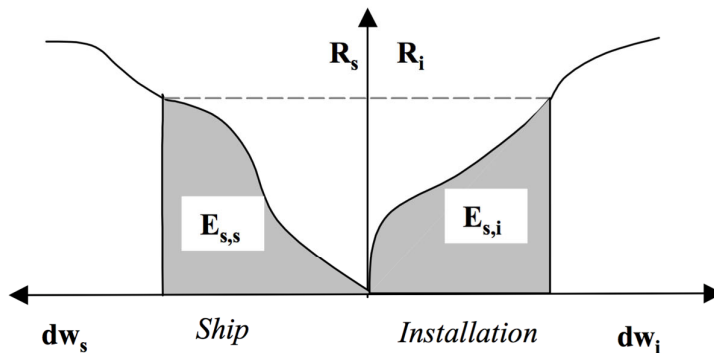


Figure A.3-3 Dissipation of strain energy in ship and platform

$$E_s = E_{s,s} + E_{s,i} = \int_0^{W_{s,max}} R_s dw_s + \int_0^{W_{i,max}} R_i dw_i$$

Figure 5.2 Estimation of force and damage (deformation) for ship impact against an installation according to NORSOK N-004.

It is noted that this approach does not take the coupling of interaction effects into account; deformation of the ship bow increases the contact area and may hence increase the resistance of the installation. Simplified methods to account for this interaction are proposed in a proposed revision of DNV-GL RP-C204, (which is virtually identical to NORSOK N-004).

Similarly, interaction effects exist for ice-structure impacts, but these are associated with significant uncertainties at present. Hence, coupled ice-structure interaction will be neglected in the current investigation.

In summary the following procedure will be used to determine the damage and energy dissipation:

- Analysis principles for ship-installation impacts in NORSOK N-004/DNV-GL RPC204 will be adopted.
- Extreme local pressures over limited areas will not be considered; it is the resistance to the total force that is essential in the ALS.
- Coupled analysis of the interaction between structural deformation and ice crushing is at present stage not viable and will be disregarded.
- Only the critical impacts scenarios identified in Chapter 4 will be further analysed in this Chapter for assessment of structural damage. The analysis procedure illustrated in Figure 5.3 and are summarized below:
 - a. Force-deformation relationships for the ice will be established using SAMS, i.e., by analysing ice impacts against a rigid structure.
 - b. Force-deformation relationship for the structure will be established using NLFEM analysis in LS-DYNA, i.e., by analysing rigid ice impacts against the structure.

- c. The crushing of the ice and the structure damage is determined such that the total energy dissipation is equal to the demand for energy dissipation, as determined by the external mechanics analysis in Chapter 4.
- The above procedure will be sufficiently accurate as long as the impact period is small compared to the relevant eigenperiods, i.e., the impact force and inertia forces predominate the response.

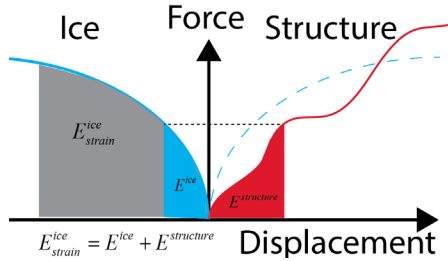


Figure 5.3 Determination of resulting damage in ice and structure.

5.2 Force-deformation curves for the ice feature using SAMS

As discussed in Section 4.3.3, the SAMS results include the contact energy dissipation as a function of time, as well as the occurring contact forces. The contact energy dissipation can be used in combination with the contact forces to derive a force-deformation curve from the SAMS results for the ice feature. Both the contact energy dissipation as well as the contact force depend on the crushing specific energy (*CSE*) of the ice feature, which is a necessary input parameter of SAMS. The *CSE* is the amount of energy needed to crush a unit volume of ice (unit: kJ/m³). Section 5.2.1 describes how the *CSE* used in SAMS is determined. Section 5.2.2 describes how the effective ice feature force-deformation curve is calculated from the SAMS results. Section 5.2.3 presents an alternative method for calculating force deformation curve in the absence of SAMS calculations.

5.2.1 Data source and method for establishing *CSE*

The crushing specific energy (*CSE*) of the ice feature is obtained by analyzing full-scale data from in-situ indentation experiments. Through personal communication, we were granted access to the Pond Inlet test data (Geotech Arctic Services, 1985), and we re-analysed the data set. Force-time histories for the spherically-ended indenters with radius $R=900$ mm, 1280 mm and 2300 mm are gathered (ten sets in total). Negative force values are excluded from the analysis. The data sets have been converted from force-time histories to force-displacement history. The indenter displacement, u , during each test was controlled according to the following equation: $u=0.1R \cdot \sin(0.4348t)$, where t is time.

Method

1. To avoid scale effects caused by small strained volumes in relation to the grain size, data points from outmost 5.0 cm of ice have been excluded from the analysis. Penetration depth at the conclusion of the test is $0.1R$.
2. For each data point, the crushing specific energy is calculated as:

$$\psi(u_j) = \frac{\int_0^{u_j} F du}{\frac{1}{3}\pi u_j^2 (3R - u_j) \rho} \quad (5.1)$$

where ψ is the crushing specific energy, F is the measured force, u is displacement of the indenter, R is the indenter radius and ρ is the ice density ($\rho=900 \text{ kg/m}^3$)

3. For NN scalar data points, the average is defined as

$$\psi_\mu = \frac{1}{NN} \sum_{k=1}^{NN} \psi_k \quad (5.2)$$

The resulting average value $\psi_\mu = 2.96 \text{ kJ/kg}$, range is from 1.30 kJ/kg to 6.09 kJ/kg .

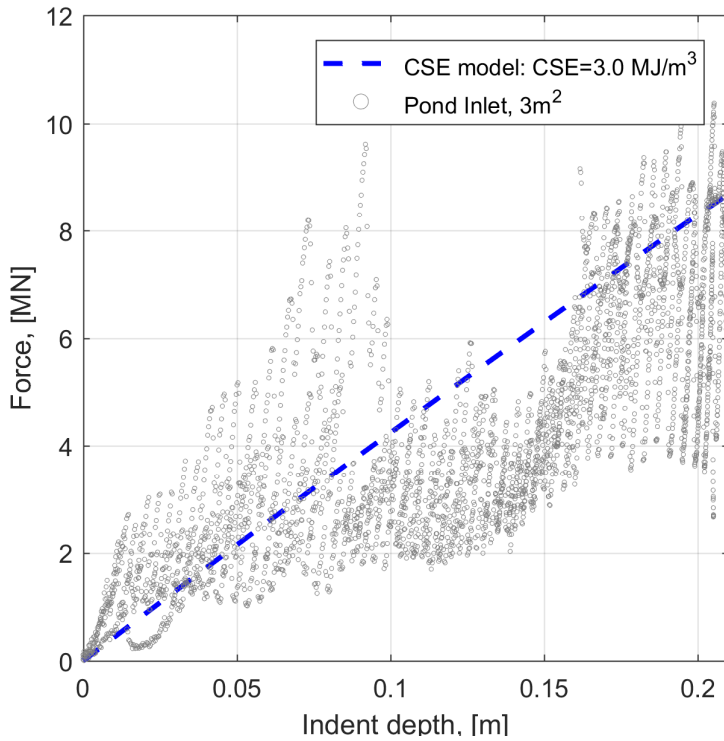


Figure 5.4 Pond Inlet data and CSE model curve.

Based on the above results, *CSE* in SAMS is chosen as 3.0 MJ/m^3 (Figure 5.4). Note that with this approximation method, the high-frequency variation in the contact force, caused by local failure events such as spalling, recrystallization and cracking will not be visible in the SAMS results.

5.2.2 Reconstruction of force-deformation curve from the SAMS results

Force-deformation curves of the ice feature are reconstructed from the SAMS output using the dissipated contact energy and the contact force. The resulting force-deformation curve depends on the local ice feature geometry, the local hull geometry, and on the assumed *CSE* value. The deformation in the force-deformation curves derived using this method can be seen as an effective deformation, defined such that the integral of the force – deformation curve results in the simulated energy dissipation for the contact geometry of interest. The deformation is defined as:

$$D(t)|_{t_1} = \int_0^{t_1} \frac{P(t)}{F_n(t)} dt \quad (5.3)$$

in which D is the ice feature deformation (unit: m), P is the impact energy dissipation rate (unit: W) and F_n is the contact force in normal direction (unit: N). Using this definition of ice feature deformation, the energy dissipated in ice crushing corresponds to:

$$E(D)|_{\delta} = \int_0^{\delta} F_n(D) dD \quad (5.4)$$

In which E is the energy dissipated in ice crushing. This definition of deformation corresponds to the deformation definition that is used in the shared energy approach discussed in Section 5.1. For the three critical scenarios as identified in Section 4.3.6, the force deformation curves of the ice feature are derived from the contact force and energy dissipation resulting from SAMS. As an example, the contact normal force, the energy dissipation rate and the resulting effective ice feature deformation are shown in Figure 5.5.:

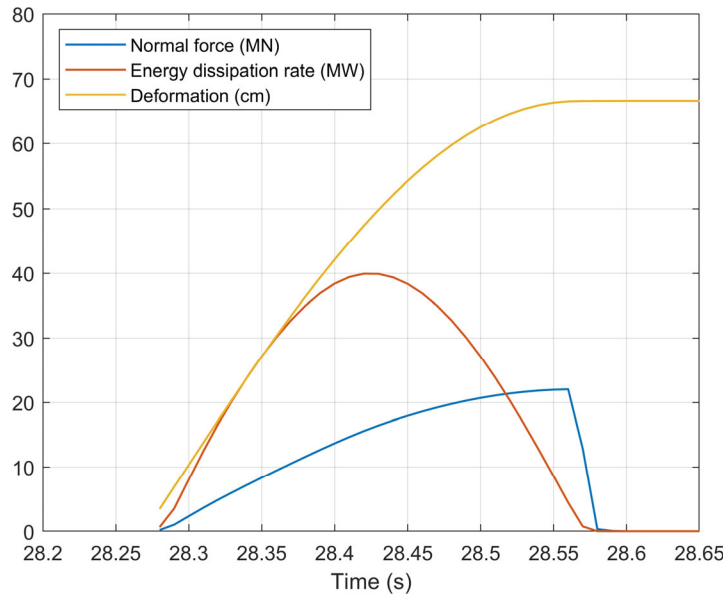


Figure 5.5: The contact normal force, the energy dissipation rate, and the resulting effective ice feature deformation for critical Scenario 1. Units are chosen such that the normal force, energy dissipation rate and the deformation can be shown in one figure.

Figure 5.6 shows the force-deformation curves for the critical scenarios identified in Section 4.3.6. Scenario 1 has a displacement-force curve that is substantially different from the force-deformation curves found for Scenarios 2 and 3.

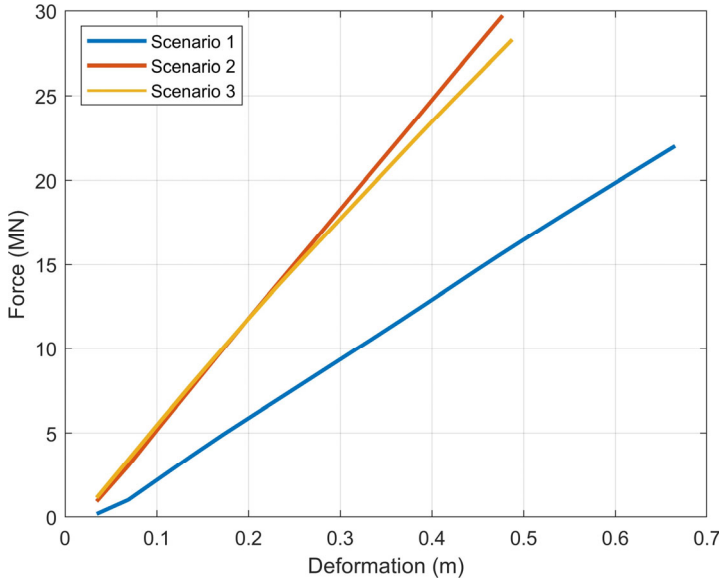


Figure 5.6: Force-deformation curves for the three critical scenarios.

This is caused by a difference in hull geometry at the structure-ice feature contact point. In Scenario 1, the ice feature impact on a corner of a structure leg, as visualized in Figure 5.7 on the left. Scenarios 2 and 3 impact on the planar side of a structure leg, as visualized in Figure 5.7 on the right.

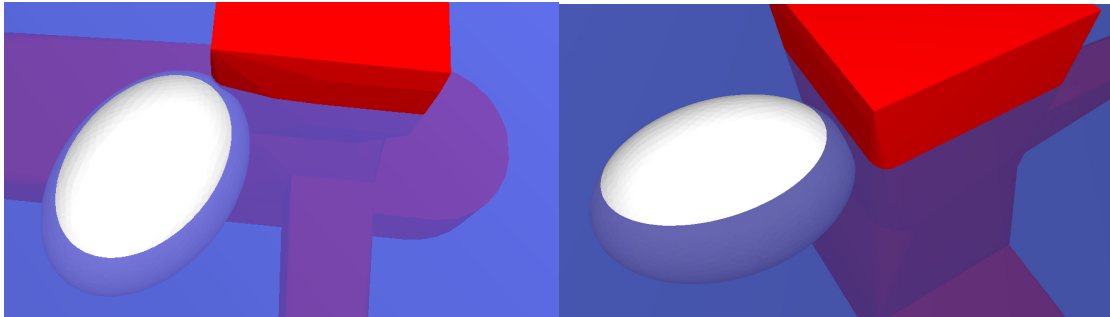


Figure 5.7 Ice feature impact in critical Scenario 1 (left) and in critical Scenario 2 (right).

5.2.3 Simplified method

In the absence of SAMS calculations, it is possible to use the deterministic simplified method as described below.

Given the local shape of the ice feature and the structure at the impact location, ice feature loads, which result in ALS, are expressed by a force-deformation curve, corresponding to the power-law expression $p=CA^{ex}$ (the process pressure-area curve), where A is the nominal contact area C and ex are constants derived from in-situ/full-scale tests on natural ice and taking into consideration the energy absorption capacity of ice.

As alternative to SAMS calculations, the force-deformation curve can be established using medium-scale empirical data sets on natural iceberg ice. The ice load model $F=CA^{1+ex}$ with $C=3.2$ MPa and $ex=-0.1$ accounts for physically plausible energy absorption capacity of freshwater ice during ice feature-structure interaction process (refer to Figure 5.8). The same ice-load model is used by the International Association of Classification Societies ((IACS), 2011) for calculating energy dissipation in ice for PC3 ice class vessels.

Comparison of simplified force-deformation curves with in-situ measurements

Figure 5.8 is a comparison between the measured force-deformation data and the simplified ice load model with $C=3.2$ MPa and $ex=-0.1$.

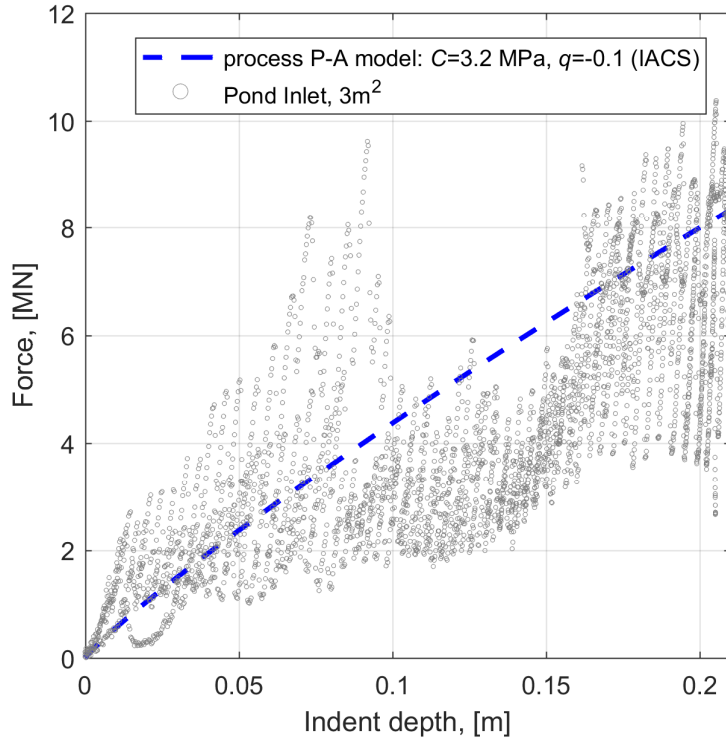


Figure 5.8 Comparison between pressure-area load model and measured force.

Comparison of experimental data and calculated force values shows that the ice load model with $C=3.2$ MPa and $ex=-0.1$ can account for average value of the energy absorption capacity of ice feature during interaction.

Within the context of the methodology used in this study, we recommend that if a pressure-area curve is used to represent the ice loads resulting in ALS, then it has also to be documented that the resulting force-deformation curve accounts for physically plausible values of the energy absorption capacity of ice.

5.3 Force-deformation curves for the structure using Non-linear FEM analysis in LS-DYNA

The demand for energy dissipation calculated from SAMS should be dissipated by ice crushing and structural deformations. The structural response will be calculated by NLFEM analysis in LS-DYNA and simplified methods. This section describes finite element modelling of the structure column, material and fracture modelling, simplified formulations for structural components, and discussion of the simulation and analytical results.

5.3.1 Finite Element Modelling

5.3.1.1 The structure column model

The column leg (C10, S10) of the Midgard structure was modelled by Tavakoli and Amdahl (2010) for the assessment of structure strength against supply vessel impacts. The drawings of the structure column are shown in Figures 5.9, 5.10 and 5.11. The column was modelled from EL8125 through EL39000. Only the front part of one leg was modelled. The overall dimension of the column FE-model is 17200 mm x 308750 mm x 6100 mm (w x h x d).

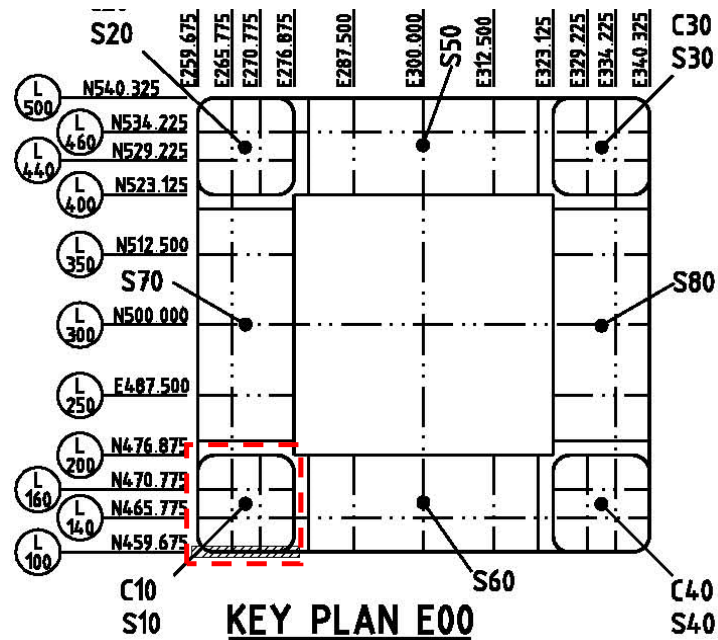


Figure 5.9: the Midgard structure

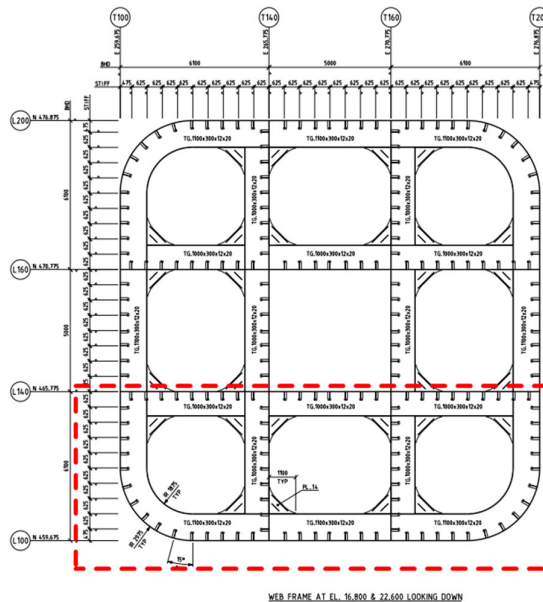


Figure 5.10. The section of the column.

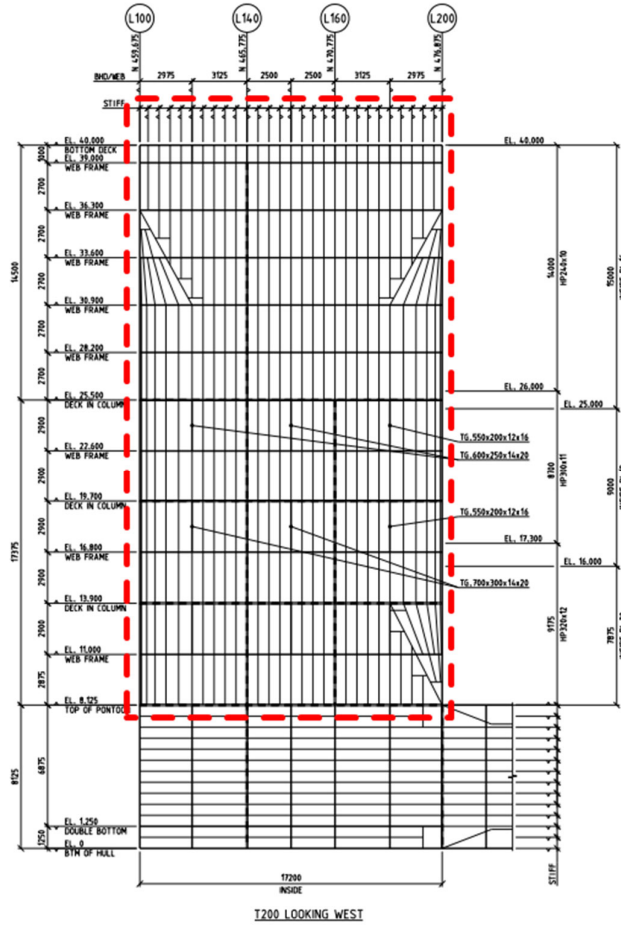


Figure 5.11. The structure column.

The finite element models of the column is shown in Figure 5.12. The column outer shell is in the range of 16-18 mm. The vertical stiffeners used in the column are HP320x12, HP300x11 and HP240x10. These stiffeners were modelled as L-bars with dimensions 320x50x40x12 (mm), 300x50x50x11 (mm) and 240x40x30x10 (mm). This gives nearly the same height, width and the cross sectional area as the HPs. The column model was meshed using approximately 245,000 4-noded shell elements. The general element size is 120 mm.

Numerical simulations were carried out by using explicit NLFE software LS-DYNA 971. The four-node Belytschko-Lin-Tsay shell element with reduced integration was used with 5 integration points through the thickness. Hourglass stiffness is added using the stiffness based form (option 4 in LS-DYNA). This is very efficient and gives low dissipation of spurious hourglass energy of less than 2-3%. The rear side, the top and the bottom of the column are constrained in all degrees of freedom (translation in direction of x-, y- and z-axis and rotation around x-, y- and z-axis). The rigid ice model is given a prescribed motion velocity of 3 m/s, and any strain rate effect is not taken into account. Two kinds of contacts are defined in this analysis, which are the self-contact and master-slave contact. For the rigid ice-column impact, the master-slave contact is used with the column being the slave part. Self-contacts are defined for the column model to detect possible contacts due to deformation. A static friction coefficient of 0.3 was used for all the contacts.

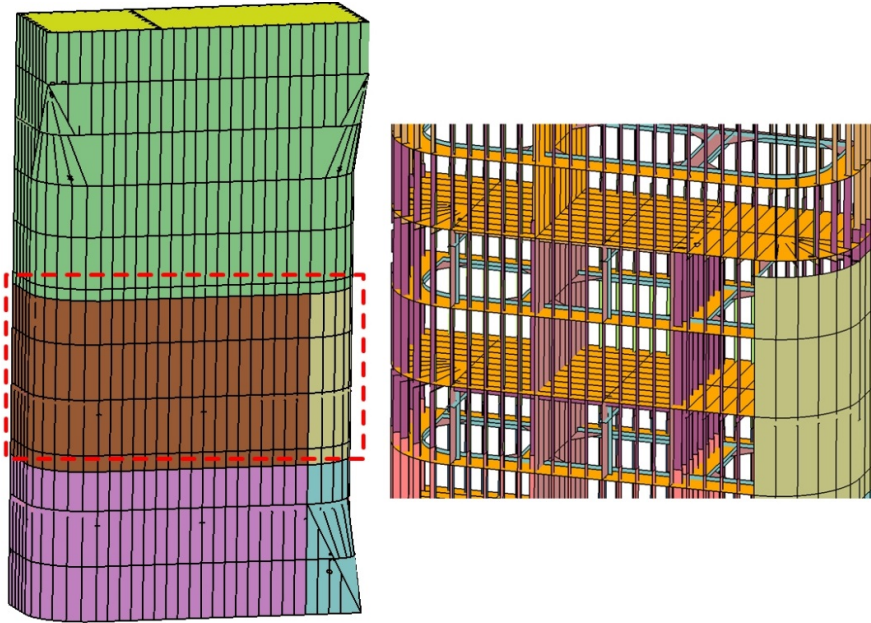


Figure 5.12. The finite element model of the structure column.

5.3.1.2 Material and fracture modelling

Material and fracture modelling are crucial to determine the structural strength in the ice impact analysis. Material fracture will degrade the structural strength to and beyond the point of collapse. Another effect is leakage and flooding of compartments, leading to stability problems. It is very challenging to accurately simulate fracture initiation and propagation with large scale shell elements. The complexity lies in that fracture is a localized phenomenon in the length scale of plate thickness, and is difficult to capture with large shell elements, the sizes of which are several times larger than the plate thickness. In addition, fracture depends highly on the stress state, material deformation history and is sensitive to the mesh size adopted. It is essential to correctly calibrate the material properties in order to capture accurately strain localizations and the subsequent fracture. The probabilistic nature of material properties makes the fracture modelling even more complicated (Yu and Amdahl, 2018). Due to the significance of material and fracture modelling and its physical complexity, a proper model is necessary for achieving realistic results.

For material modelling, the power law hardening with a yield plateau is used to model the material. The hardening is described by the yield criterion

$$f = \sigma_{eq} - \sigma_f(\varepsilon_{eq}) = 0 \quad (5.5)$$

where σ_{eq} is the von-Mises equivalent stress. The current flow stress σ_f is a function of the equivalent plastic strain ε_{eq} via the Hollomon-type power law hardening rule:

$$\sigma_f(\varepsilon_{eq}) = \begin{cases} \sigma_0 & \text{if } \varepsilon_{eq} \leq \varepsilon_{plateau} \\ K(\varepsilon_{0,eff} + \varepsilon_{eq})^n & \text{if } \varepsilon_{eq} > \varepsilon_{plateau} \end{cases} \quad (5.6)$$

where K and n are the hardening parameters and σ_0 is the initial yield stress. To account for the existence of a strain plateau, the hardening is delayed until the plastic strain reaches the plateau strain $\varepsilon_{plateau}$. Thus, $\varepsilon_{0,eff}$ is defined by the relation

$$\varepsilon_{0,eff} = \varepsilon_0 - \varepsilon_{plateau} = \left(\frac{\sigma_y}{K} \right)^{1/n} - \varepsilon_{plateau} \quad (5.7)$$

where ε_0 is the strain at initial yield

The BWH (Bressan-Williams-Hill) instability criterion is used to model fracture in the ice impact simulation. The BWH instability criterion was proposed by Alsos et al. (2008), which combines Hill's local necking model (Hill, 1952) and the Bressan-Williams shear stress criterion (Bressan and Williams, 1983). The BWH criterion considers that fracture occurs at the onset of local necking instability neglecting the post-necking regime, and this is conservative. The BWH criterion has been validated of good accuracy by comparison with various impact experiments (Storheim et al., 2015, Marinatos and Samuelides, 2013). The BWH criterion can in the principle stress space be expressed as follows:

$$\sigma_1 = \begin{cases} \frac{2K}{\sqrt{3}} \frac{1+\frac{1}{2}\beta}{\sqrt{\beta^2 + \beta + 1}} \left(\frac{2}{\sqrt{3}} \frac{\hat{\varepsilon}_1}{1+\beta} \sqrt{\beta^2 + \beta + 1} \right)^n & \text{if } -1 < \beta \leq 0 \\ \frac{2K}{\sqrt{3}} \frac{\left(\frac{2}{\sqrt{3}} \hat{\varepsilon}_1 \right)^n}{\sqrt{1 - \left(\frac{\beta}{2+\beta} \right)^2}} & \text{if } 0 < \beta \leq 1 \end{cases} \quad (5.8)$$

β is the ratio of the minor and the major principal strain rates, $\beta = \dot{\varepsilon}_2 / \dot{\varepsilon}_1$. The critical strain $\hat{\varepsilon}_1$ can be assumed to be equal to the power law coefficient n in accordance with Hill's criterion.

Fracture is simulated by eroding the failed elements when the fracture criterion is fulfilled. A through-thickness integration point is failed by setting the stresses to zero once a failure criterion is satisfied. Final element erosion occurs once the middle integration point fails. This approach is preferred over requiring all integration points to fail prior to erosion because nodal fibre rotations in elements undergoing large strains may limit the strains in the remaining integration points, thus resulting in no erosion of the element.

Two kinds of steel material grades are used for the structure materials, and the material properties are shown in Table 5.1. The outer shell material is with a yield stress of 420 MPa, while the stiffeners are modelled with a 355 MPa yield stress steel.

Table 5.1: Properties of the steel material

Steel Grade	Young's Modulus (MPa)	Yield Strength (MPa)	Poisson Ratio	Power law K (MPa)	Power law n	$\varepsilon_{plateau}$
Plate	2.07×10^5	420	0.3	860	0.16	0.0
HP	2.07×10^5	355	0.3	780	0.22	0.0

5.3.1.3 Definitions of impact scenarios

The potential impact locations depend upon the size and draft of the structure and the ice. In addition, wave-induced relative motions of the structure and the ice increase the vertical extension of the impact exposed area. From the probabilistic analysis of motions in waves and current, potential impact locations varies from 5.5 m above the waterline to 10 m below the waterline. From the point of view of structural arrangements, several representative impact locations are selected on the column as shown in Figure 5.13, including the column corner, column bulkhead and cruciform, and stiffened panels of column front. The impact scenarios are shown in Figure 5.14.

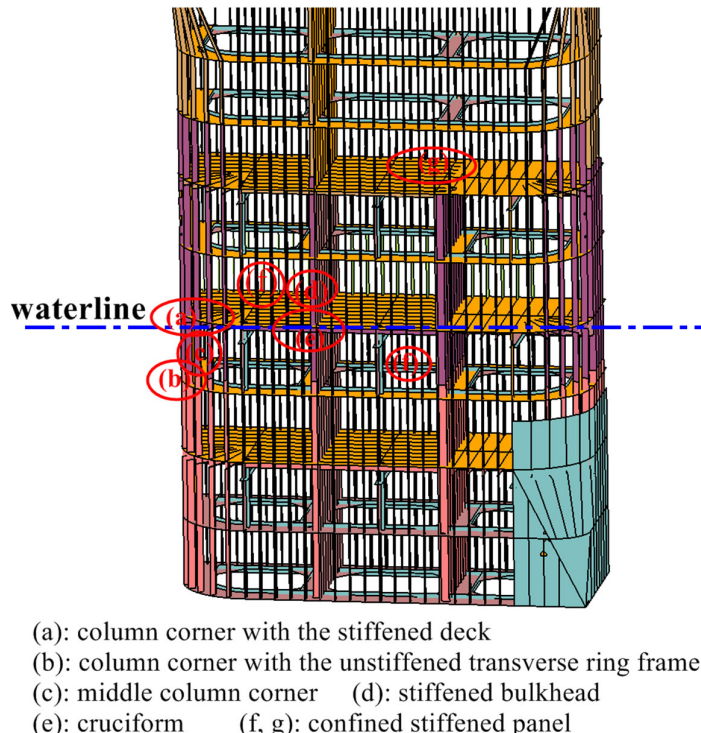


Figure 5.13. The impact locations.

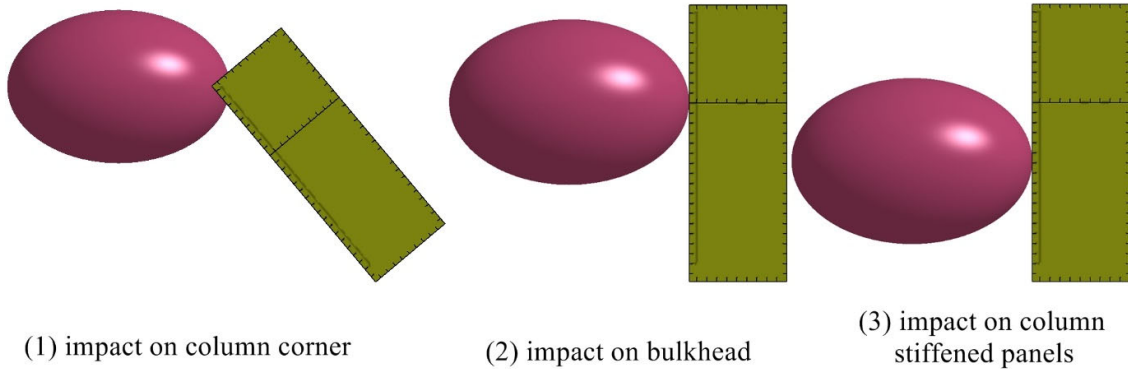


Figure 5.14. The impact scenarios.

5.3.2 Non-linear FEM analysis

5.3.2.1 Scenario (a), (b) and (c): impact on the column corner

Ice impacts on the column corner are studied first, including impacts on (a) stiffened deck, (b) the transverse frame and (c) the column corner in between (a) and (b) (refer to Figure 5.13). Take impact scenario (a) as an example, and the sectional cut of column deformation at different time instants are given in Figure 5.15. Note that the impact velocity is 3 m/s. As the crushing distance increases, buckling of the stiffened deck and HP stiffeners are clearly observed until final fracture. Deformation and fracture of the column corner structure at an indentation of 1.5 m is plotted in Figure 5.16.

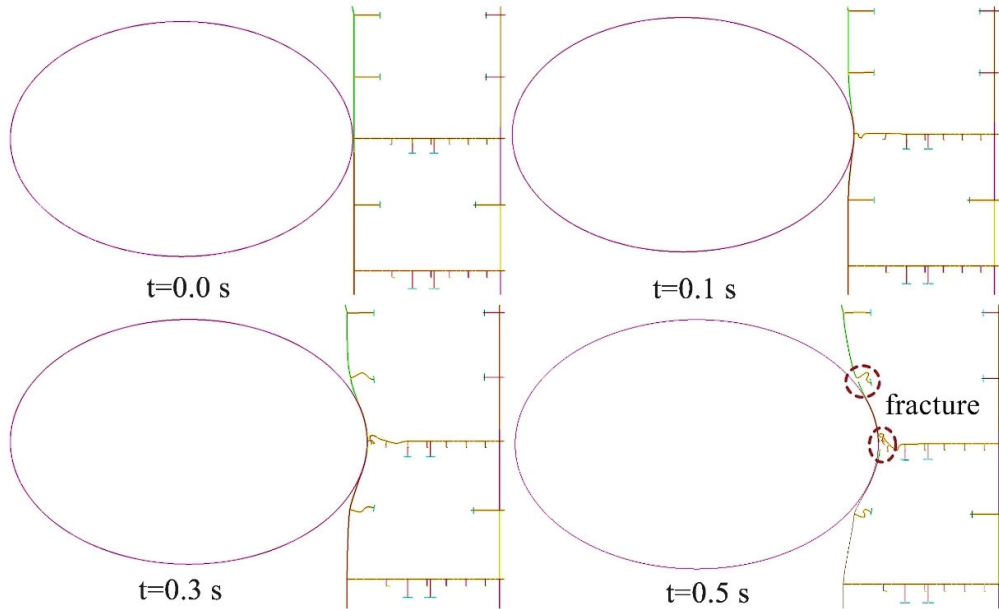


Figure 5.15. Snapshots of the impact scenario (a) on the stiffened deck (side view).

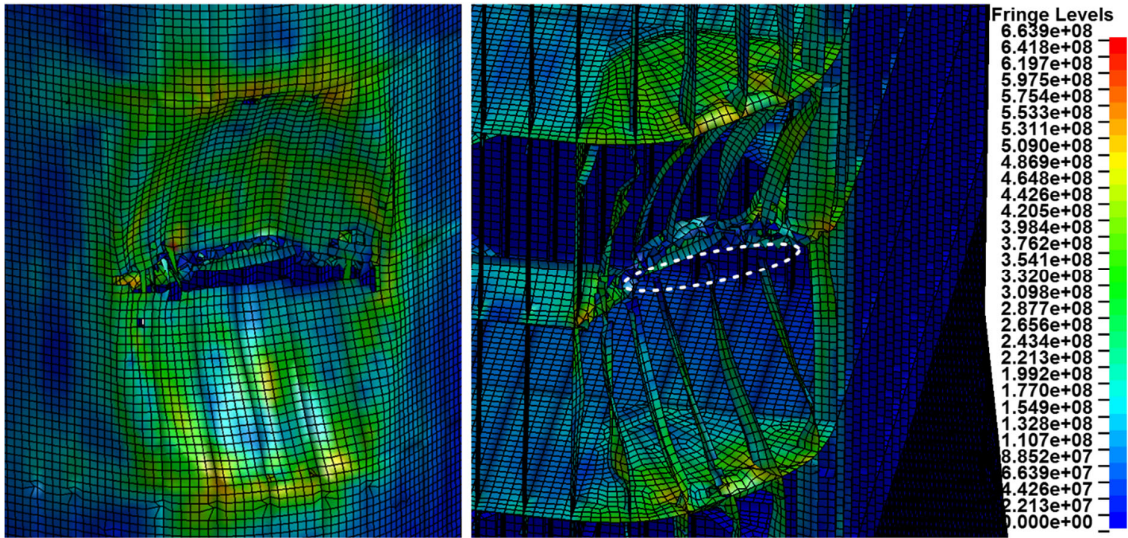


Figure 5.16. Deformation and fracture of the column corner in scenario (a) at an indentation of 1.5 m.

The rigid ice crushing resistance and energy with increasing crushing length is plotted in Figure 5.17, and the outer shell fracture initiation is marked with short bold lines. Results show that the initial bending capacity of the column corner on the stiffened deck and the transverse frame is about 5 MN. As crushing continues, the indentation resistance increases. Initial outer shell rupture occurs at a crushing length of 0.6 m-0.9 m.

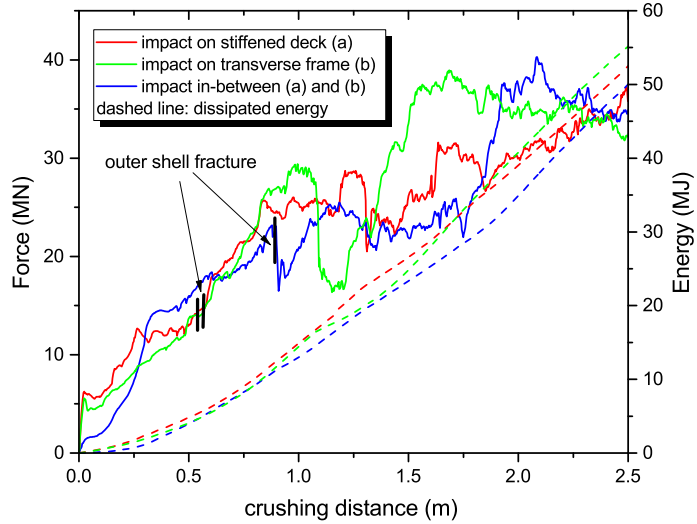


Figure 5.17. Rigid ice crushing resistance and energy versus crushing distance for scenario (a)-(c).

5.3.2.2 Scenario (d) and (e): impact on the bulkhead and cruciform

Rigid ice impacts on the bulkhead and the cruciform of the structure column are studied. The crushing resistance and energy of the structure with increasing crushing distances are plotted in Figure 5.18, and the outer shell fracture is marked as well. The column bulkhead and the cruciform represent hard points

of the column structure. The initial collapse capacity of the bulkhead and the cruciform are about 7.0 MN and 12.5 MN, respectively, below which little structural damage will be expected. The outer shell fracture occurs at about a crushing distance of 0.5-0.9 m.

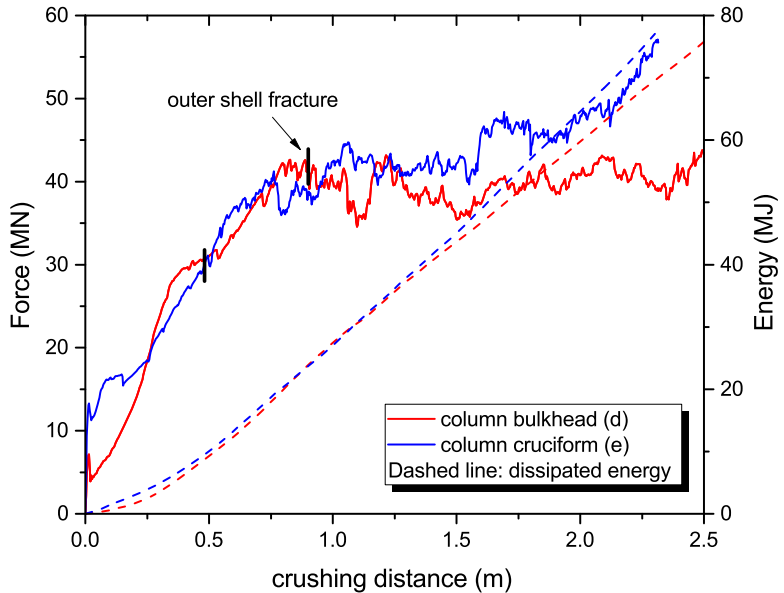


Figure 5.18. Rigid ice crushing resistance and energy with crushing distance for scenario (d)-(e).

The outer shell fracture for the impact scenario (d) at a crushing distance of 1.15 m is shown in Figure 5.19. Fracture propagates along the root of the bulkhead and the transverse frame. As the crack involves two adjacent compartments and propagates further to four compartments, this is considered critical for compartment flooding.

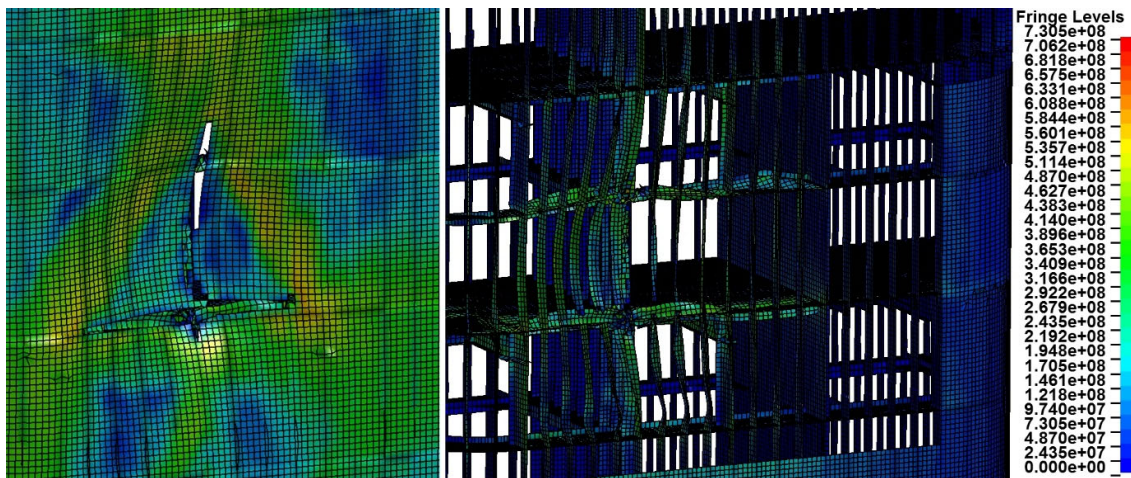


Figure 5.19. Structural deformation of impact scenario (d) on the bulkhead at a crushing distance of 1.15 m.

5.3.2.3 Scenario (f) and (g): impact on the column stiffened panels

Rigid ice impacts on the column stiffened panels are simulated. A top view of the column deformation of scenario (f) at different time instants are given in Figure 5.20. As the crushing distance increases, deformation and buckling of the stiffened panels are clearly observed, and the column bulkhead gets involved later in the deformation till final fracture. The stiffened panel deformation is plotted in Figure 5.21.

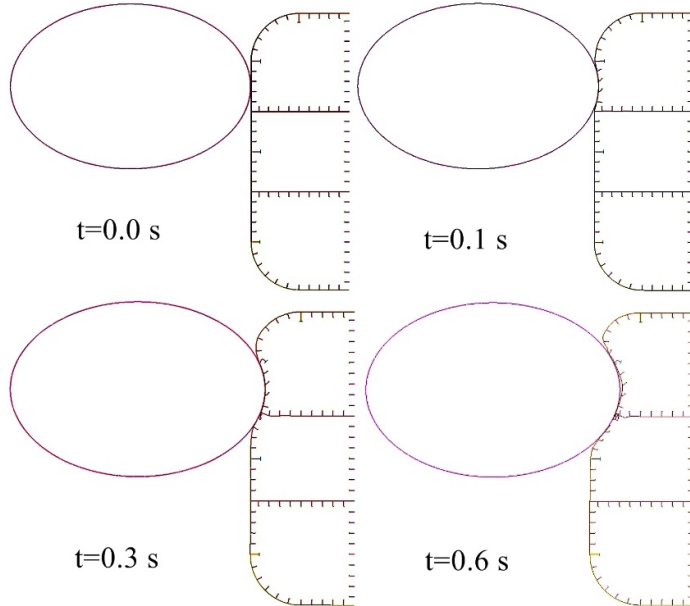


Figure 5.20. Snapshots of the impact scenario (f) on the stiffened panel (top view).

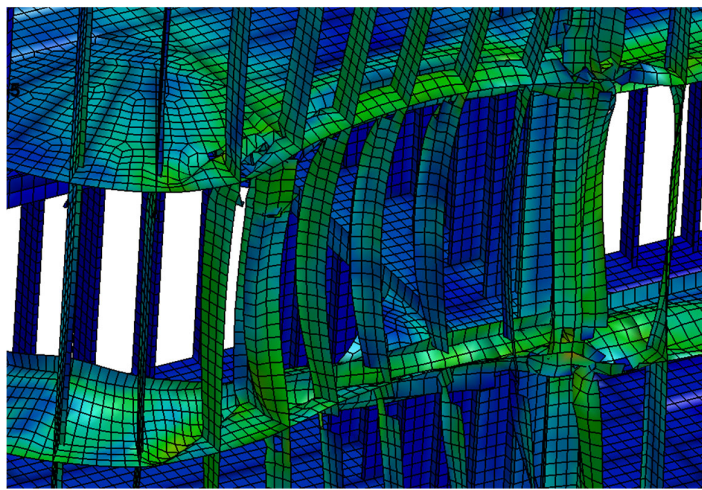


Figure 5.21. Structural deformation of impact scenario (f) at a crushing distance of 0.9 m.

The crushing resistance and energy of scenario (f) and (g) with increasing crushing distance is plotted in Figure 5.22, and the outer shell fracture is marked. Results show that resistance increases as crushing continues, and the initial outer shell rupture occurs at a crushing distance of about 0.6 m.

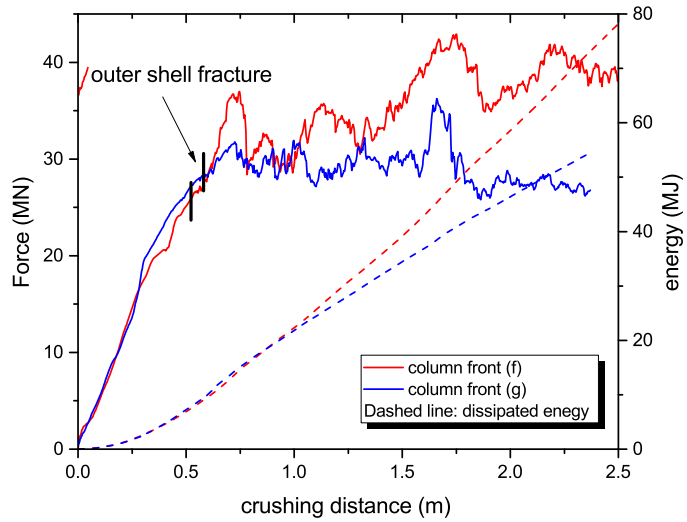


Figure 5.22. Rigid ice crushing resistance and energy for scenario (f)-(g) on stiffened panels.

5.3.3 Simplified analytical formulation of structure frames to ice loading

One of the objectives of the project was to establish simplified formulations for assessment of the resistance to deformation and energy dissipation in semi-submersible structure. The development was supposed to be based on existing knowledge of stiffened panel, bulkheads and decks subjected to deep deformation due to ship impact or other accidental events. The results of this work are presented along with comparison with data from NLFEM with LS-DYNA. Because a finite element model for a structure column was available, NLFEM was carried for various impact scenarios. As it is often of interest to conduct simplified calculations, notably in the early design stage, it is considered worthwhile to present the background for the simplified calculations methods.

5.3.3.1 Beam response of a stiffened panel strip under point and patch loading

The assessment of structural resistance for a stiffened panel strip with associated plate flange undergoing finite deformations is carried out in accordance with the recommended practice DNV-GL-RP-C204 Design against accidental loads (Updated, unreleased version – July 2017). The formulas is based on the work by Yu et al. (2018). The total resistance is considered to consist of a bending contribution and a membrane contribution for finite deflections as illustrated in Figure 5.23.

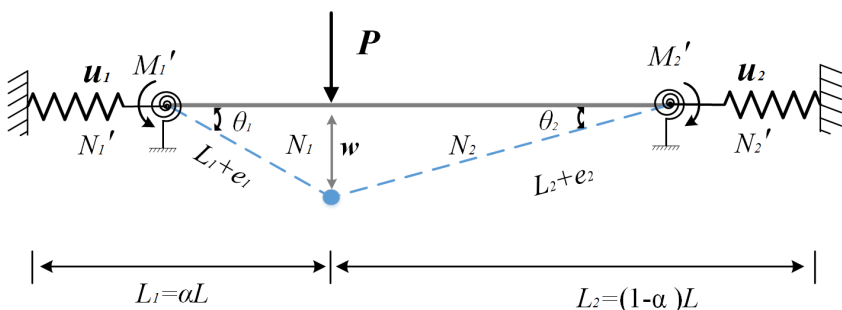


Figure 5.23. Model for the assessment of structural resistance for stiffener with plate flange during large deflection and finite axial stiffness. k is stiffness against inward motion.

The resistance is given by the following set of equations:

$$\frac{P}{P_0} = \frac{M}{M_p} + \frac{N\delta}{\beta M_p}; \quad \beta = \begin{cases} 1 & \text{free rotation} \\ 2 & \text{fixed rotation} \end{cases} \quad (5.9)$$

where, the resistance to plastic bending, P_0 , plastic bending moment, M_p , and plastic axial force, N_p , of the stiffener with associated plate flange are given by Eq. 5.10.

$$\begin{aligned} P_0 &= \beta M_p \left(\frac{1}{\alpha L} + \frac{1}{(1-\alpha)L} \right) \\ M_p &= \sigma_y \left(\frac{1}{2} A_w h_w + A_t h_w \right) \\ N_p &= \sigma_y A_e \end{aligned} \quad (5.10)$$

The development of the membrane force is determined by:

$$\begin{aligned} \frac{N}{N_p} &= \left[\frac{16}{\beta^2 c} \left(\frac{A_w}{A_e} \right)^2 - \left(2 \frac{A_p}{A_e} - 1 \right) \right] \left[\exp \left(- \frac{\beta c}{4} \frac{A_e}{A_w} \frac{\delta}{h_w} \right) - 1 \right] \\ &\quad + \frac{4}{\beta} \frac{A_w}{A_e} \frac{\delta}{h_w}; \quad \left(\text{stage } 1, 2, 3 : \frac{N}{N_p} < 1 \right) \end{aligned} \quad (5.11)$$

$$\frac{N}{N_p} = 1; \quad \text{stage 4}$$

where c is the non-dimensional axial stiffness given by:

$$c = \frac{k_{eq} h_w^2}{\alpha(1-\alpha)L N_p} \quad (5.12)$$

The development of the bending moment is calculated from:

$$\begin{aligned} \frac{M}{M_p} &= 1; \quad \left(\text{stage 1} : \frac{N}{N_p} \leq \frac{2A_p}{A_e} - 1 \right) \\ \frac{M}{M_p} &= 1 - \frac{1}{4} \frac{1}{1 + 2 \frac{A_t}{A_w}} \left(\frac{A_e}{A_w} \right)^2 \left(\frac{N}{N_p} - \left(\frac{2A_p}{A_e} - 1 \right) \right)^2; \quad \left(\text{stage 2} : \frac{2A_p}{A_e} - 1 < \frac{N}{N_p} < 1 - \frac{2A_t}{A_e} \right) \\ \frac{M}{M_p} &= \frac{\frac{A_e}{A_w}}{1 + 2 \frac{A_t}{A_w}} \left(1 - \frac{N}{N_p} \right); \quad \left(\text{stage 3} : 1 - \frac{2A_t}{A_e} \leq \frac{N}{N_p} < 1 \right) \\ M &= 0; \quad \text{stage 4} \end{aligned} \quad (5.13)$$

The resistance of the stiffened plate strip depends upon the non-dimensional axial flexibility $c(k)$, the relative size of the plate flange vs stiffener area ($A_p/A_s \geq 1$) and the size of the top flange versus the web area (A_f/A_w), as shown in Figure 5.24. In the present case, it will be reasonably representative to assume that $c(k)$ is large.

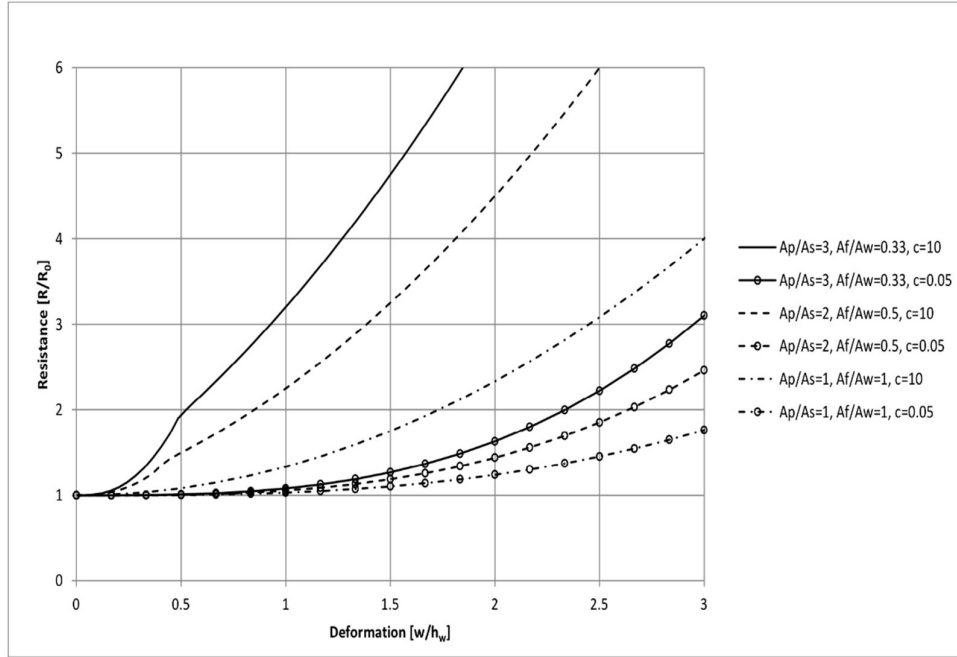


Figure 5.24. Illustration of large deflection resistance curve for stiffened plating (DNV-GL RP-C204, revision July 2017).

For a stiffened panel strip under pressure patch loading (refer Figure 5.25), the pressure p is given by,

$$p = \frac{P}{WB} \left(1 - \frac{B}{2L} \right) \quad (5.14)$$

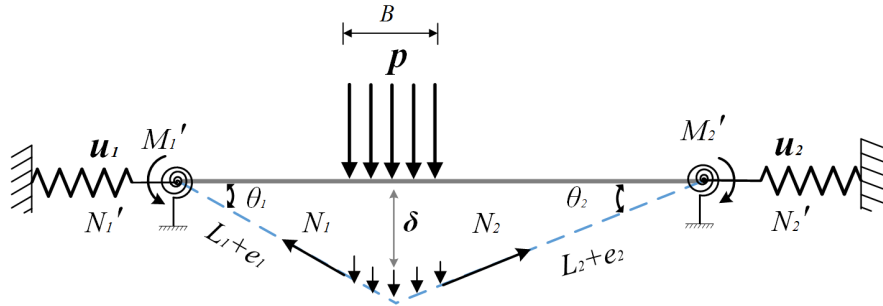


Figure. 5.25. Beam deformation under patch loading.

5.3.3.2 Stiffened panel response under patch and uniform loading

The resistance of stiffened panels with several stiffeners and with fixed boundaries along both transverse and longitudinal directions is analysed. The beam model in *Section 5.3.3.1* only takes into account the resistance in the stiffener direction. For stiffened panels undergoing large deflections, membrane forces developed in the transverse direction should be added. Figure 5.26 shows a stiffened panel under patch

loading with the patch length B . The panel length is L and the panel width is W . It is assumed that the bottom plate of the stiffened panel will be in biaxial state during loading while the stiffeners are in the uniaxial stress state.

According to von-Mises yield criterion, the membrane stress in two orthogonal directions may reach the yield stress, see Figure 5.27. Hence, the contribution from transverse tensile membrane stress will be taken into account with no reduction of the load-carrying capacity in the stiffener direction.

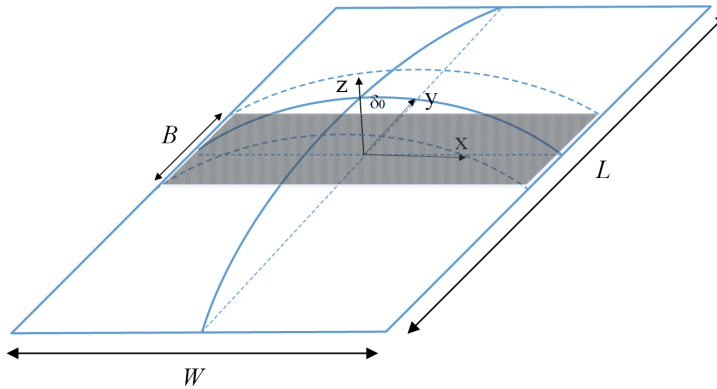


Figure 5.26. The panel deflection under pressure loading.

Thus, for the simplified formulation of a stiffened panel under patch loading, it is assumed that the panel resistance consists two main contributions: beam response along the stiffener direction and plate response of bottom plate perpendicular to the stiffener direction. Along the stiffener direction, we use the beam model of stiffened panel strips as presented in *Section 5.3.3.1*. Perpendicular to the stiffener direction, we assume that only membrane forces of the bottom plate contribute. According to the Von Mises yield criterion or the Tresca criterion as shown in Figure 5.27, the bottom plate in the biaxial stress state can reach the yield stress σ_y in both directions.

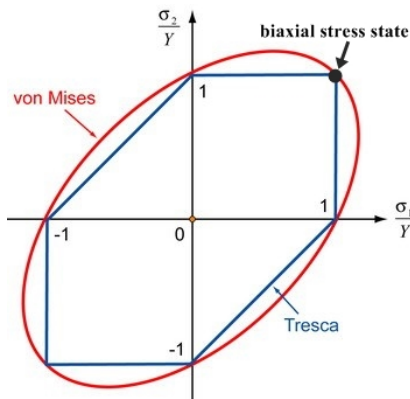


Figure 5.27. Von Mises yield criterion and the Tresca yield criterion.

From the idealized displacement field in Figure 5.26, the displacement is assumed to be sinusoidal in the transverse direction. The displacement is:

$$z = \delta \cos\left(\frac{\pi x}{W}\right); \quad dz = -\frac{\pi \delta}{W} \sin\left(\frac{\pi x}{W}\right) dx \quad (5.15)$$

For half of the plate flange in the transverse direction, the elongation Δ and the elongation rate $\dot{\Delta}$ are:

$$\Delta = \int_0^{W/2} \sqrt{(dx)^2 + (dz)^2} - \frac{W}{2} = \int_0^{W/2} \sqrt{1 + \frac{\pi^2 \delta^2}{W^2} \sin^2\left(\frac{\pi x}{W}\right)} dx - \frac{W}{2} \quad (5.16)$$

$$\dot{\Delta} = \int_0^{W/2} \frac{1}{2} \cdot \frac{2\delta \dot{\delta} \frac{\pi^2}{W^2} \sin^2\left(\frac{\pi x}{W}\right)}{\sqrt{1 + \frac{\pi^2 \delta^2}{W^2} \sin^2\left(\frac{\pi x}{W}\right)}} dx = \frac{\pi^2 \delta \dot{\delta}}{4} \quad (5.17)$$

The rate of the change of the internal energy is,

$$\dot{W}_{\text{int}} = \int_0^{L/2} \cos^2\left(\frac{\pi y}{L}\right) \frac{\gamma N_0 \pi^2 \delta_0 \dot{\delta}_0}{4W} dy = \frac{\gamma \pi^2 \delta_0 \dot{\delta}_0 N_0 L}{16W} \quad (5.18)$$

The rate of the change of the external energy is,

$$\dot{W}_{\text{ext}} = \int_0^{B/2} \cos\left(\frac{\pi y}{L}\right) dy \int_0^{W/2} p \dot{\delta}_0 \cos\left(\frac{\pi x}{W}\right) dx = \frac{pWL}{\pi^2} \sin\left(\frac{B\pi}{2L}\right) \dot{\delta} \quad (5.19)$$

By equating the energy rate of the internal and external energy, we obtain,

$$\dot{W}_{\text{ext}} = \dot{W}_{\text{int}} \Rightarrow p = \frac{\gamma \pi^4 N_0 \delta_0}{16W^2 \sin\left(\frac{B\pi}{2L}\right)} \quad (5.20)$$

When $B = L$, i.e. the pressure is uniformly distributed along the whole span, the pressure is:

$$\text{if } B \rightarrow L, \text{ then } p \rightarrow \frac{\gamma \pi^4 N_0 \delta_0}{16W^2} \quad (5.21)$$

γ is introduced to account for the significant plastic hardening with large deformations in the transverse direction.

5.3.3.3 Girder in-plane crushing

During ice loading, the transverse frames and bulkheads of the structure may be hit. The crushing resistance of the girder can be approximated using the model by Hong and Amdahl (2008). The expressions are:

$$H = 0.395 b^{2/3} t^{1/3} \quad (5.22)$$

$$\frac{P_m}{M_0} = \frac{17.0}{\lambda} \left(\frac{b}{t} \right)^{1/3} \quad (5.23)$$

$$P(\delta) = \frac{1.2M_0b}{H\sqrt{1-\left(1-0.3\frac{\delta}{H}\right)^2}} \left(2 + \frac{\left(1-0.3\frac{\delta}{H}\right)}{\sqrt{3+\left(1-0.3\frac{\delta}{H}\right)^2}} \right) + 5.56 \frac{N_0H\delta}{b} \quad (5.24)$$

5.3.4 Assessment of strength of structural components with simplified methods

5.3.4.1 Response of a stiffened panel strip under point and patch loading

A stiffened panel strip is modelled in accordance with dimensions of the column stiffened panel as shown in Figure 5.28. The bottom plate dimension is 2.9 m×0.625 m×18 mm. The stiffener web is 0.32 m×12 mm while the stiffener flange is 0.05m×40 mm. The steel material in Table 5.1 with a yield strength of 420 MPa is used. The model is discretized with fine meshes, and the mesh size is typically 50 mm. The ends of the stiffened panel strip is fixed in all degrees of freedom.

The force-displacement curves with different patch length is shown in Figure 5.29. It shows that under patch loading with different patch lengths, the model is capable of predicting the resistance curves with good accuracy. The shear effect may degrade the initial bending capacity of the beam. This however does not influence the structural capacity for energy absorption in the ALSs. The stiffened strip deformation is shown in Figure 5.28 (right), and significant web buckling can be observed. The effect of web buckling and strain hardening tends to counteract each other, and the influence on the accuracy of the simplified model is limited.

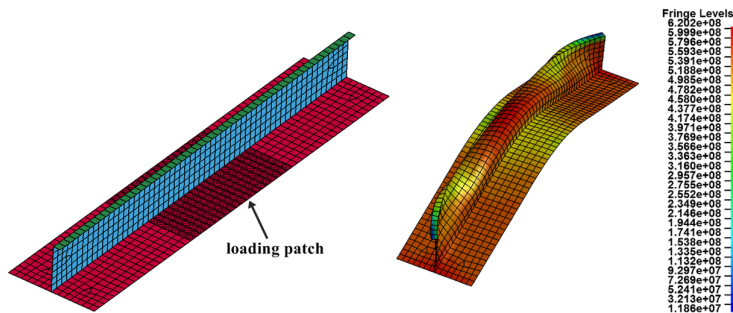


Figure 5.28. (Left) a stiffened panel strip model from the column (Right) deformation of the stiffened beam strip with a patch length of 1.0 m.

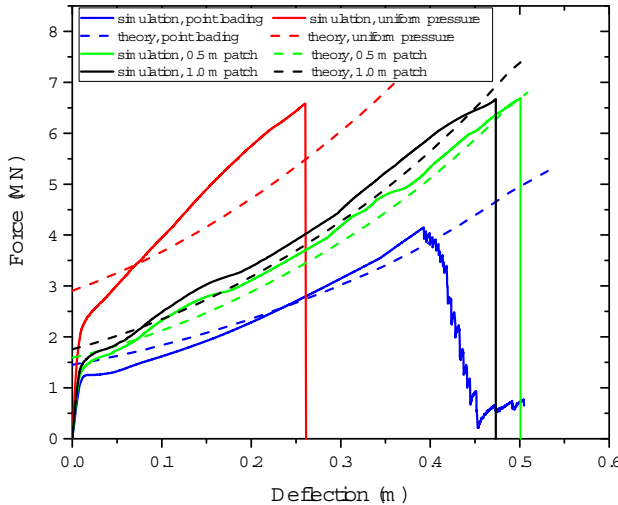


Figure. 5.29. Beam deformation under patch loading.

5.3.4.2 Response of a stiffened panel under patch and uniform loading

The beam assumption of a stiffened panel strip is valid when the stiffened panel width is far larger than the panel length. In reality, the panel width can be comparable or smaller than the length. The contribution from the transverse direction will become important.

A finite element model for a stiffened panel with four stiffeners are established as shown in Figure 5.30(a). The stiffener dimensions and the used material are the same with that used in *Section 5.3.1*. Figure 5.30(b) shows the stress triaxiality and panel deformations under patch loading. It is observed that the stiffener is mainly in the uniaxial stress state while the bottom plate is in the biaxial stress state. This justifies the assumption that the membrane stress in two orthogonal directions may reach the yield stress according to von-Mises yield criterion.

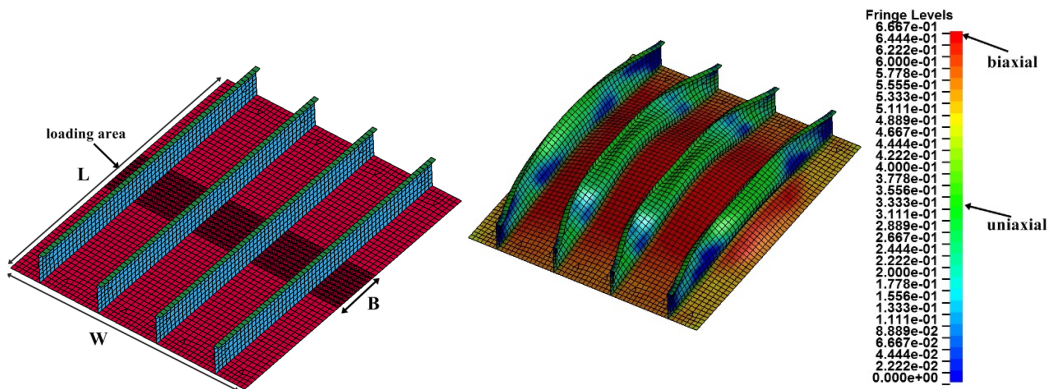


Figure. 5.30. (a). Stiffened panel under patching loading (b). stress triaxiality under pressure loading.

Figure 5.31 plots deformation resistance of the stiffened panel under patch loading with different patch lengths as predicted by numerical simulations and the simplified method. Simplified analytical results show that contribution along the stiffener direction mainly comes from bending capacity of stiffened panel strips while the development of membrane forces is limited. In the transverse direction,

development of the membrane forces is significant accompanied by considerable strain hardening effect. As the simplified model does not consider the strain hardening effect, the predicted pressure is a little lower than numerical simulation results. We tested patch loading of the stiffened panel using steel material with the same yield stress of 420 MPa but with little hardening. The force-displacement curve becomes rather close to the simplified model curve. In order to account for the hardening effect, a hardening factor γ is introduced in the transverse direction only. A hardening factor γ of 1.2 is recommended.

It can be expected that the aspect ratio of the stiffened panel is crucial in determining the panel response. As the panel width is often smaller than the length, and given a certain panel deformation, the membrane force in the transverse direction will be much more significant than that in the stiffener direction.

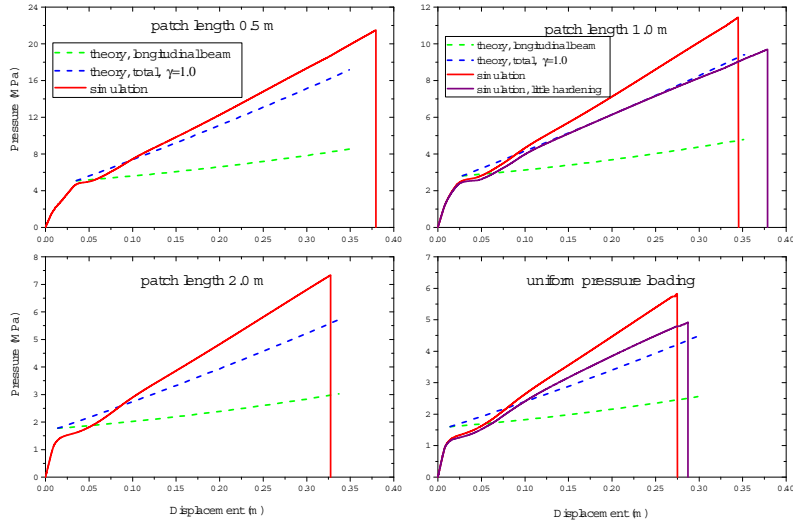


Figure. 5.31. Deformation resistance of a stiffened panel under patch loading.

5.3.4.3 Response of the bulkhead under in-plane crushing

The bulkhead of the structure column is modelled in Figure 5.32 based on the drawings. The stiffener web dimension is 2.9 m×0.3 m×11 mm, and the stiffener flange dimension is 0.05 m×40 mm. The thickness of the attached plate is 14 mm. The steel material with a yield stress of 420 MPa is used from Table 5.1. Rigid tubes with a radius of 0.1 m and 0.5 m are modelled to crush the bulkhead.

Figure 5.33 shows the crushing resistance of the stiffened bulkhead with the two rigid tubes. Results show that the simulation resistance curves are very close for both cases. The simplified model considers crushing of web girders without stiffeners, and the analytical curves agree reasonably with the simulation results. This shows that the influence of transverse stiffeners on the crushing resistance is limited.

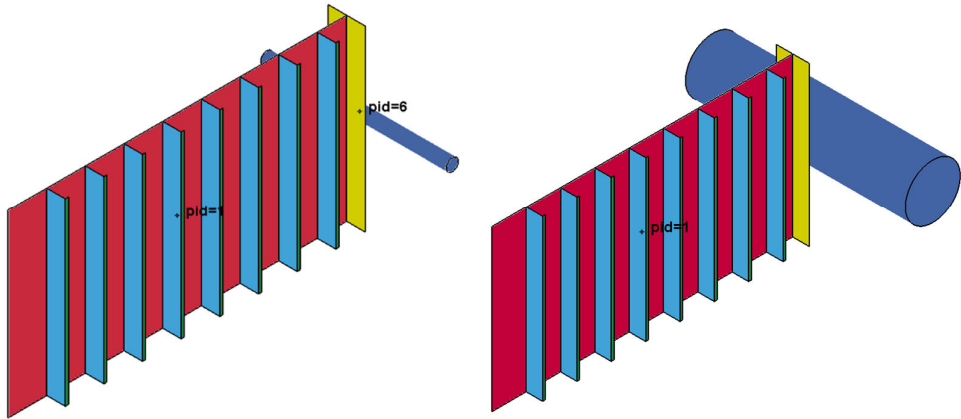


Figure 5.32. Crushing of stiffened bulkhead of the column

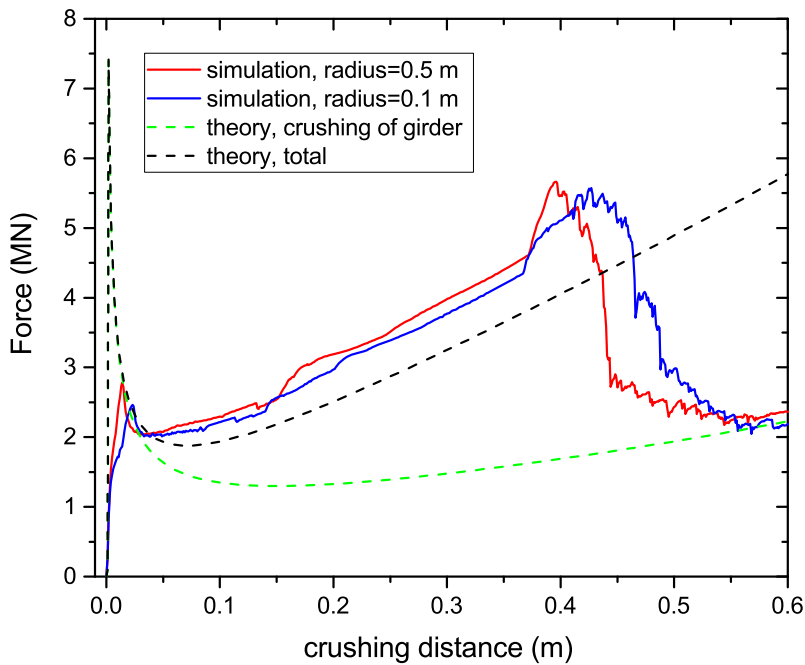


Figure 5.33. Crushing resistance of stiffened bulkhead of the column.

5.4 Integrated Analysis of SAMS and LS-DYNA

Figure 5.34 plots on the right-hand side, the structural impact resistance on seven different locations from LS-DYNA simulations assuming rigid ice, while on the left-hand side of Figure 5.34, the ice crushing resistance calculated from SAMS assuming rigid structures is plotted. The ice load of $F_{ice} = 3.2A^{0.9}$ calculated using the process P-A model (as described in Section 5.2.3) is also plotted. It is assumed that under the same force level, both the ice and the structure should deform and absorb energy in accordance with the resistance curves, and the area below the curves are the corresponding energy that is dissipated in ice and the structure, respectively.

From Figure 5.34, the column bulkhead and cruciform represent hard points of the structure, and are capable of crushing ice significantly. Below a certain force level (around 6 MN for bulkhead and 12 MN for the cruciform), all the deformation goes to the ice. The column stiffened panels have similar force level with that of the ice, and therefore both the ice and the stiffened panels deform and absorb around 50% of the total energy. The resist force of the column corner is much lower than the column side, but it is interesting to observe that the ice crushing force on the corner defined by SAMS is also lower than the ice crushing force from the column side. This makes the strengths of ice and structure on the column corner very close, and both objects will deform to absorb the energy.

Figure 5.35 summarizes the energy absorption with increasing crushing distances. As discussed from the probabilistic analysis in Chapter 4, an energy dissipation of 7.5 MJ is considered critical in the given environmental conditions. If all the energy 7.5 MJ goes to the structure, this will result in a crushing distance of 0.4-0.7 m. In reality, the total energy should be shared by both ice crushing and structural deformations, and the resulting deformation of the structures will be less. Considering shared energy in ice and the structure, the permanent deformation of the structures with a total energy dissipation of 7.5 MJ is summarized in Table 5.2.

It is found that given a total energy of 7.5 MJ, both the ice and the column structure should deform and dissipate part of the energy. The crushing distance can vary from 0.25 m to 0.55 m depending on the impact locations. As initial outer shell rupture generally occurs at 0.6 m-0.9 m, the structure is considered safe from compartment flooding for the given impact energy. It is noted that the markers on Figure 5.34 represent initial fracture of the outer shell when one element is eroded. There is still considerable capacity from one element erosion to large outer shell opening.

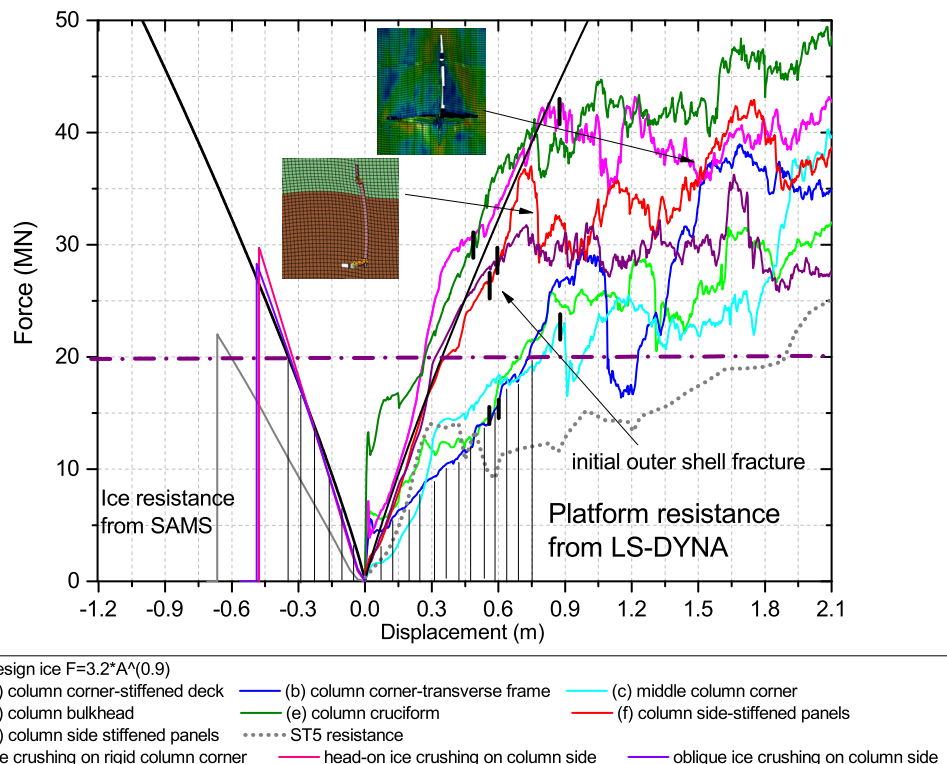


Figure 5.34. Ice-structure impact resistance.

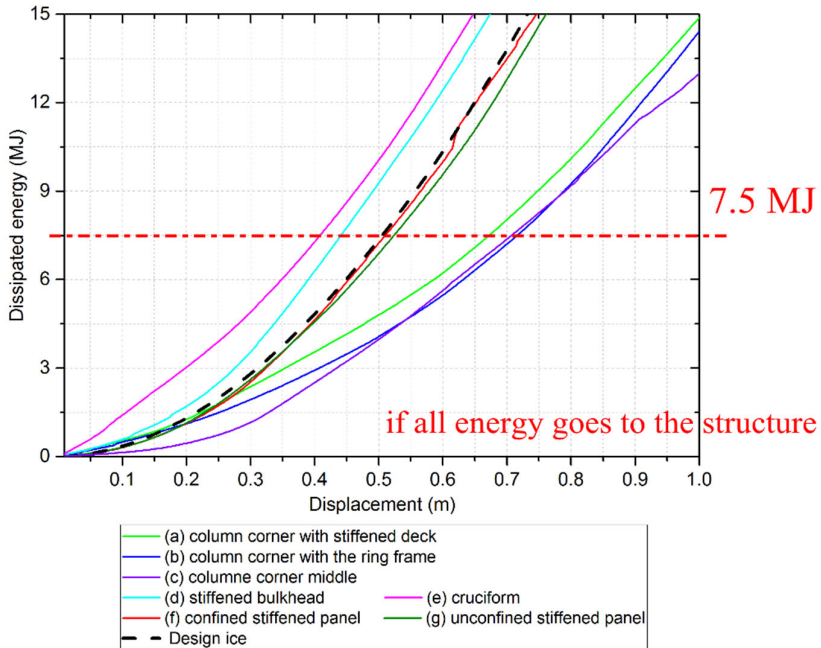


Figure 5.35. Energy absorption in the ice-structure impacts.

Table 5.2. Ice and structural deformation with a total energy of 7.5 MJ

	Location corner (a)	Location corner (b)	Location corner (c)	Location (d)	Location (e)	Location (f)	Location (g)
Ice crushing	0.41 m	0.42 m	0.48 m	0.37 m	0.33 m	0.33 m	0.36 m
Structural displacement	0.51 m	0.55 m	0.50 m	0.29 m	0.27 m	0.38 m	0.36 m
Energy in ice	2.5 MJ	2.7 MJ	3.55 MJ	4.1 MJ	3.2 MJ	3.2 MJ	3.75 MJ
Energy in structure	5.0 MJ	4.8 MJ	3.95 MJ	3.4 MJ	4.3 MJ	4.3 MJ	3.75 MJ

5.4.1 Discussion of fracture modelling in ST5 and ST19

Fracture modelling is essential to determine the ultimate structural strength under ice loading. The ST5 report adopts a fracture criterion based on the 1st principal strain recommended by DNV-GL-RP-C208 (2016). According to DNV-GL-RP-C208 (2016), the maximum principal strain ε_{crl} should be less than

$$\varepsilon_{crl} \leq \varepsilon_{org} \left(1 + \frac{5t}{3l} \right), \text{ where } \varepsilon_{org} \text{ is gross yielding strain, } t \text{ is the element thickness and } l \text{ is the element length.}$$

The limiting principal strain value was calculated to be 7 % for the 355 MPa steel in ST5 report based on the mesh size, plate thickness and material quality.

The BWH criterion based on necking instability is also based on the maximum principal strain. The critical strain $\hat{\varepsilon}_1$ in Eq. (5.8) for the BWH criterion is often assumed to be equal to the power law coefficient n , which corresponds with the necking strain in a uniaxial tensile test. For the present material with a yield strength of 355 MPa, $\hat{\varepsilon}_1$ is 0.16, which is far larger than 7% used in ST5. The BWH criterion used here considers fracture to occur at the onset of necking instability, thus neglecting the post-necking regime. The BWH criterion is therefore considered conservative for structural analysis.

Storheim et al. (2017) discussed the accuracy of different fracture criteria by comparison with several experiments including the BWH criteria and the DNV-GL-RP-C208 fracture criterion. The simulation results of stiffened panel indentation experiments by Alsos and Amdahl (2009) and plate tearing tests by Simonsen and Törnqvist (2004) are shown in Figure 5.36 and 5.37. The results show that fracture simulation using the BWH criterion agrees reasonably with the experimental curve, while the RP-C208 criterion predicts too early fracture with the peak structural resistance being almost half of the experimental capacity. In addition, a graphical view of statistical comparison of behaviour of the tested fracture criteria are shown in Figure 5.38. Based on these comparisons, the RP-C208 criterion is considered overly conservative.

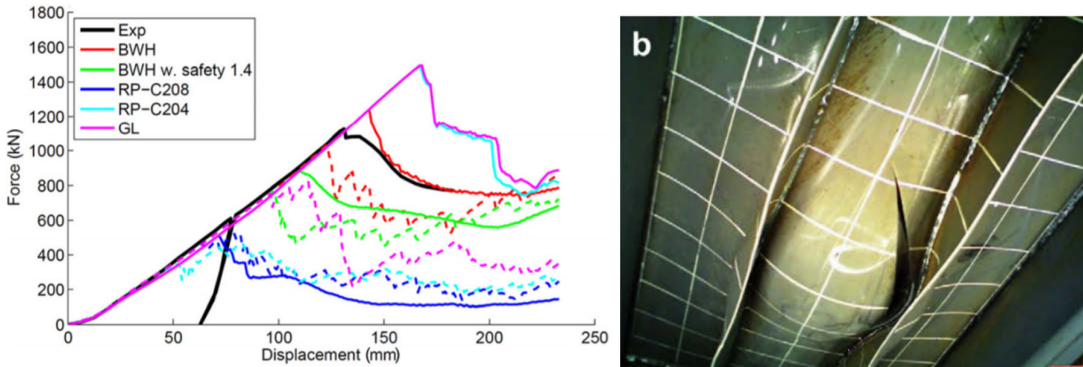


Figure 5.36. Force-displacement results from simulation of the indentation experiment two flatbar stiffeners from Alsos and Amdahl (2009) with different fracture criteria. Continuous lines are with element length equal to thickness, whereas dashed lines are with element length ten times the thickness. Data and simulation from Storheim et al. (2017).

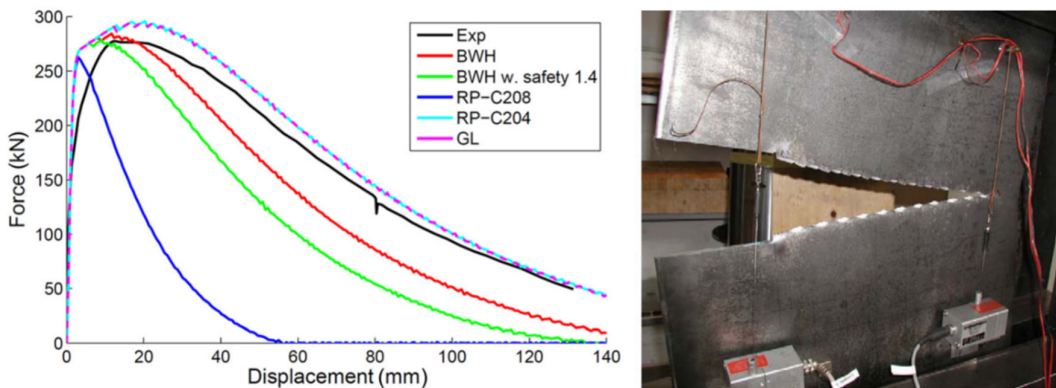


Figure 5.37. Force-displacement results from simulation of the plate tearing tests from Simonsen and Törnqvist (2004) using different fracture criterion with the element length equal to thickness. Data and simulation from Storheim et al. (2017).

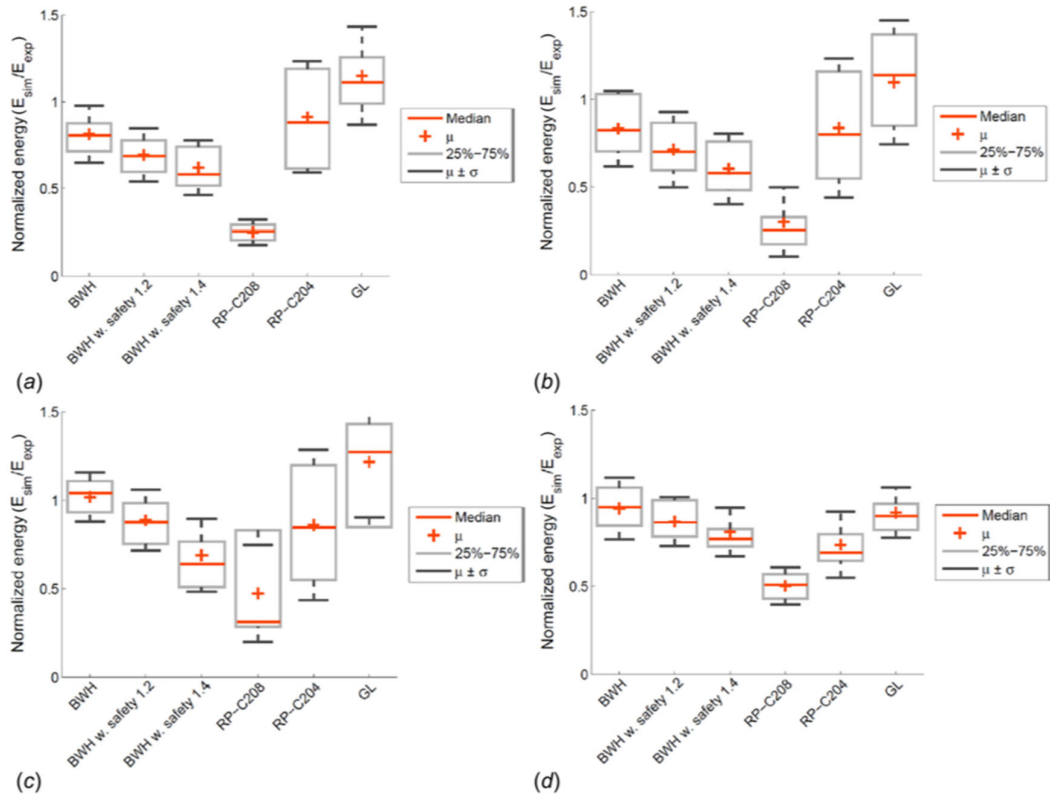


Figure 5.38. Graphical view of statistical comparison of behaviour of the tested fracture criteria: (a) material tests, peak force; (b) all tests, peak force; (c) stiffened panels, peak force; and (d) stiffened panels, end of simulation (Storheim et. al. 2017).

6 Discussions

To achieve the goals of the ST19 project, the study carried out three main tasks, namely 1) analysis of impact events to establish PDFs for impact velocities and locations on the structure; 2) simulations of hundreds of impact scenarios using SAMS to create *energy map* showing the *demand for energy dissipation* at each location on the structure; and 3) assessment of structural damage for the critical impact scenarios. The text below summarises and discusses the main results.

6.1 Discussion on ice feature's geometry

All three tasks were built upon some common starting points, one of which, is the ice feature's geometry. As described in Section 2.3, the glacial ice feature's geometry that is assumed will have a big impact on the outcome of the global and local analysis. Most part of the three tasks in this project is built upon a pre-selected ice feature geometry, i.e., the spheroidal shape in Figure 2.11. If a different ice feature geometry is utilised, one may very well end up with different results when it comes to the impact velocity and impact range, and the associated energy map, and most significantly, the extend of local damage. This is because the local geometry of the ice feature has a decisive effect on the deformation and fracture of the local structure when the ice is assumed rigid, e.g., a sharp corner of an ice feature (see Figure 6.1) might penetrate more into the structure comparing to a blunt ice contact area. It is therefore cautioned when generalising findings made in this project to other ice feature geometries, especially those with quite sharp local geometries.

In this regard, it is recommended to conduct related studies to quantify the local geometries' influence on structure's damage assessment. Figure 6.1b) and 6.1c) illustrate some alternative ice features with exaggerated local geometries for potential further damage assessment. It is, however, emphasise that it is very likely that the shape b) and c) will be crushed in reality to form a blunter shape. This sharp corner being crushed phenomena can to a certain extend, be quantified by the shared energy approach; or to an even larger extend, be characterised by the fully coupled ice crushing and structure deformation approach.

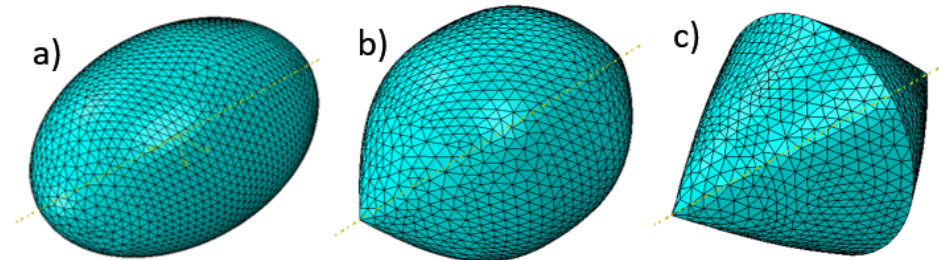


Figure 6.1: Imagined (with exaggeration) ice features with different local geometries, which can be decisive to the deformation and damage of local structure.

6.2 Discussion on correlated impact velocities and heights

In order to derive the correlated impact velocities and heights, a novel method was utilised to simulate the relative motion between the ice features and the structure in the time domain. This method is largely based on the RAOs for the structure and the ice features obtained in ST5. The analysis yields a group of data pairs with correlated impact velocity and impact height. Two impact scenarios were studied, i.e.,

horizontal impact due to relative sway motions and vertical impact due to relative heave motions. In both cases, the motions in Sea State #3 (ST5) was considered with a significant wave height 13.8 m and a wave period of 18 s.

For the horizontal impact scenario, it is necessary to include a current velocity (or a mean drift velocity) in order to sample valid impact events. For this purpose, we have chosen a current velocity of 0.79 m/s, which represents the surface velocity of a current with a 100-year return period at the study site (Block A). Analysing all the impact events, we obtained a series of impact velocities, 1.8 m/s (50% non-exceedance value) and 3.0 m/s (90% non-exceedance), comparing to a series of ‘same’ results obtained in ST5, i.e., around 3.9 m/s (50% non-exceedance value) and 4.4 m/s (50% non-exceedance value). Please refer to Table 3.2 for details. The impact velocities obtained in this study are less conservative than those obtained in ST5, which were based on extreme relative velocities during 3 hours.

Similarly, when analysing the horizontal impact’s height ranges, the method used in this project obtained the following values, $\pm 1.8\text{m}$ (50% non-exceedance value) and $\pm 4.4\text{m}$ (90% non-exceedance value), comparing to $\pm 9.6\text{m}$ (50% non-exceedance value) and $\pm 10.8\text{m}$ (90% non-exceedance value) from ST5 (for details, please refer to Table 3.1). Again, impact height ranges obtained in this study are much smaller than those obtained in ST5.

The reduction in the calculated horizontal impact velocity leads to significant reduction in the impact energy, which scales with the impact velocity squared. The reduced impact energy can potentially alter some conclusions made in ST5 (e.g., penetration depth due to impact). Moreover, the impact height range (e.g., $\pm 4.4\text{m}$ from the ice feature’s tip or -7.3 m to 1.5 m from the SWL; i.e. the 90% non-exceedance value) obtained in this study appears to be, around half of which, covered by the ship impact re-enforced region of a structure, i.e., -3 m to 5 m from the SWL.

The major reason for the reduced horizontal impact velocity and reduced impact height range is that the 3-hour maxima values (both for heights and velocities) are utilised for statistical analysis in ST5. However, in this study, our statistical analysis are based on all potential impact events and we did not make an additional 3-hour maxima sampling of the sampled impact events in Figure 3.10. This is in line with procedures recommended by Fylling (1994), who states: “*the transformed series represent samples of impact incidents with equal probability of occurrence. Hence, in a statistical interpretation, the fractiles of the distribution should be used directly to calculate impact states. This is in contrast to normal wave-induced motions and loads, where the distribution of maxima is used*”.

Only if there are many small ice features in the wave field, and numerous glacial ice feature impact events, shall we consider taking the ‘3-hour maxima value’ - based approach. In this project, one single glacial ice’s impacts are focused.

In addition to the horizontal impact scenario, potential vertical impact was also studied. We focused mainly on the impact scenario with the pontoon. It was found that quite significant vertical velocity (e.g., the 90% non-exceedance value of 2.3 m/s) is expected due to the relative heave motion between the ice feature and the pontoon. This indicates that for the pontoon, vertical impacts may be of more concerns than the horizontal ones. However, in this study, both the external and internal mechanics consider only the horizontal impact scenarios. Damage assessment for the vertical impact would potentially be an important future work.

6.3 Discussion on the energy map

In this part of the tasks, a benchmark test was first carried out to compare results obtained from a set of analytical formulations and those obtained based on SAMS simulations. An idealised test set up was introduced by both head-on and inclined impacts. Several assumptions were introduced into SAMS in order to accommodate the analytical formulas. One important assumption was the utilisation of the rigid contact module from SAMS. Although favourable agreement was achieved in this benchmark test, one might argue that it is only the rigid contact module of SAMS that was benchmarked, not the compliant contact module that is extensively utilised to calculate the ice feature and structure impact in this project. However, it is worth noting that the two contact models in SAMS are built on many of the same building blocks, the same time-stepping and integration schemes. Therefore, to a large extent, the initial benchmark test demonstrates the capability and correctness of SAMS' simulations.

Based on 1800 simulations, SAMS produced an energy map with uniform impact velocity and uniform impact location (see Figure 4.10). These results can be considered as generic given the same structure and ice feature geometry, as the results are scalable (see Figure 4.11). With these results at hand, different impact velocities distributions at different locations can be used to scale and obtain the corresponding impact energy. In this case, the results from Chapter 3 were utilised to obtain the impact energy map and thereby critical impact scenarios. Simultaneous with this project (ST19), there is another accompanying project (ST20) under active development. If additional or improved impact velocity information become available, they can be easily incorporated into the SAMS simulation results in Figure 4.10.

The generated energy map, incorporating both the impact velocity and probability information (from Chapter 3), and the external mechanics by SAMS (from Chapter 4) are very informative. Among many important conclusions, it was found that, for the modelled structure, the horizontal member (the horizontal brace between two columns) are susceptible to impact as well. However, it is not selected as one of the critical scenarios for the following reasons:

- The lower impact energy and maximum load of the impacts on horizontal members.
- The fact that these members are specific to this semi-submersible structure geometry, and the results of a more detailed analysis of horizontal member impact may not be useful in a more general scenario.
- The fact that structural drawings and/or a FEM model of the horizontal members are not available to the authors.

In addition, other potential impact locations, such as the risers, mooring lines and fittings are not included in this analysis. This is partly due to the lack of information on these structural components and partly due to the time constraint of this project. However, the importance of potential impact with these structure members should not be underestimated and further studies are recommended in this regard.

From the scaled 1800 simulations with spheroidal ice feature in open water, we obtained the energy map. Based on the energy map, it was found that 90% of the impact has an impact energy lower than 4.3 MJ and the maximum one is around 7.32 MJ. These numbers are much less than those obtained in ST5, e.g., 16 MJ (in Table 15 of the report of ST5) for the same ice feature geometry. This is mainly due to a reduced impact velocity derived in Chapter 3 in this project and the impact energy is scaled with velocity squared. The idea behind SAMS simulation is to produce an energy map. This map quantifies how the

impact energy is distributed as a whole, e.g., 90% of the impact energy is lower than 4.3 MJ. Nevertheless, in the damage assessment analysis, we conservatively chose 7.5 MJ as our reference impact energy for the discussion and conclusions. In a way, we have added one layer of conservatism herein, even though this impact energy is half of that obtained in ST5 (16 MJ).

6.4 Discussion on the damage assessment

In this project (ST19), damage assessment is carried out based on the shared energy approach, namely, the impact energy is dissipated in both the ice feature and the structure. However, before achieving this, two limiting scenarios were studied, i.e., using SAMS to simulate the crushing of ice feature on a rigid structure and its associated contact force – penetration curve; and using LS-DYNA performing NLFEM analysis regarding a rigid ice feature colliding with a deformable structure, yielding a force – displacement curve. Combining these two curves, we can readily identify where the impact energy flows. Given any penetration/deformation depth, the steepness of these two curves represents how ‘stiff or strong’ the ice or the structure is; and the impact energy shall be dissipated inversely proportionally into the ice and into the structure, i.e., the weaker one dissipates more energy. The total energy to be dissipated is from the analysis conducted in Chapter 4 of this report.

It is worth noting that the above described integrated analysis is not fully coupled. It is an integrated interpretation of two limiting scenarios to achieve an estimation of impact energy sharing between the structure and the ice. Irrespective of its seemingly crude approach, its advantage over either the ‘rigid ice + deformable structure approach’ or the ‘crushable ice + rigid structure approach’ should not be underestimated. It allows for a less conservative quantification with respect to the structural damage assessment.

Bearing the above integrated approach in mind, seven critical locations were chosen for NLFEM analysis. The choice of these seven locations are based on the energy map showing maximum impact energies and taking into account the structural characteristics. Here, it is worth mentioning that the energy map simulated by SAMS are based on a semi-submersible structure from an accompanying project (ST20), whereas the damage assessment was carried out for a different semi-submersible structure, i.e., the ‘Midgard’ platform. Such inconsistency are considered of minor consequences as SAMS simulation focuses more on the global responses (i.e., external mechanics) and NLFEM are more concerned with detailed local structures (i.e., internal mechanics).

In addition, the chosen ‘Midgard’ structure’s column is stronger than the column structure analysed in ST5. Figure 5.34 shows that ST5’s force-deformation curve is lower than those from the relevant locations on Midgard’s column. There are several reasons behind this. First, ST5 applied a different fracture criteria (DNV-GL-RP-C208 (2016)), which is more conservative (i.e., more prone to deform) comparing to the fracture criteria adopted in this study (BWH criterion). Based on existing literatures and experiment data analysis, we conclude that the BWH criterion is already conservative enough since fracture is considered at the onset of necking instability and the post-necking regime is neglected. The BWH criteria has been shown to predict test results pretty well and the DNV-GL-RP-C208 (2016) fracture criteria can be overly conservative according to Storheim et al. (2017). Secondly, the Midgard structure’s plate thickness is larger than that in ST5.

With less impact energies derived from joint results from Chapters 3 and 4, and a much stronger local structure, using the shared energy approach (see Figure 5.34), the maximum indentation depth at different location can be calculated. In extreme scenarios, if all impact energy (7.5 MJ) is dissipated by

the structure at those seven locations, the maximum indentation depth is around 0.72 m (see Figure 5.35). This is in sharp contrast to the results obtained in ST5, which is 1.5 m (see Table 15 of the report for ST5). Again, this decrease in indentation depth, compared to ST5 result, is mainly due to a smaller impact energy due to reduced impact velocity and a less conservative fracture criteria for the structure material. However, even for our result (0.72 m indentation), there are at least two layers of conservatism here: 1) the 90% of the impact energy is less than 4.3 MJ; 2) the impact energy is shared both in ice and the structure, therefore, the actual indentation is much smaller than 0.72 m. For any other combinations of impact energy, impact location, and indentation depth, one is refer to the general results in Figure 5.34 to obtain the true, yet still relatively conservative, results.

7 Conclusions and Recommendations for Further Work

For the northernmost Block A in the 23rd licencing round, an iceberg could potentially be encountered (e.g., an iceberg with a waterline diameter of 48 m can be expected once per $1/(5.2 \times 10^{-4})$ years²). An even smaller ice feature, e.g., with a diameter of 15 m or less, may be expected due to the difficulties in its detection and monitoring by the current available surveillance systems and the challenges in ice management operations (mainly for large icebergs). In order to gain more insights into the consequence of potential impacts with such an ice feature, several related projects (ST5, and the follow-up ST19 and ST20) were established by the Norwegian Petroleum Authority (Petroleumstilsynet). This chapter reports major tasks performed and findings found in the ST19 project.

All the tasks carried out in ST19 were built upon results from or choices made in the previous project (i.e., ST5). The starting point comprises the same ice feature geometry (i.e., a spheroidal ice feature with a diameter of 15 m), a same sea state (wave period = 18 s, significant wave height = 13.8 m, return period = 100 years and is characterised by the JONSWAP wave spectrum) at the same study site. Most of these choices are a natural extension of previous work. These initial choices can largely influence the results obtained in each of our tasks.

As an extension and enrichment to the previous project (ST5), some different additions were made in the ST19 project:

- In addition to extensive studies made for the same ice feature geometry (the spheroidal ice feature), the study does also include two real-life ice feature geometries with the presence of an ambient broken floe ice field for selected simulations.
- In addition to the wave conditions described above, a 100-year return period surface current velocity is selected and incorporated in the analysis.
- Apart from horizontal direction impact scenarios, possible vertical direction impact analyses were also carried out.
- SAMS simulated an extensive set of impact scenarios (1800 simulations) and created a map of impact energy distributed around the structure.
- Damage assessment was carried out with NLFEM analysis with LS-DYNA at seven different locations, which are considered critical based on the results from the impact energy map and their respective structural composition.
- With given SAMS simulations, which treat the ice as crushable and the structure rigid; and NLFEM analysis, which treats the ice rigid but the structure deformable, the study compared the results and established the shared energy approach to quantify in any given impact scenario how much and to where the impact energy is dissipated.
- In addition to simulation results obtained by SAMS and LS-DYNA, simplified hand calculation methods were also used to approximate the SAMS' simulation results by using the process pressure-area curve; and to approximate the LS-DYNA's simulation results by the simplified analytical formulations for structure frames.

² According to Eik and Dezecot (2016), the actual number can be one magnitude higher or lower and this number presented here is only to raise the awareness of iceberg's encounter frequency at the study site.

After going through the above analyses, the following section presents conclusions and major findings that are made under different tasks.

7.1 Conclusions

With a new method involving time domain simulations based on existing results from the ST5 project, the ST19 project concluded that:

- For horizontal direction impacts, the impact velocities increases with the impact height (see Figure 3.13).
- However, the most probable horizontal impact occurs at moderate height around the tip of the ice feature at the still water level (e.g., the maximum probability of impact in Figure 3.14).
- There is a rather low chance to have a horizontal impact either with the pontoon (12.5 m below the still water level) or 5 m above the still water level (see Figure 3.14).
- For the pontoon, horizontal impacts are most likely not of concern for two reasons, 1) low chance of impact; 2) low horizontal velocity of impact (see Figure 3.14).
- However, for the pontoon, it can very well be that the vertical impact is of concern. Given the limited analysis conducted in Figure 3.16, quite substantial vertical impact velocities (see Table 3.5) are obtained.

Extensive simulations of ice feature's horizontal impacts with the structure were carried out by SAMS. The major conclusions are:

- Out of the 1800 spheroidal ice feature's impact with the structure in open water, it is found that critical impacts mainly occur on the structure legs. Impacts on the pontoons have a very low probability – only 0.6% of impacts will occur on the pontoons under the considered wave and current conditions.
- The horizontal members which were present in the simulated semi-submersible structure have a substantial probability of impact. However, the impact energy of horizontal member impact is lower, since the hull geometry is inclined at the location of impact, and the impact velocity will be lower than in case of impacts higher on the structure.
- The maximum impact energy resulting from the simulations is 7.32 MJ. However, high energy impacts have a low probability. 90% of the simulated open water impacts result in an impact energy lower than 4.3 MJ when accounting for the impact probability and impact velocity distribution as a function of height as found in Chapter 3.
- High energy impacts have a low probability because of the correlation between impact probability and impact velocity. High velocity impacts have a lower probability of occurrence.
- Out of the 90 simulations with real-life ice feature geometry and an ambient floe ice field, it was found that: even though the real-life ice feature has a substantially higher mass than the spheroidal ice feature, the dissipated contact energy and maximum contact force are lower than the spheroidal ice feature in open water. This is mainly caused by the real-life iceberg's lower impact velocity, since the large ice feature is only driven by current and not by waves in our simulation. In addition, as described in Section 2.3.1, a large ice feature tends to have an off-centric impact with the structure, which limits the impact energy.
- For the ambient floe ice field, the ice floes used in the analysis do not have sufficient momentum to increase the contact energy to values larger than the value caused by the initial ice feature impact.

Damage assessments were carried out at seven critical locations on the structure's column. The integrated SAMS and LS-DYNA analysis results yield rather rich information to quantify impact energy's dissipation in a shared manner. As an example, for a conservatively chosen total impact energy of 7.5 MJ, it is found that:

- Both the ice and the column structure should deform and dissipate part of the impact energy.
- The indentation depth into the structure can vary from 0.25 m to 0.55 m depending on the impact locations. As the outer shell rupture generally is predicted to occur at 0.6 m-0.9 m, the structure is considered safe from compartment flooding risks with the given impact energy.
- For any other impact energy levels, one can refer to Figure 5.34 to obtain information about the shared energy dissipation, structural deformation and ice crushing depth respectively.

7.2 Further work

Concerning this important engineering problems, i.e., impact between a small ice feature and a semi-submersible structure, based on the previous discussions and conclusions, we propose the following further work to complete all the tasks (i.e., ST5 and ST19) that have been achieved so far.

- The damage assessment of other critical structural members, such as risers and mooring lines, was not part of this study and should be included in further studies. The same procedures (i.e., impact energy map → damage assessment) as have been performed in the current study (concerns mainly the column and pontoons) can be applied to these structural members. However, special structural analysis techniques should be employed to account for the compliance/large motion of these structural member under impact.
- Empirical evidence should be collected to justify the selected ice feature geometry. As was discussed in Section 6.1, the local geometry of an ice feature would significantly influence the damage assessment results. This study chose a spheroidal shape to represent the ice feature and local geometry at the spheroid's tip was mainly used for the NLFEM analysis in Chapter 5. Further studies are needed to measure the sensitivity of ST19 results to other local geometries (with different sharpness). These studies will construct a series of 'shared energy plot' to study the energy dissipations and the associated deformation in the structure and the crushing depth in the ice.
- In addition to the integrated analysis performed in this project, a fully coupled analysis of the ice-structure interactions should be performed (i.e., deformable structure and crushable ice). Emphases should be given to the verification and the validation of this approach. The later requires an access to in-situ/full-scale test data where both the ice feature and the structure undergo significant permanent deformations during impact.
- In this project, the relative motions and impact events were analysed as explained in Chapter 3. The outcome of that analysis (i.e., impact probability and velocity's distributions) was used as input to SAMS simulations (i.e., the external mechanics part) to construct the energy map. However, this two-step approach can be replaced by a fully coupled approach using SAMS with enhanced hydrodynamic modules. This comprises time-domain simulations of multi-bodies motion under the combined actions from waves, wind and currents, in addition to the capability of SAMS to detect and solve contacts. This should be included in further studies and it will allow explicit and direct simulations of various impact events and their associated impact energy. In this way, all types of impacts (i.e., the horizontal, vertical and inclined impacts) can be natural

outcome of the simulation; and thus a more generic impact energy map can be constructed than the one presented in Figure 4.12, which was only for horizontal impact scenarios.

- When analysing the relative motions in Chapter 3, the study separated the impact events into the horizontal impact and vertical impact scenarios. The focus has been given to the horizontal impact events when it comes to the construction of energy map and to damage assessments. As discussed above, this limitation can be removed by adopting the fully coupled approach using SAMS. As an intermediate solution, one may perform an extensive study on the vertical impact scenarios following the same procedures as for the horizontal impact scenarios described in Chapter 3. This will be especially useful for the assessment of structural damage of the pontoons as they are more susceptible to vertical impacts than to the horizontal impacts.
- Both ISO 19906 (2018) and NORSOK 003 (2016) recommend to use probabilistic approach to identify ice feature actions yielding ALS. In order to use this probabilistic approach in the context of structural design assessment under ALS conditions, encounter frequency and statistical distribution of ice features' geometry (size and parametrized shape) needs to be studied at the location of the structure, taking into account effects of climate change. For example, a coupled analysis of ice features' trajectories and their associated thermo- and wave- erosions at the location of the structure.

Reference

- (IACS), I. A. O. C. S. 2011. Unified Requirements for Polar Ships: I2–Structural requirements for Polar Class ships
- ALSOS, H. S. & AMDAHL, J. 2009. On the resistance to penetration of stiffened plates, Part I–Experiments. *International Journal of Impact Engineering*, 36, 799-807.
- ALSOS, H. S., HOPPERSTAD, O. S., TÖRNQVIST, R. & AMDAHL, J. 2008. Analytical and numerical analysis of sheet metal instability using a stress based criterion. *International Journal of Solids and Structures*, 45, 2042-2055.
- AMDAHL, J. 1980. Probabilities of occurrence and impact velocities for impacts in the North sea. Det Norske Veritas Research Division.
- BRESSAN, J. & WILLIAMS, J. 1983. The use of a shear instability criterion to predict local necking in sheet metal deformation. *International Journal of Mechanical Sciences*, 25, 155-168.
- DNV-GL-RP-C208 2016. Determination of Structural Capacity by Non-linear FE analysis Methods. *Det Norske Veritas*.
- EIK, K. J. & DEZECOT, C. 2016. Barents Sea exploration collaboration, “Fysisk miljø i Barentshavet sørøst.”
- EKEBERG, O.-C., SHIPILOVA, O., BIRKNES-BERG, J. & JOHANSEN, A. 2018. Glacial Ice Impact.
- FREDERKING, R. The pressure area relation in the definition of ice forces. The Eighth International Offshore and Polar Engineering Conference, 1998. International Society of Offshore and Polar Engineers.
- FYLLING, I. On the Statistics of Impact Velocities and Hit Positions Related to Collisions and Mating Operations for Offshore Structures. BOSS, 1994. 297-306.
- HILL, R. 1952. On discontinuous plastic states, with special reference to localized necking in thin sheets. *Journal of the Mechanics and Physics of Solids*, 1, 19-30.
- HONG, L. & AMDAHL, J. 2008. Crushing resistance of web girders in ship collision and grounding. *Marine Structures*, 21, 374-401.
- KJERSTAD, Ø. K., LU, W., SKJETNE, R. & LØSET, S. 2018. A method for real-time estimation of full-scale global ice loads on floating structures. *Cold Regions Science and Technology*.
- LIU, Z. & AMDAHL, J. 2019. On multi-planar impact mechanics in ship collisions. *Marine Structures*, 63, 364-383.
- LU, W., HEYN, H.-M., LUBBAD, R. & LØSET, S. 2018. A large scale simulation of floe-ice fractures and validation against full-scale scenario. *International Journal of Naval Architecture and Ocean Engineering*.
- LU, W., LUBBAD, R. & LØSET, S. 2015a. In-plane fracture of an ice floe: A theoretical study on the splitting failure mode. *Cold Regions Science and Technology*, 110, 77-101.
- LU, W., LUBBAD, R. & LØSET, S. 2015b. Out-of-plane failure of an ice floe: Radial-crack-initiation-controlled fracture. *Cold Regions Science and Technology*, 119, 183-203.
- LU, W., LUBBAD, R., LØSET, S. & KASHAFUTDINOV, M. 2016. Fracture of an ice floe: Local out-of-plane flexural failures versus global in-plane splitting failure. *Cold Regions Science and Technology*, 123, 1-13.
- LUBBAD, R. & LØSET, S. 2011. A numerical model for real-time simulation of ship-ice interaction. *Cold Regions Science and Technology*, 65, 111-127.
- LUBBAD, R., LØSET, S., LU, W., TSARAU, A. & VAN DEN BERG, M. 2018. An overview of the Oden Arctic Technology Research Cruise 2015 (OATRC2015) and numerical simulations performed with SAMS driven by data collected during the cruise. *Cold Regions Science and Technology*.
- MARINATOS, J. N. & SAMUELIDES, M. S. Material characterization and implementation of the RTCL, BWH and SHEAR failure criteria to finite element codes for the simulation of impacts on ship structures. 6th International Conference on Collision and Grounding of Ships and Offshore Structures, ICCGS 2013, 2013 Trondheim, 57-67.
- NORSOK 2017. Actions and action effects, N-003. *Oslo: Norwegian Technology Standards Institution*.
- SIMONSEN, B. C. & TÖRNQVIST, R. 2004. Experimental and numerical modelling of ductile crack propagation in large-scale shell structures. *Marine Structures*, 17, 1-27.
- STORHEIM, M., ALSOS, H. S. & AMDAHL, J. Evaluation of Nonlinear Material Behavior for Offshore Structures Subjected to Accidental Actions. ASME 2017 36th International Conference on Ocean, Offshore and Arctic Engineering, 2017. American Society of Mechanical Engineers, V03AT02A006-V03AT02A006.
- STORHEIM, M., AMDAHL, J. & MARTENS, I. 2015. On the accuracy of fracture estimation in collision analysis of ship and offshore structures. *Marine Structures*, 44, 254-287.

- TAVAKOLI, M. T. & AMDAHL, J. 2010. Analysis of collision between Midgard platform and 8000 tonnes displacement ship
- TSARAU, A. 2015. *Numerical Modelling of the Hydrodynamic Effects of Marine Operations in Broken Ice*. PhD, Norwegian University of Science and Technology.
- TSARAU, A., LØSET, S. & GRINDSTAD, T. Propeller wash by an icebreaker. 22nd IAHR International Symposium on Ice August 11 to 15, 2014 Singapore.
- VAN DEN BERG, M., LUBBAD, R. & LØSET, S. 2018. An implicit time-stepping scheme and an improved contact model for ice-structure interaction simulations. *Cold Regions Science and Technology*, 155, 193-213.
- YU, Z. & AMDAHL, J. 2018. A review of structural responses and design of offshore tubular structures subjected to ship impacts. *Ocean Engineering*, 154, 177-203.
- YU, Z., AMDAHL, J. & SHA, Y. 2018. Large inelastic deformation resistance of stiffened panels subjected to lateral loading. *Marine Structures*, 59, 342-367.